The Origin of Harmonic Tremor at Old Faithful Geyser

Thesis by

Sharon Kedar

In Partial Fulfillment of the Requirements

for the Degree of

Doctor of Philosophy

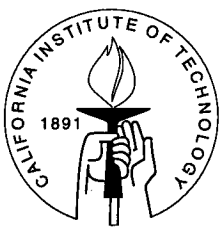

Caltech

Pasadena, California

1996

(Submitted June 5, 1996)

Abstract

Volcanic tremor, the seismic signal which is often associated with eruptions, is among the least understood phenomena in seismology. Large variations in the physical properties of volcanic rocks and fluids along with the complex geological structure make it difficult to obtain reliable source models. Old Faithful geyser, Yellowstone National Park, was chosen as a laboratory for studying fluid-flow-induced seismicity. The geyser's cyclic behavior on an hourly time scale, and its accessibility, make it suitable for a detailed study of seismic behavior between eruptions simultaneously with underwater pressure measurements inside the geyser.

We observe that sharp pressure pulses inside the water-column attributed to steam bubble collapse are followed by distinct seismic events, with a sharp onset and a harmonic horizontal motion whose frequency varies spatially but not temporally. A superposition of these events creates the appearance of continuous harmonic tremor. Since the pressure in the water column exhibits no sign of resonance, the harmonic motion must be caused by elastic waves reverberating in the solid medium. A near-surface soft layer is demonstrated to be a possible elastic model.

The harmonic tremor observed at Old faithful seems analogous to some examples of shallow volcanic tremor.

Contents

0.1 Introduction

Volcanic and hydrothermal seismic activity presents one of the most peculiar puzzles in seismology. The seismic signals which precede, accompany, and follow volcanic and hydrothermal eruptions are intriguing because of their simple harmonic nature (referred to as harmonic tremor), and because their source is still unknown, beyond the fact that they are assumed to be generated by fluid motion. In recent years volcanic tremor has been used several times as a prediction tool with some success (*Mori* [1995]). These predictions were based mainly on intensity patterns of volcanic seismic signals, without a clear understanding of the physics behind them, the understanding of which is essential if a clear assessment of an impending eruption is to be made. The key to such understanding is first and foremost a clear resolution of source effects from path and site effects. Unfortunately, the volcanic environment poses serious obstacles to achieving this resolution. One difficulty is the simplicity of harmonic tremor signals, which can be adequately described by any number of models, but provide little or no physical constraints for these models. Adding to this is the volcanic environment's geological and dynamical complexities. The irregular volcanic topography, the complicated stratigraphy, and the highly irregular pipe and duct systems make it hard to fully account for seismic path effects, while the fluid system spans a large range of fluid properties, temperatures, pressures, and flow regimes. Another objective difficulty is the amount and quality of data from volcanoes. Due to the logistical difficulties of instrumenting active volcanoes, high quality data are sparse, whereas most volcano source analysis reported to date has been based on data obtained by band-limited instruments. Only recently have volcano seismologists begun to incorporate broadband high-dynamic-range instruments into their research, and have begun to unravel the processes that were formerly obscured by the band-limited instruments.

As some similarity between geyser and volcanic seismic activity is known to exist (*Kieffer* [1984]), and in order to overcome the above difficulties, we have chosen Old Faithful geyser, Yellowstone National Park, as a laboratory of fluid-flow-induced seismicity. The geyser's cyclic behavior on a convenient time scale, $\sim$ 1 hour, and its accessibility, make it a logistically convenient environment for a detailed seismic study and ultimately for a direct measurement of the seismic source. The following is a report of the seismic and hydrodynamic data gathered at Old Faithful Geyser in the time period 1991-1994, of their physical interpretation, and of their possible application to volcano seismology.

Chapter 1 Observations

1.1 General

Old Faithful is probably the most studied geyser in the world. Located in the Upper Geyser Basin of Yellowstone National Park, its surface expression is a 4 m high, 60 m wide mound with an approximately 2×1 m^2 opening at the top. The conduit extends downwards, successively narrowing and opening into larger spaces, as described by *Birch and Kennedy* [1972] and as inferred from the spectacular video recordings made by Westphal, Kieffer and Hutchinson (personal communication). The Geyser's eruptions are 2–5 minute long with the interval between them ranging from 30–100 minutes, and their time of occurrence is predictable to within 15 minutes.

The pioneer of scientific studies of the geyser was J. Rinehart (*Rinehart* [1965], *Rinehart* [1967], *Rinehart* [1980]), who was the first to deploy seismometers around the geyser and measure temperature inside it. *Birch and Kennedy* [1972] continued with temperature measurements at different depths in the geyser, and *Kieffer* [1984] gave an elaborate description of the geyser's behavior including its seismicity and thermodynamics. *Kieffer* [1984] first pointed out the similarities between geyser seismicity and volcanic seismicity and the possible relevance of geyser studies to interpretation of volcanic tremor.

These studies provided a good overall understanding of geyser behavior. However, since all past studies used analog recorders and short-period ($\sim$ 1 s period) seismometers without simultaneous time-resolved measurements of pressure and temperature, the source of tremor and its interaction with the solid medium at Old Faithful were not fully understood.

Our work at Old Faithful was designed to establish a cause-and-effect relationship between the source of seismic noise and the observed harmonic tremor. We have carried out three seismic studies at Old Faithful geyser (1991, 1992 and 1994), in which time-resolved pressure variations inside the geyser, passive broadband and short-period seismicity around the geyser, and seismic response to an external sledge-hammer source have been measured.

1.1.1 Field-work and setup

Three scientific excursions to Old Faithful geyser were made (Figure 1.1). The first (not shown in the figure) was carried out in 1991 and deployed two broadband sensors (GURALP CMG-3ESP, flat velocity response 0.0333-50 Hz) and REF-TEK 6-channel portable data-loggers with a 16-bit digitizer. This served as a pilot study for a second and a more elaborate seismic survey which was

carried out in October, 1992, and which incorporated broadband recordings of geyser generated signals and sledge-hammer pulses. This survey included six broadband setups identical to the 1991 instruments, which were placed around the geyser in different configurations for continuous recordings at 100 sps and 200 sps for periods of a day at a time. In addition an array of 96 short-period (natural frequency 1 Hz) vertical geophones was placed in a tight grid over the geyser's dome. Based on the observations from 1991 and 1992, a probe was designed and built to measure pressure inside the water-column simultaneously with the seismic measurements on the geyser's dome. The recording was made at 250sps simultaneously with 2-broadband sensors and three 3-component short period sensors (L-28, natural frequency 4.5 Hz) for 40 minutes. This last experiment (October 1994) obtained a direct measurement of the source of seismic waves and resolved propagation effects from source effects.

1.2 Data

1.2.1 The eruption cycle

An eruption cycle is defined as the time-interval between the end of one eruption to the end of the next.

Figure 1.2 displays a 12-hour-long vertical component record obtained at station WY000 (Figure 1.1). The general pattern of the eruption cycle starts with a quiet period, then, a half hour later, the activity increases in intensity and amplitude, and gradually decays until the final moments before an eruption. A short ($\sim$ 50min) eruption cycle shows a similar behavior without a period of seismic silence. The amplitude decay was explained by *Kieffer* [1984] by an increased acoustic impedance mismatch between the two-phase water-steam mixture and the conduit walls, due to an increased amount of steam in the final stages of boiling.

Figure 1.3 displays the North-South component along with the vertical component for the first six hours of Figure 1.2. It is evident that the horizontal component has a much stronger long-period component, mostly attributed to tilt caused by wind, while sometimes a long-period tilt accompanies an eruption, as the runoff water flows by the sensors.

Although the interval between eruptions fluctuates over a period of several years, it is known to have a bi-modal distribution with peaks at $\sim$ 50min and $\sim$ 75min. The eruption duration also has a bi-modal distribution peaked at $\sim$ 2min and $\sim$ 5min. The relationship between the durations of eruptions and the interval between them is discussed in detail in Appendix A.

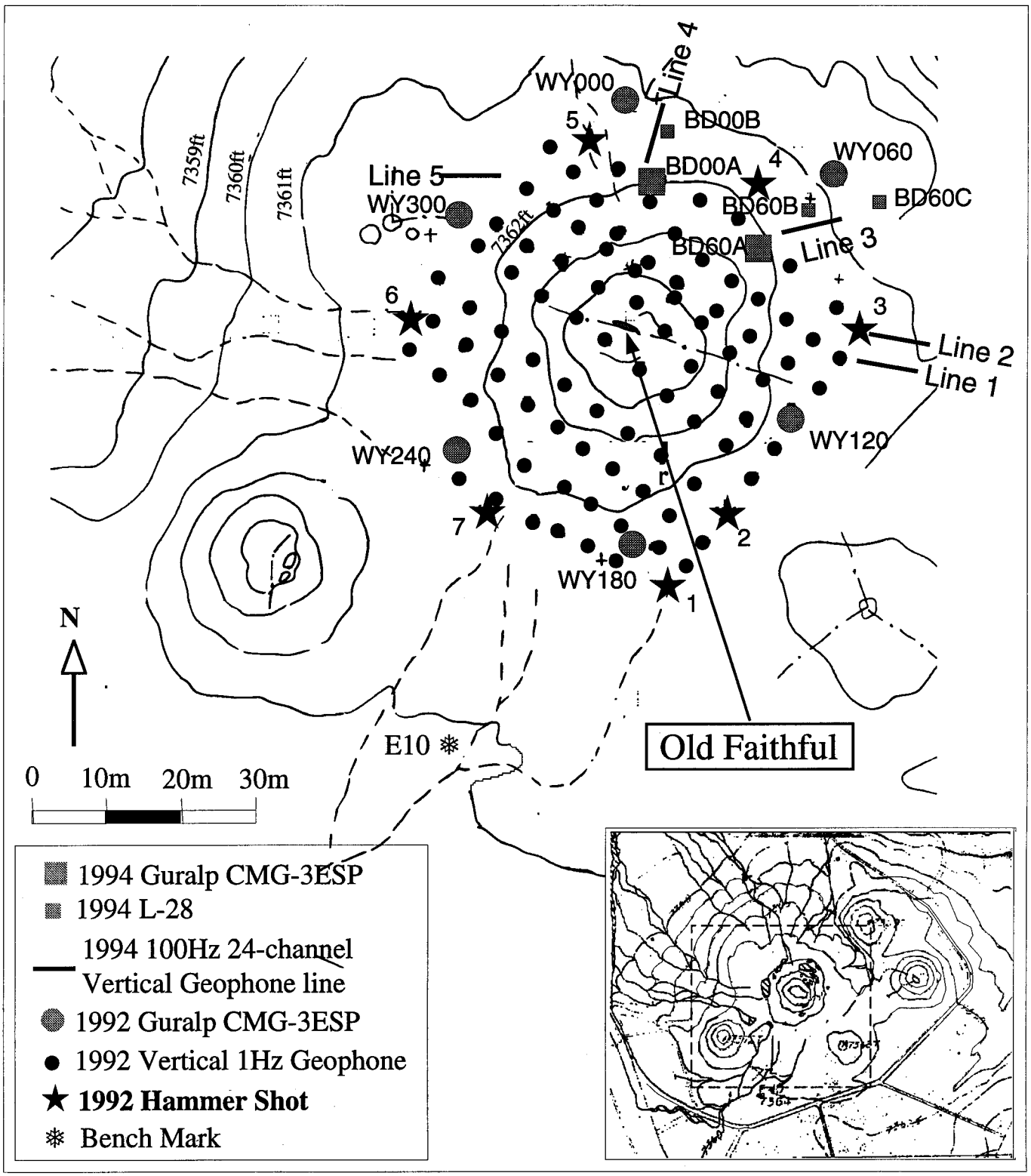

Figure 1.1: A map of the survey area and instrument setups for the 1992 and 1994 deployments in relation to Old Faithful and two of its neighboring passive domes. The orientation of the geyser's orifice is indicated by the broken line across its dome.

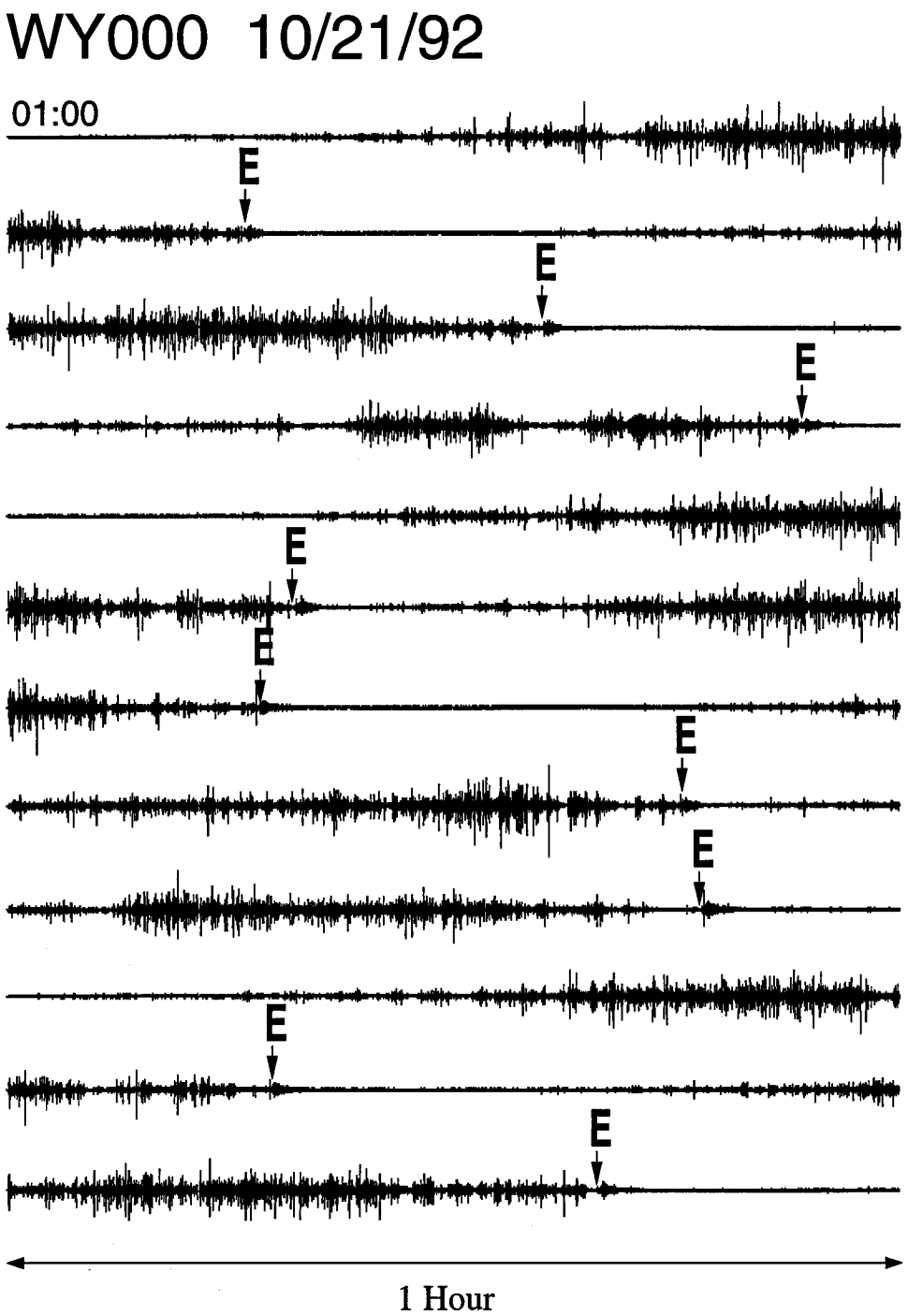

Figure 1.2: A 12-hour record of the vertical motion recorded at WY000 (Figure 1.1). Eruptions are marked by **E**.

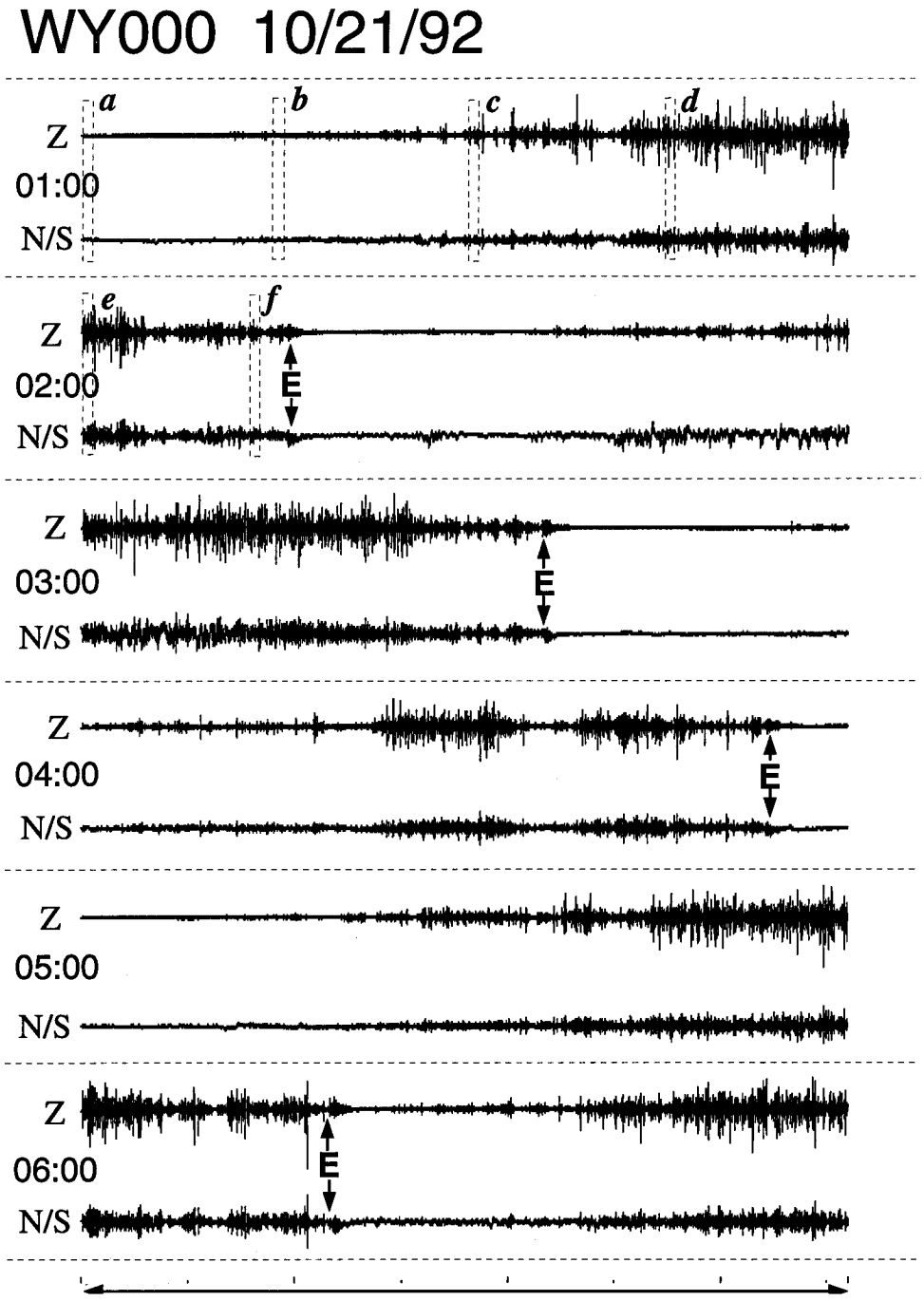

Figure 1.3: Vertical and N/S (Radial) components for the first six hours of Figure 1.2. Eruptions are marked by **E**. Six 1-minute time windows marked by *a* - *f* are displayed in Figures 1.6 through Figure 1.8.

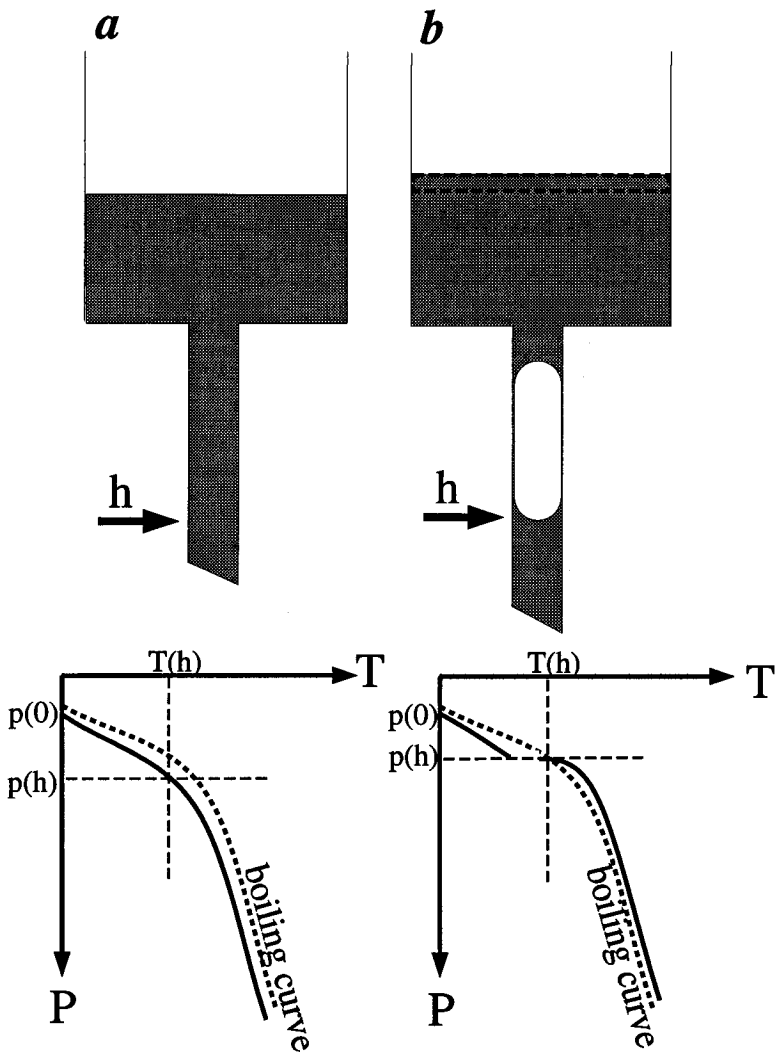

Figure 1.4: A schematic illustration of instantaneous boiling of a near-boiling water column due to a volumetric change, and water-level rise into a tank.

The eruption

An eruption occurs when a mass of water is removed temporarily from the top of the superheated column, causing a sufficient drop in the hydrostatic head to result in instantaneous boiling of the entire column and subsequently an evacuation of the conduit in the form of an eruption. Two main mechanisms may be responsible for the reduction in the hydrostatic head: A temporary displacement of a mass of water by an explosive process, or a mass of water pushed into a larger diameter space at the top of the water column due to volume change. The former is known as 'pre-play', a process observed 5-10 minutes before an eruption at Old Faithful, which starts like a normal eruption that immediately dies down as the displaced water falls back into the conduit. The latter is illustrated in Figure 1.4 and was described by *Griffith* [1962].

As a slug of steam is formed inside the pipe, the water is pushed up into the tank. However, the

mass of the steam slug is negligible. Most of the water which occupied the volume (now occupied by vapor) is spread over a wider space, thus lowering the hydrostatic pressure in the fluid below the slug. As is schematically described in Figure 1.4, if the fluid is near boiling, a slight reduction of the hydrostatic pressure will cause instantaneous boiling of the fluid below the slug. It should be pointed out that the same phenomenon takes place for any shape of widening pipe (such as a funnel), and any form of volume change.

An eruption generates a distinct seismic signal as can be observed in Figures 1.5. All components show a $\sim 1-3$ minute long coda caused by the water falling on the ground. In some cases (four out of the nine eruptions marked by arrows in Figure 1.5) there is a distinct event which seems to initiate the eruption.

The significance of this observation is debatable, as it appears only at a fraction of the eruptions, and when it does it can be obscured by the background activity. There is no other signal which may be used as a prediction tool, other than the overall reduction in the background noise amplitude. Seismically, the eruption emerges from the background noise with no clear precursor.

1.2.2 Harmonic tremor

Figure 1.6 through Figure 1.8 demonstrate that the activity depicted in Figure 1.2 and Figure 1.3 is composed of individual events with a sharp onset and a characteristic decay time of $\sim 0.2-2$s depending on the station. It is evident that the intensity of the activity is dependent on the rate of occurrence of events as well as their amplitude, and that the pulses get stronger and more frequent as the eruption cycle progresses. At the early stages of the eruption cycle, infrequent low-amplitude pulses are observed. The pulses get stronger and more frequent until their amplitude and rate become steady (Figure 1.8). Minutes before the eruption the amplitude goes down due to the poor acoustic impedance match between the bubbly fluid and the geyser wall (*Kieffer* [1984]), while the rate stays fairly constant.

Spatial properties

Zooming on one pulse recorded simultaneously at the six 'WY' stations (Figure 1.1), Figure 1.9 - 1.11 present the vertical, radial and tangential motion at each of the station relative to Old Faithful's orifice, along with their Fourier amplitude spectra. For comparison, similar data from hammer shot 4 (Figure 1.1) is presented.

It becomes apparent from Figures 1.9 - 1.11 that:

- The harmonic signal is more pronounced in the horizontal components than the vertical component.

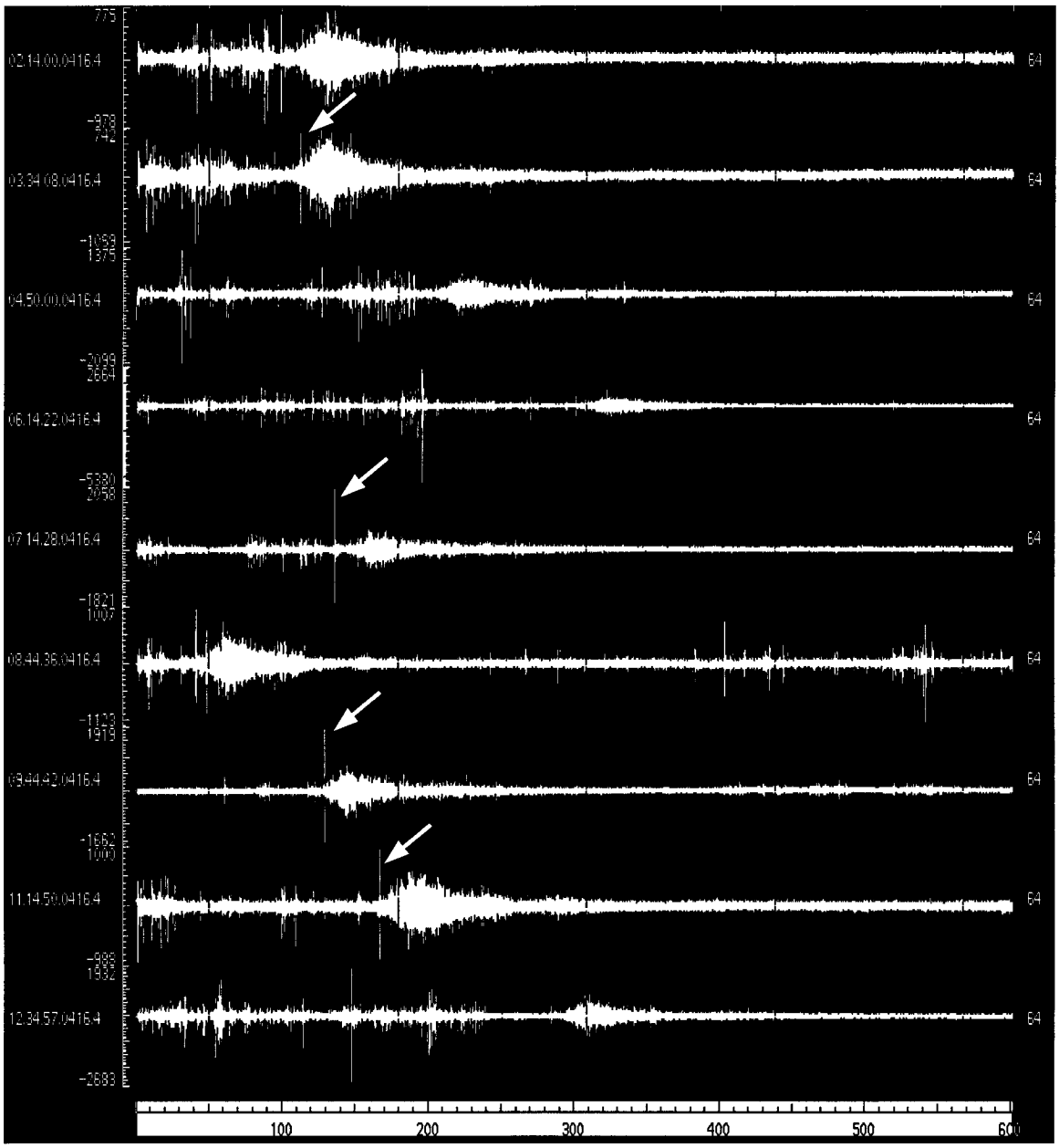

Figure 1.5: A 10-minute window of the vertical component at WY000 around the nine eruptions marked on Figure 1.2

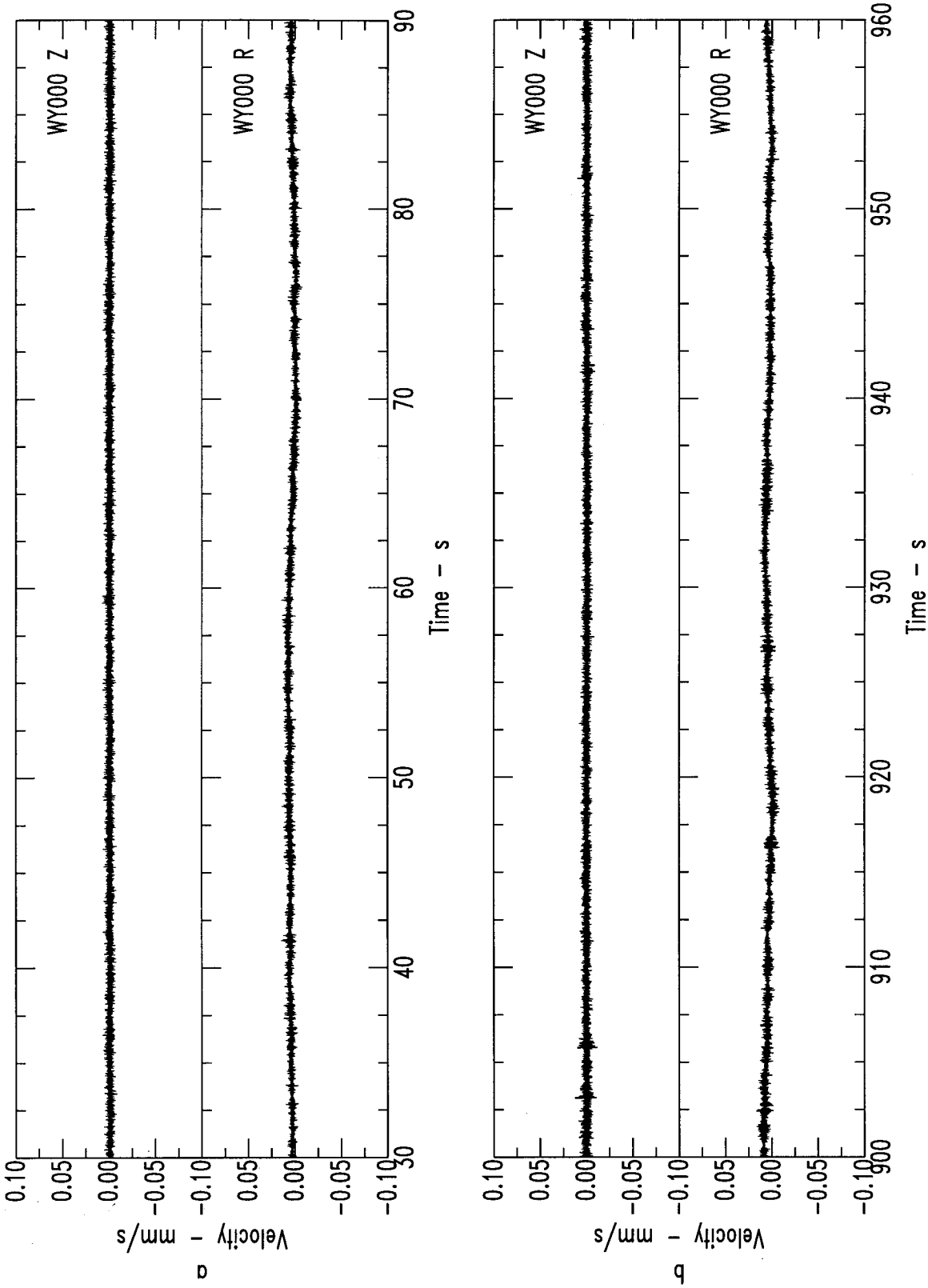

Figure 1.6: A blow up of the 1-minute time window marked **a** and **b** in Figure 1.3.

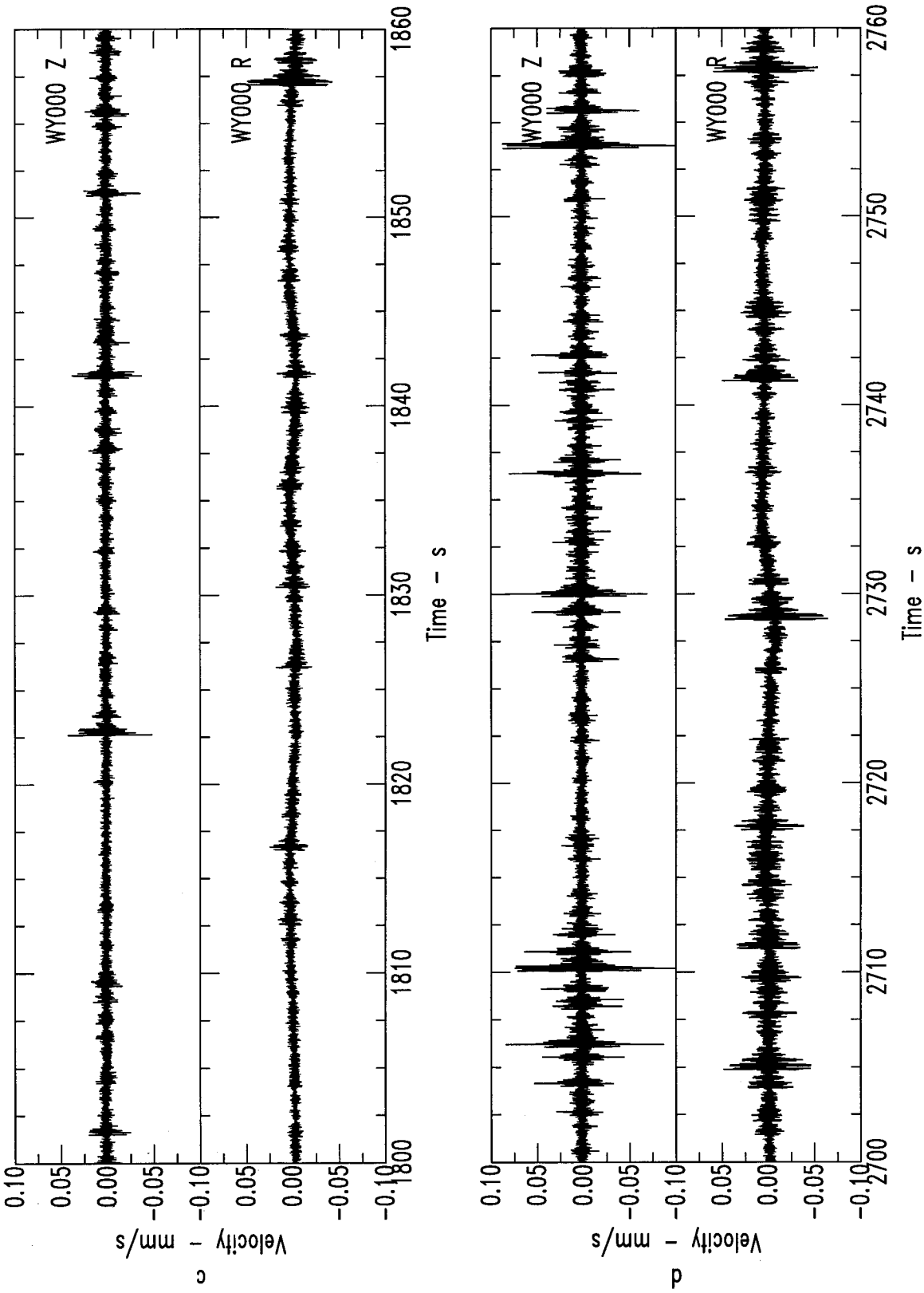

Figure 1.7: A blow up of the 1-minute time window marked **c** and **d** in Figure 1.3.

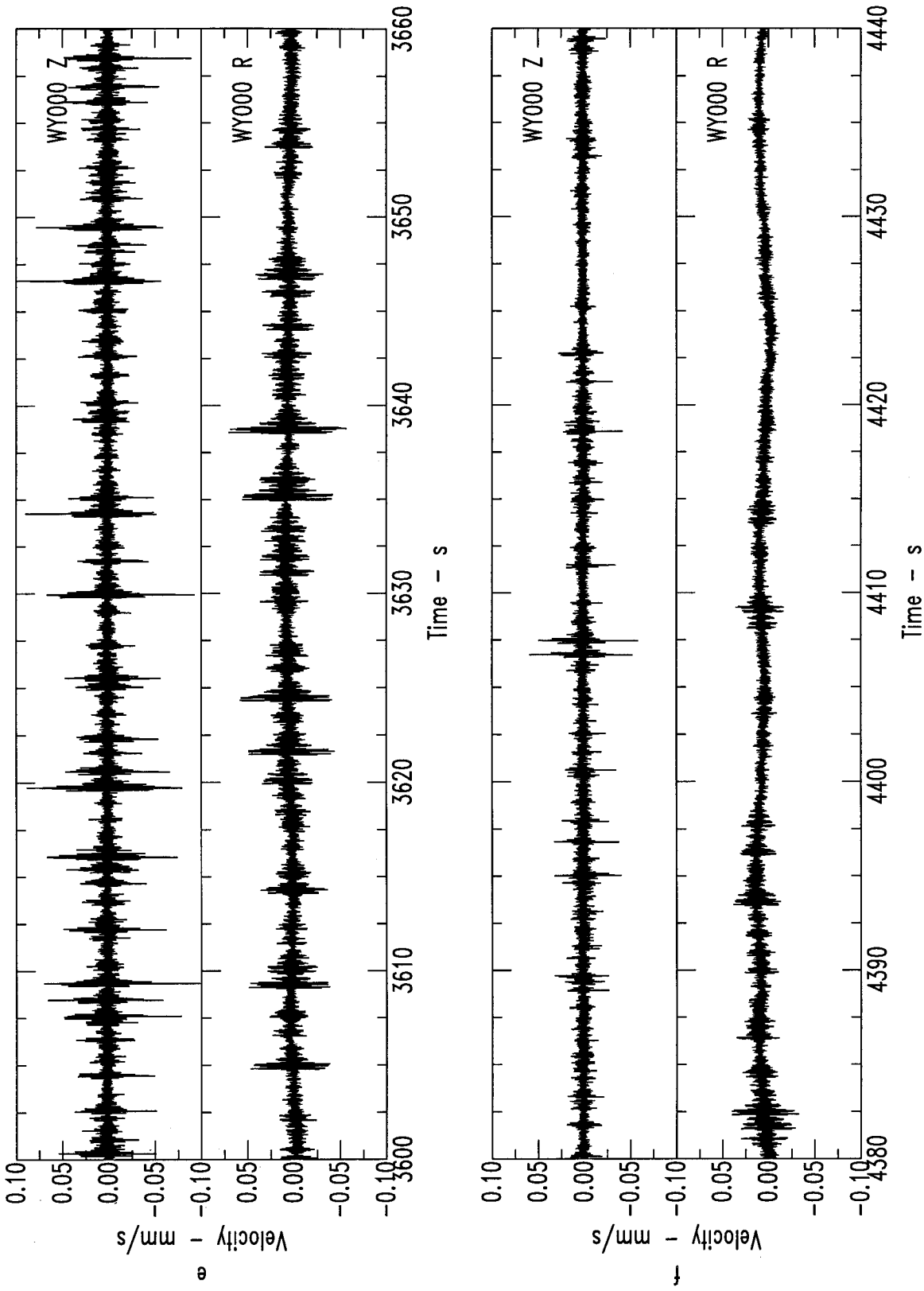

Figure 1.8: A blow up of the 1-minute time window marked **e** and **f** in Figure 1.3.

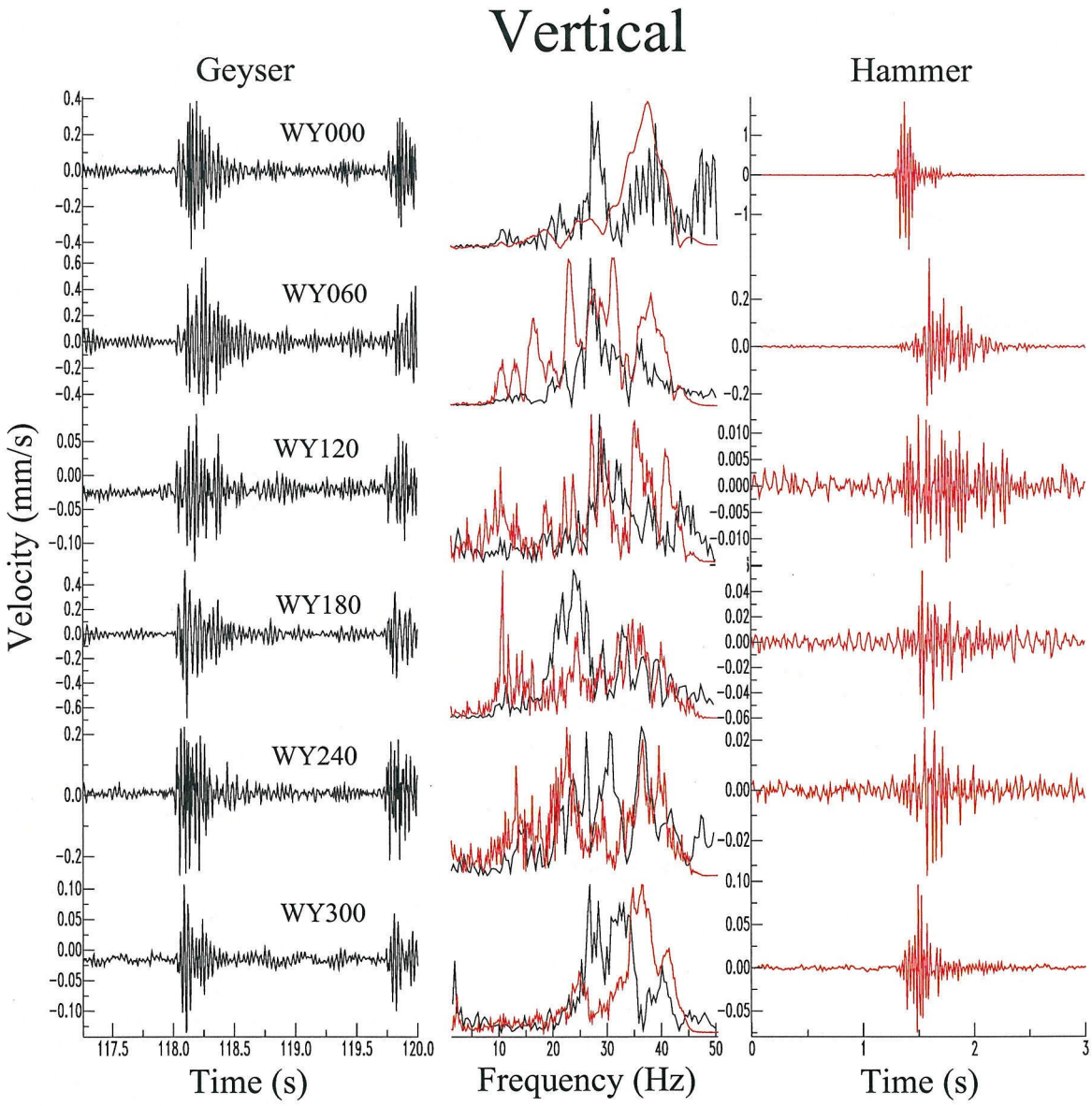

Figure 1.9: Vertical components of a geyser event and of hammer shot 4 along with their Fourier amplitude spectra.

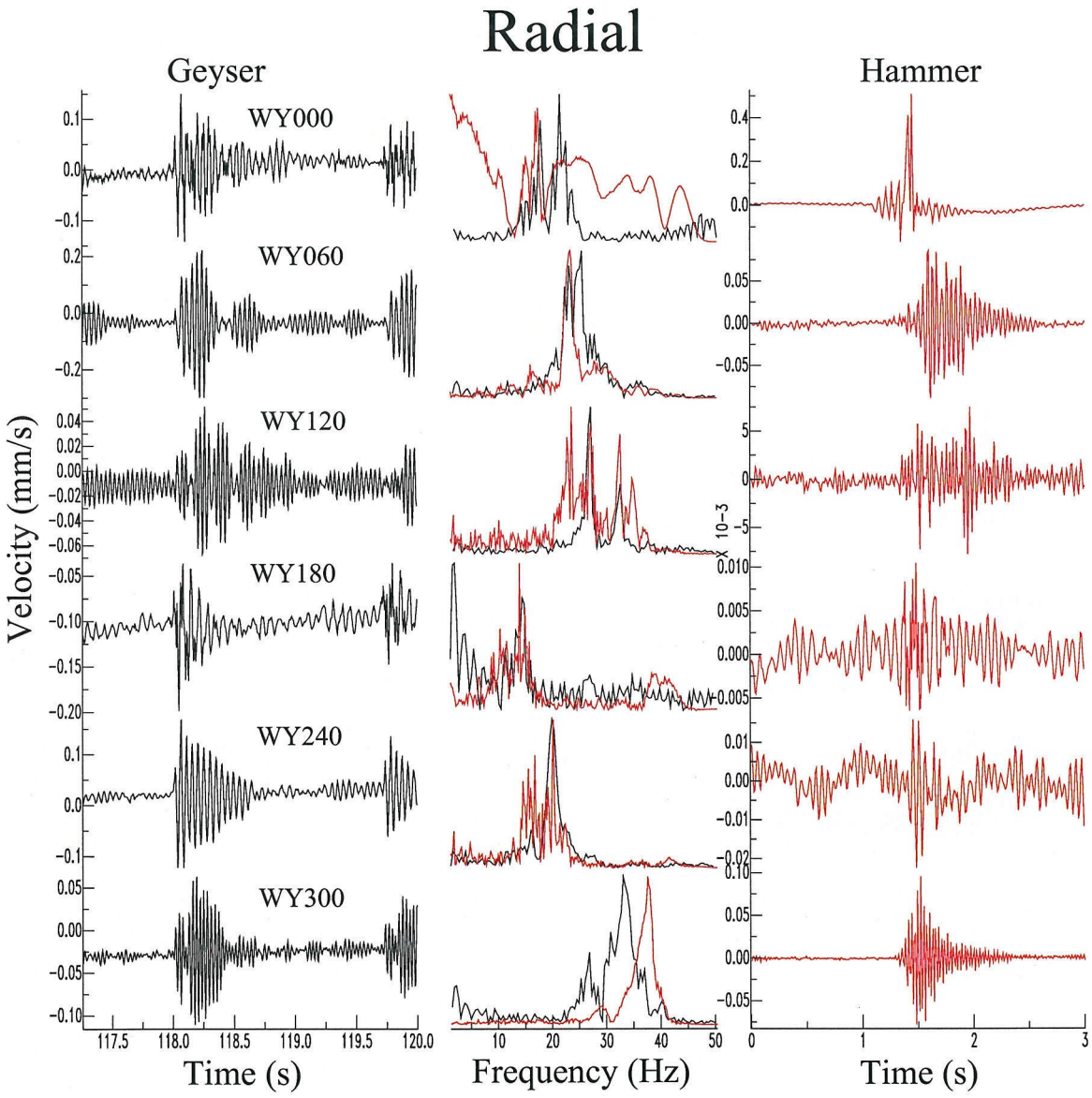

Figure 1.10: Radial components of a geyser event and of hammer shot 4 along with their Fourier amplitude spectra.

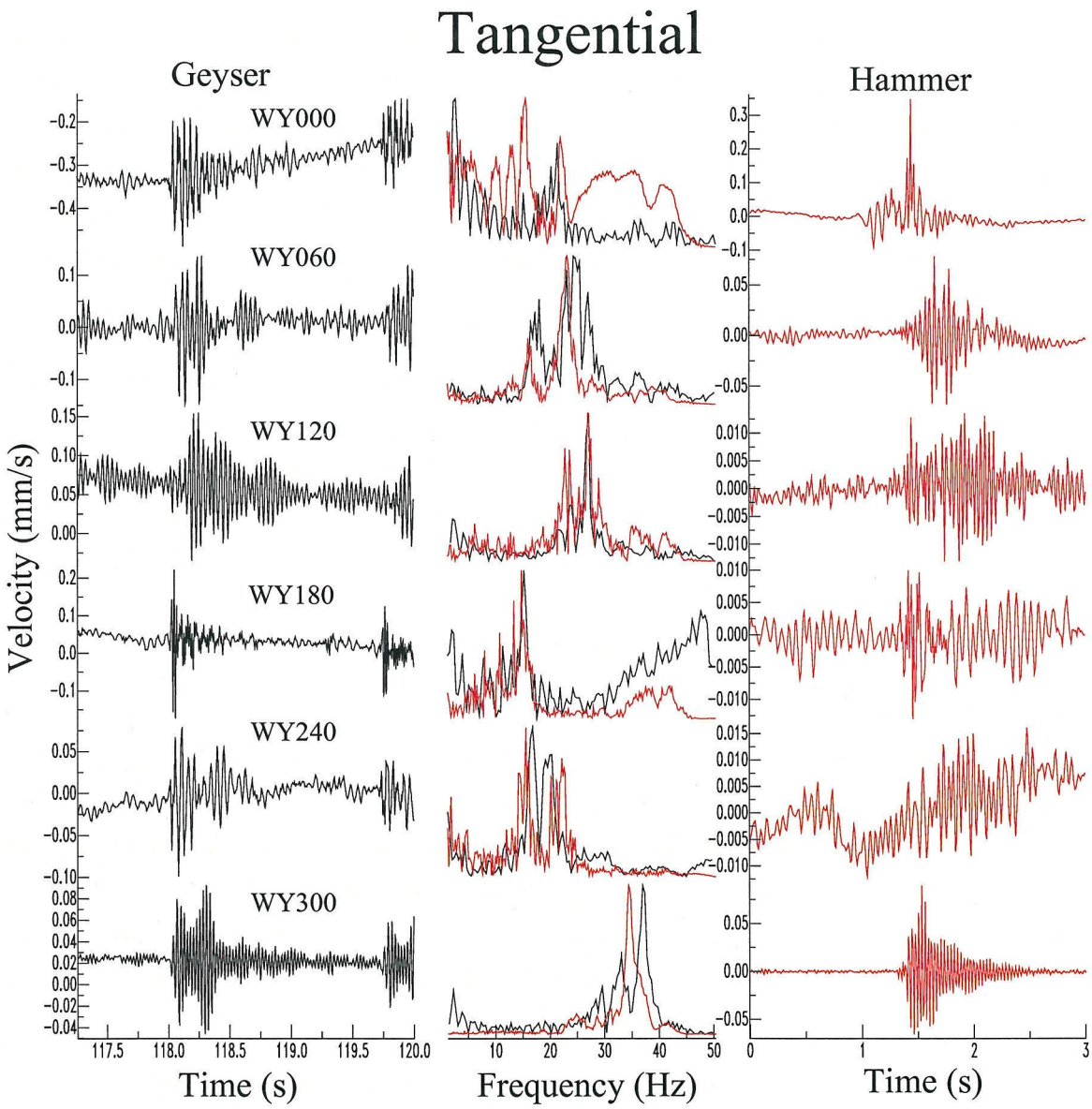

Figure 1.11: Tangential components of a geyser event and of hammer shot 4 along with their Fourier amplitude spectra.

- The frequency of the harmonic signals varies as a function of location. The horizontal components, although all stations display one or two sharp spectral peaks, differ in spectral content and in decay time.

Temporal properties

Figures 1.12 and 1.13 reiterate the above observations. These frequency-time diagrams, known as 'spectrograms', are constructed by calculating the Fourier spectra for a 3min long window, shifting the window one minute forward, and repeating the process. The vertical motion spectrum is clearly broader compared to the radial component, as was stated above. In addition, it is clear that the eruption spectrum is 'white', i.e., all frequencies are more or less equally excited, due to noise generated by water falling on the ground surrounding the orifice. It is apparent that:

- The resonance frequencies do not change with time.

Figure 1.14 illustrates the spatial excitation of the medium by geyser-events at 10-minute intervals. The calculation is done by integrating the square amplitude of a single pulse recorded at each of the 96 geophones and contouring the calculated values over the entire array, thus obtaining a map of the elastic (vertical) energy generated by a pulse within the geyser. It is clear that the excitation pattern hardly changes in time.

1.2.3 Local excitation by a sledge hammer

In order to isolate the medium's impulse response from the source, a sledge-hammer source on the surface was used. The seven shots that were carried out in 1992 (Figure 1.1) were for source comparison only and were not used for an active study of the structure. A much more detailed study was done in 1994, when an array of 24 $100Hz$ vertical geophones was laid out in an attempt to study the shallow subsurface. This portion of the work is described in Chapter 3.
The 1992 sledge-hammer experiment has illustrated the dominant impulse response of the medium, and as is evident from Figure 1.9, Figure 1.10 and Figure 1.11:

- The hammer source, differing in location and in mechanism from the geyser source, is exciting the same spectral peaks excited by the natural source.

Moreover, from Figure 1.15 and Figure 1.14 it is observed that:

- Specific regions in the medium are always excited regardless of the source location.

1.2.4 Simultaneous pressure and seismic measurements

Based on the observations from 1991 and 1992, a probe was designed and built to measure pressure inside the water-column simultaneously with the seismic measurements on the geyser's dome. The

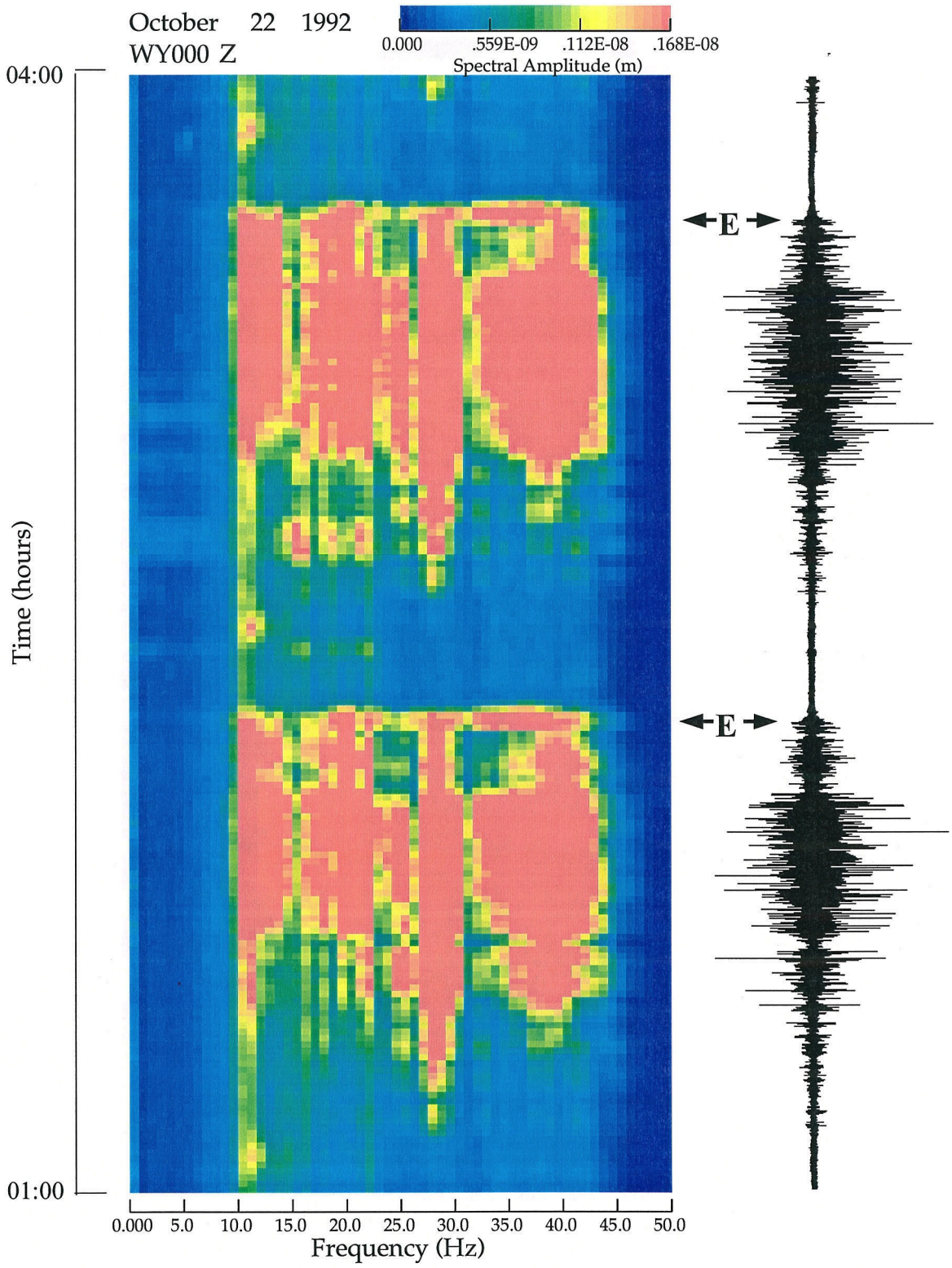

Figure 1.12: A 3-hour spectrogram of the vertical component at station WY000. Eruptions are marked by "**E**."

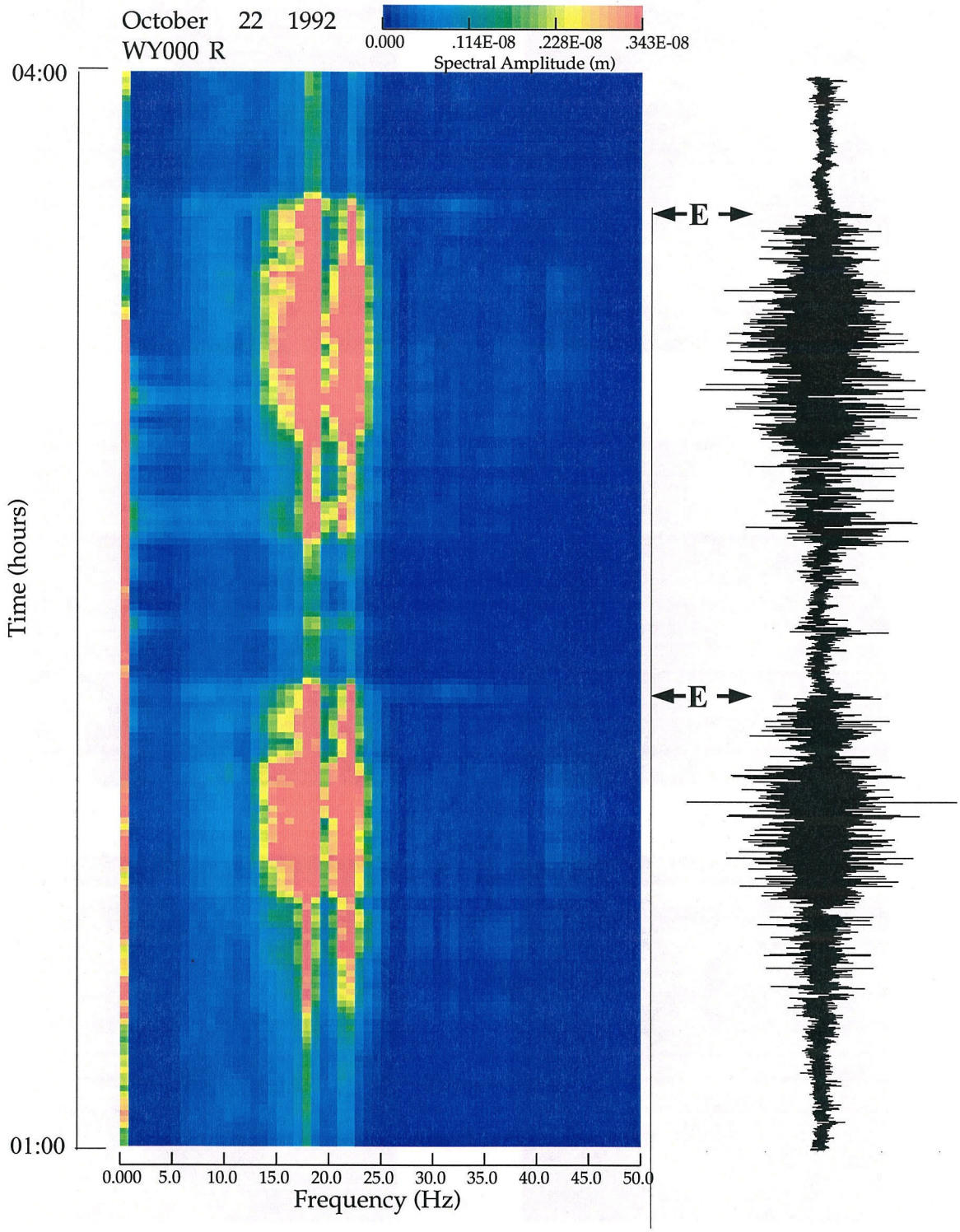

Figure 1.13: A 3-hour spectrogram of the radial component at station WY000. Eruptions are marked by "**E**."

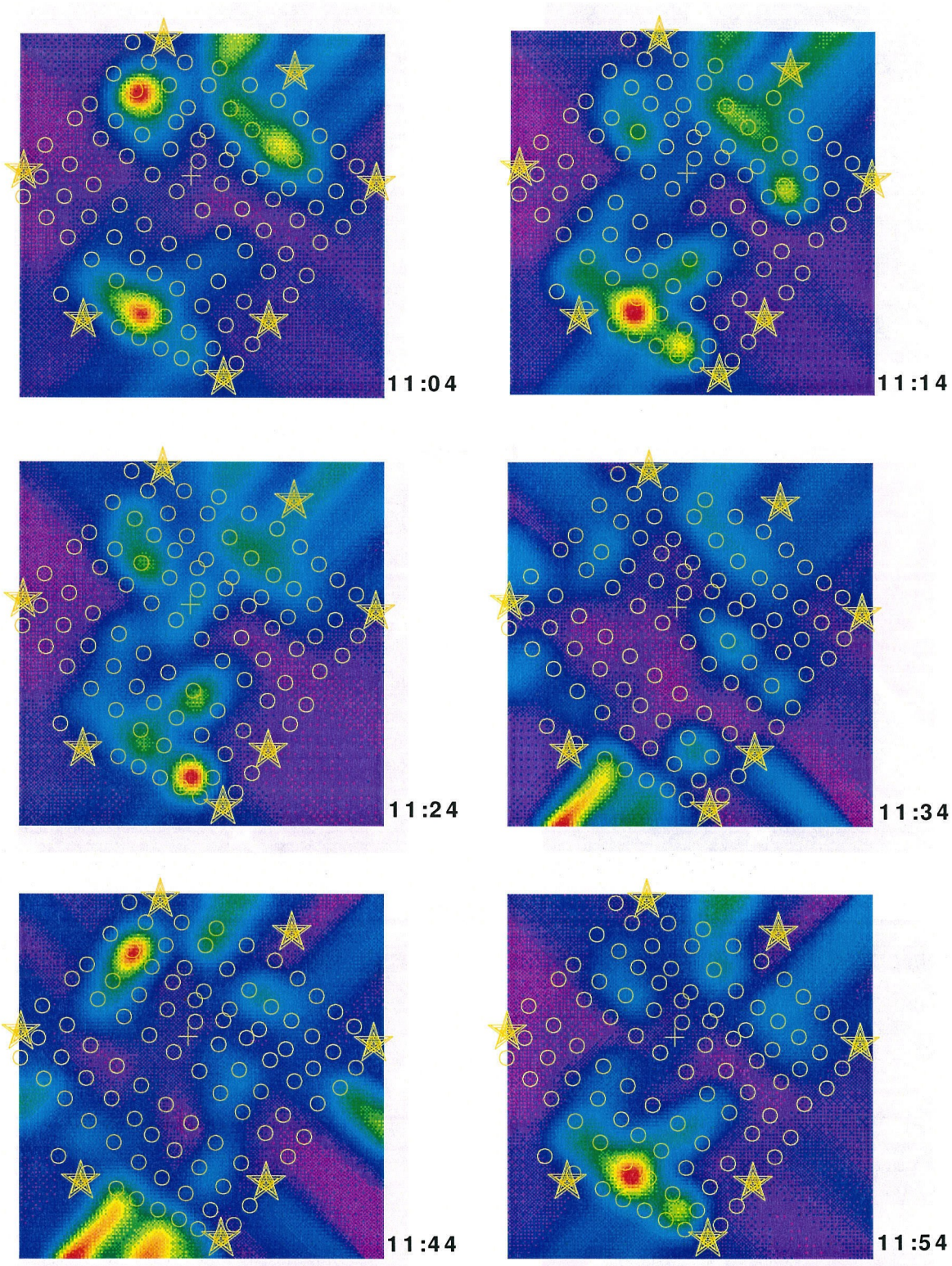

Figure 1.14: An elastic energy map for the medium excitations for six different pulses at 10-minute intervals. Since there is no data outside the array, the contours are smeared towards the edge of the plot. The values outside the array should be ignored.

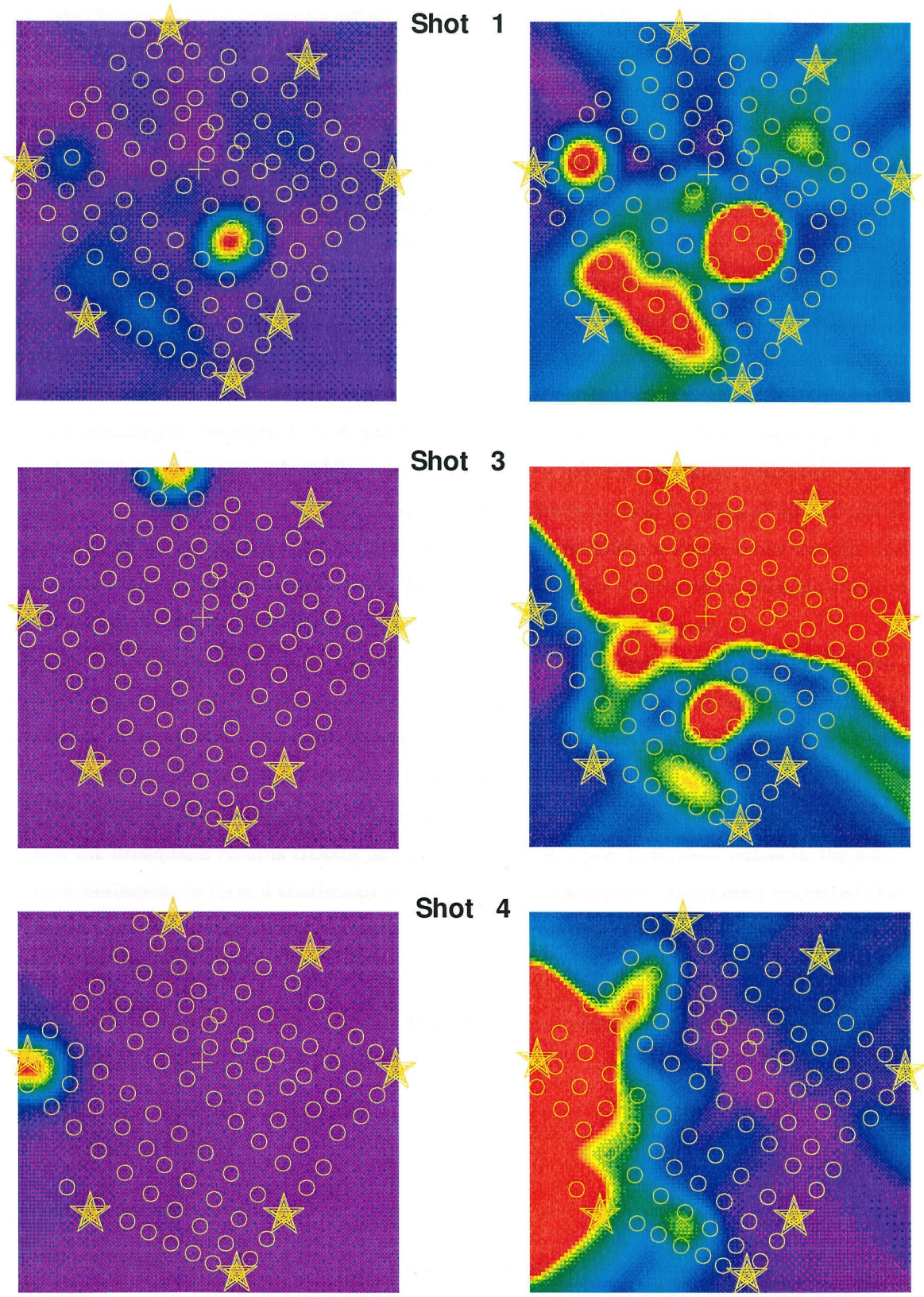

Figure 1.15: Similar to Figure 1.14, elastic energy maps for three different hammer shots are presented. The figures on the right-hand side are clipped versions of the maps on the left which are dominated by the sites in the vicinity of the shots.

instrument consisted of three sensors 3m apart on a coaxial cable, each containing a KULITE XTC-190, high-frequency pressure transducer (Figure 1.16). The instrument was lowered into the geyser's conduit during the quiet period in a long eruption cycle until the bottom sensor was 22 m deep and was below 7 m of water. The recording was made at 250sps simultaneously with 2-broadband sensors and three 3-component short period sensors (L-28, natural frequency 4.5 Hz) for 40 minutes. This last experiment (October 1994) obtained a direct measurement of the source of seismic waves and resolved propagation effects from source effects.

Figure 1.17 displays the $\sim$ 40min-long pressure data recorded inside the conduit of Old Faithful. The amplitude of the pressure traces displayed here for the three pressure transducer is relative to atmospheric pressure. The large drift in the record when the transducers are entering the water at $300s$ is probably due to thermal effect. The malfunctioning of the bottom transducer is attributed to water penetrating its container, thus its record will be ignored hereafter. However, after a period of thermal adjustment, the top and middle transducers display a behavior consistent with their relative locations in the water, and a consistent steady rise in the pressure over a period of 30 minutes as the geyser is filling. Towards the end of the record (1700s) the middle transducer drifts strongly and is followed by the top transducer 300s later. These effects are again attributed to water penetration of the sensor and are not a measurement of any real activity within the geyser.

Figure 1.18 displays a 30s long simultaneous pressure and seismic records (station BD60A) demonstrating a direct correspondence between the pressure pulses and the seismic signals that follow them. A 2s portion of the record shows a single pressure pulse in the water exciting seismic waves. The horizontal components show a strong harmonic behavior.

A 10 s time window displaying the record of the top pressure transducer high-pass filtered at 1Hz and the broadband records BD60A and BD00A (Figure 1.19). Individual pulses in the water column superimpose to form a continuous harmonic seismic wave-train. It has been suggested that in volcanic areas individual harmonic events ('LP events') compose the continuous volcanic tremor.

It is clear, therefore, that:

- The source of harmonic tremor at Old Faithful geyser is impulsive. There is no resonance at the source.

1.3 Summary

Summarizing the observations:

- The harmonic signal is more pronounced in the horizontal components than the vertical component.

- The frequency amplitude of the harmonic signals varies as a function of location.

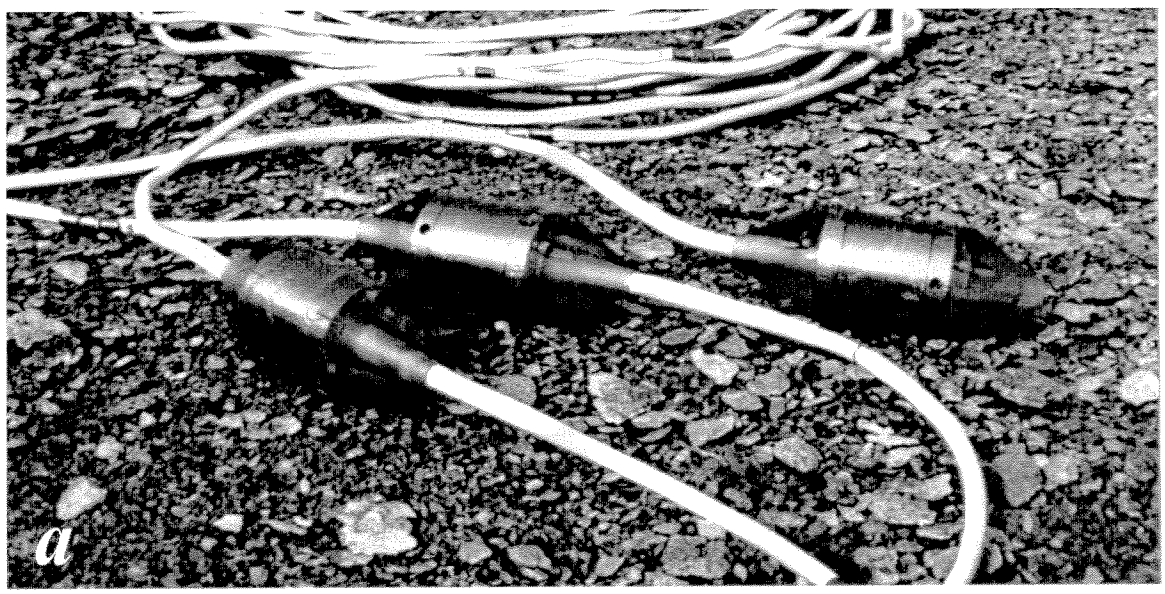

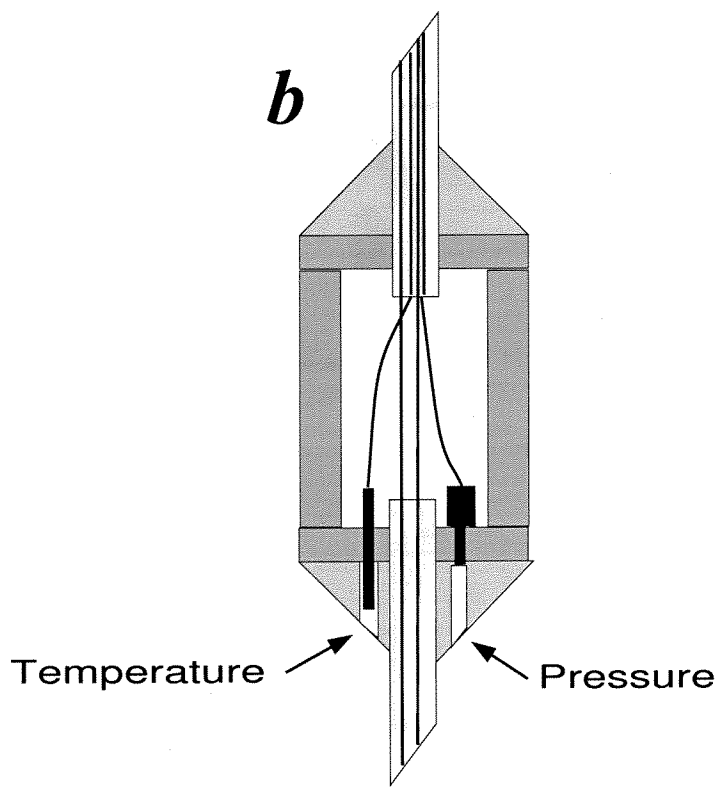

Figure 1.16: a. The three pressure sensors laying on sinter deposits at the foot of Old Faithful's dome; b. A schematic diagram of the interior of the containers.

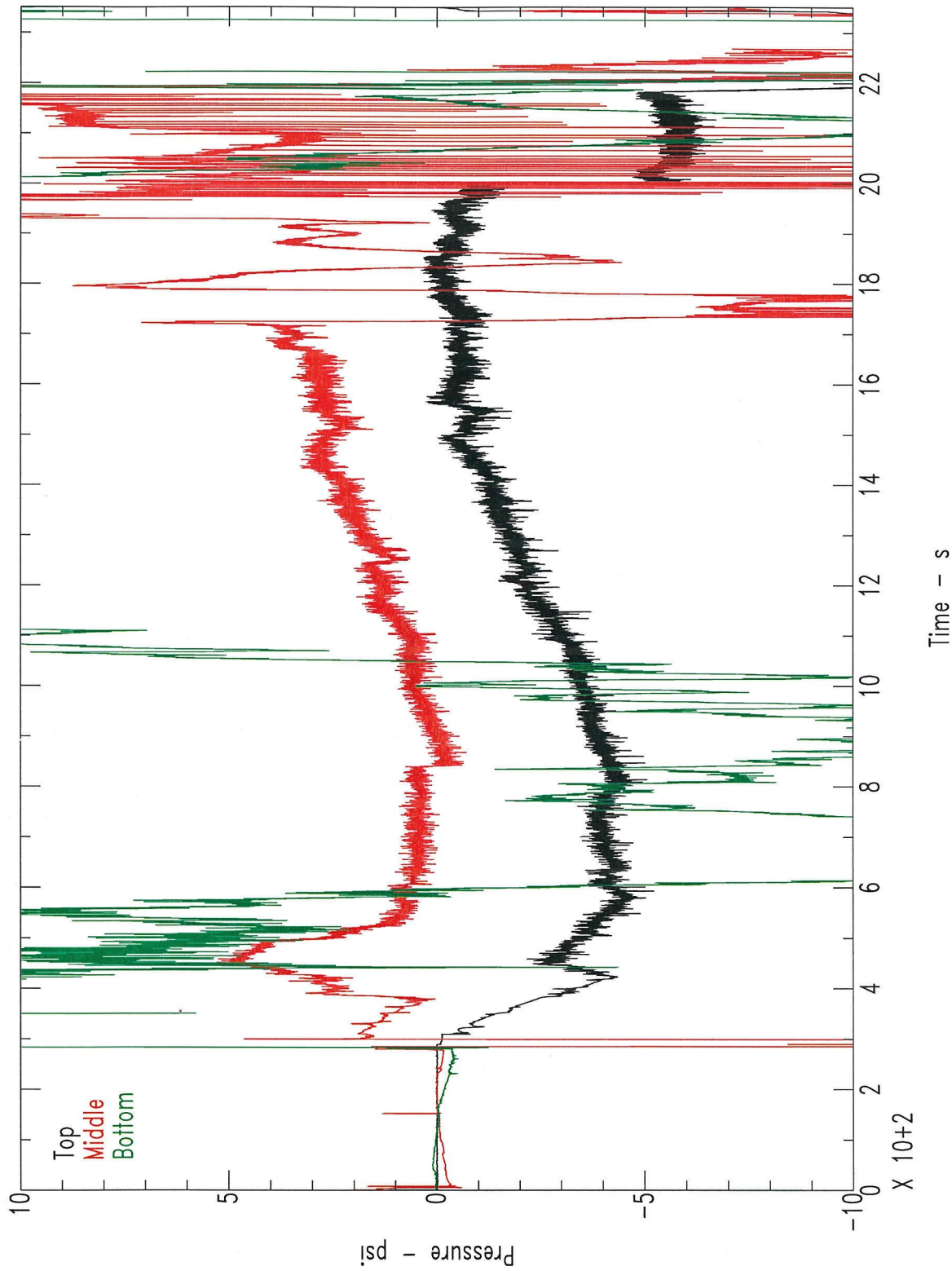

Figure 1.17: The long period behavior of the pressure measured inside the conduit. The top and middle transducer are $3m$ apart, thus the top transducer (Black) is measuring a $\sim$ 5psi lower pressure than the middle transducer (Red). The bottom transducer (Green) is malfunctioning due to water leaking into the container.

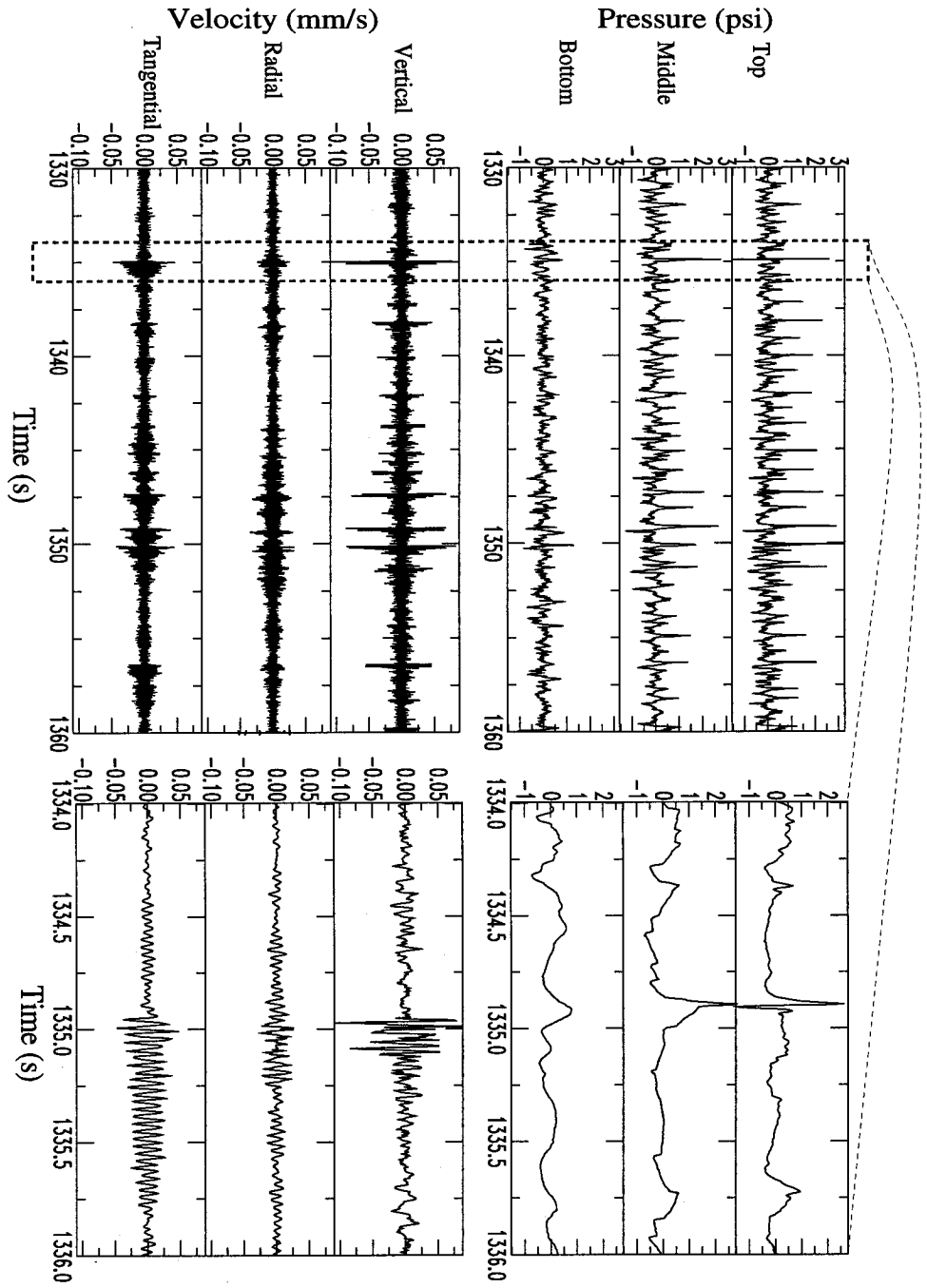

Figure 1.18: A simultaneous record of pressure and seismic waves shows a distinct cause-and-effect relationship between the impulsive source and the impulse response of the medium.

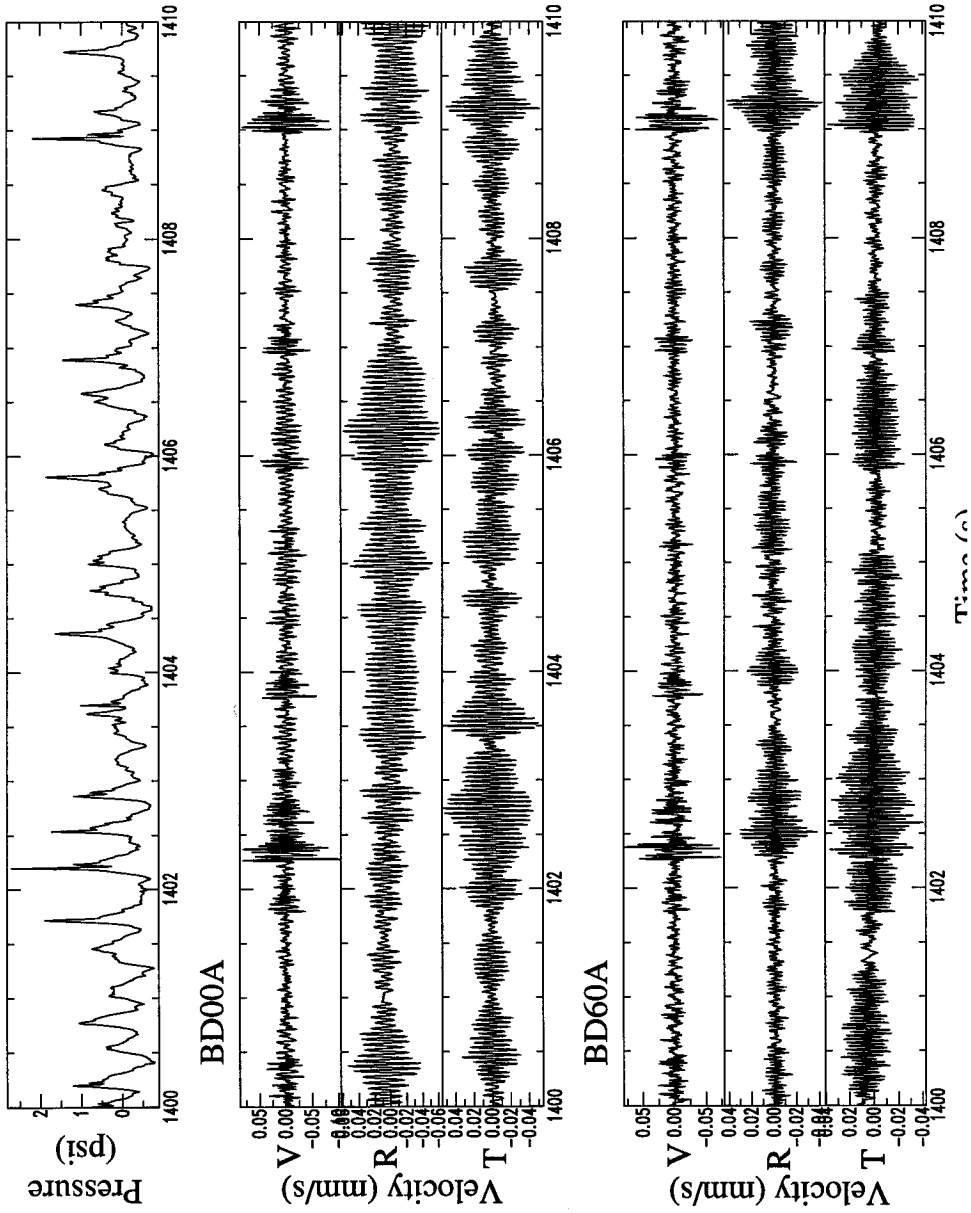

Figure 1.19: A 10s long record demonstrates that continuous tremor at Old Faithful is generated by a superposition of individual pressure pulses inside the geyser.

- The resonance frequency does not change with time.
- The hammer source, differing in location and in mechanism from the geyser source, is exciting the same spectral peaks as the natural source.
- The source of harmonic tremor at Old Faithful geyser is impulsive. There is no resonance at the source.
- Superposition of several pulses appears as continuous harmonic tremor.
- Eruptions are emergent. Excluding a fraction of the eruption which start with a distinct impulse, there are no precursors to the eruption other than amplitude and intensity changes in the eruption cycle.

It is clear, therefore, that harmonic at Old Faithful is fully a path/site effect. There is an obvious cause-and-effect relationship between the impulsive pressure source and the harmonic path effect. This in and of itself is an important observation, particularly because of its possible relevance to volcanic tremor studies, which will be discussed in Chapter 4.

The next two chapters will deal specifically with the source mechanism and the medium's impulse response. Chapter 2 will concentrate on the processes taking place within the fluid: The physics of an individual pulse, and the controls over the intensity of the activity. Chapter 3 will discuss possible explanations for the harmonic impulse response with its special characteristics.

Chapter 2 The Source

In the previous chapter it was established that tremor at Old Faithful originates from sharp pressure pulses at the top of the water column, and that continuous tremor results from the superposition in time of several such pulses. In order to gain further physical understanding on the nature of these processes, two problems are posed:

- What is the impulsive source?
  The physics of an individual pulse, its shape, time scale and amplitude.
- What controls the rate of occurrence of pulses?
  The rate of occurrence of pulses determines whether continuous or impulsive tremor is excited. The filling-rates and heating-rates, the interaction between them and their effect on the rate of pressure pulse excitation, will be discussed.

2.1 Source of impulses

The most common source of repetitive pressure impulses in a column of boiling water is bubble collapse (*Blake* [1986]; *Boure et al.* [1973]), as was suggested by *Kieffer* [1984] and by *Kedar et al.* [1996] in the context of Old Faithful. When a steam bubble rises to some cooler, lower pressure zone in the water column, the steam vapor condenses and the bubble collapses, generating a pressure pulse with a characteristic collapse time τ_c, and sometimes a rebound or several rebounds resulting from an incomplete collapse of the bubble, as is shown in Figure 2.1, and as is frequently observed in the laboratory (*Blake* [1986]). Similarly, when a large bubble of the order of the size of the conduit bursts at the water surface, the displaced mass of water will drop back on the emptied cavity (a process sometimes referred to as 'chugging') generating a pulse. The collapse time τ_c is measured from the moment the pressure starts increasing to the time of the pressure peak as is demonstrated in Figure 2.1 (*Blake* [1986]) and Figure 2.2.

Several examples of pressure pulses showing distinct characteristics of bubble collapse are presented in Figure 2.2. The following discussion will concentrate on modeling the recorded pressure pulses as a bubble collapses.

2.1.1 Rayleigh collapse

The simplest collapse model was calculated by *Rayleigh* [1917] who estimated the collapse time of an empty spherical cavity in a body of incompressible fluid with constant pressure P_∞ at infinity.

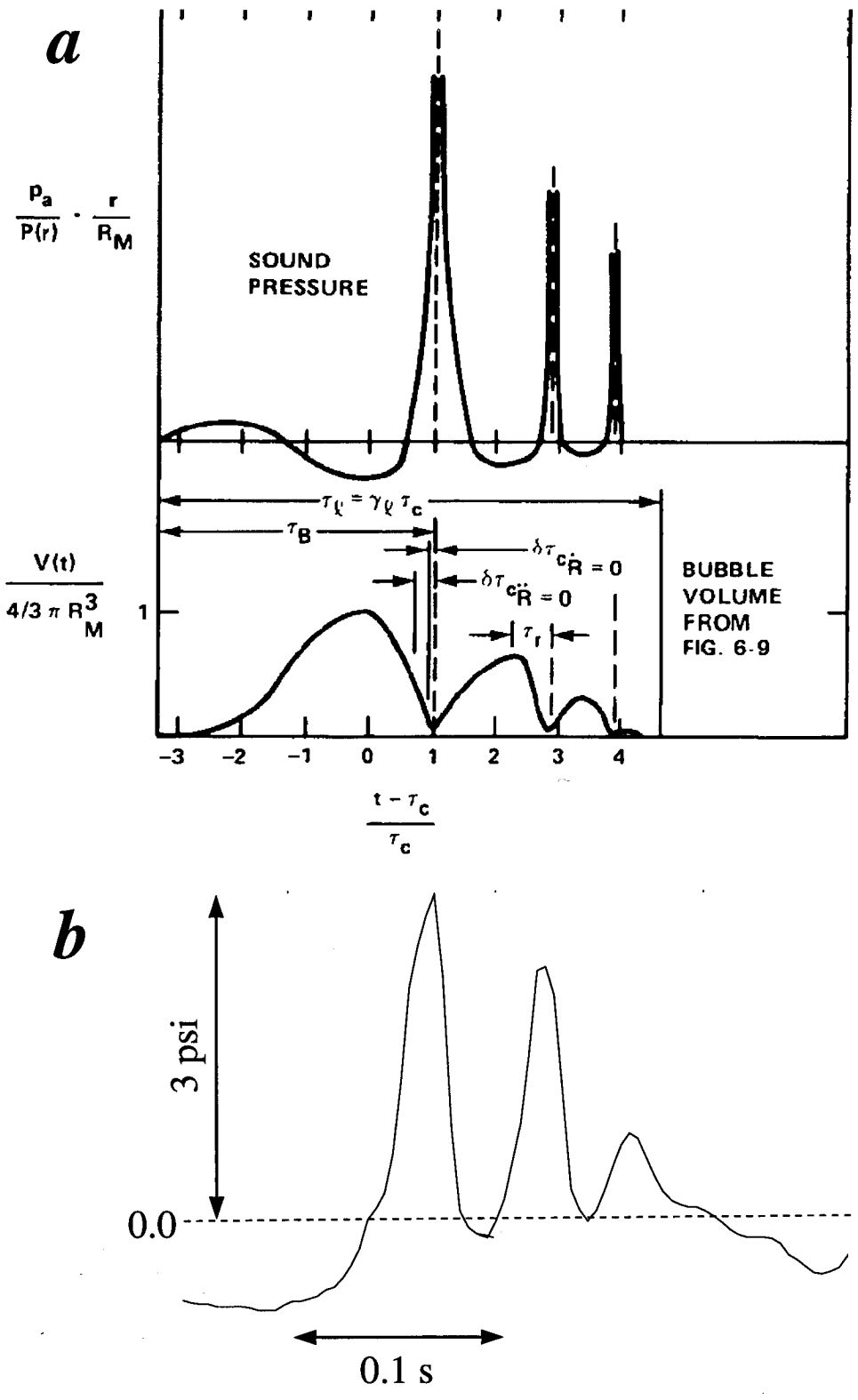

Figure 2.1: Characteristics of bubble collapse comparison between a laboratory measurement (a.) and a pressure pulse recorded on the top transducer inside Old Faithful (b.).

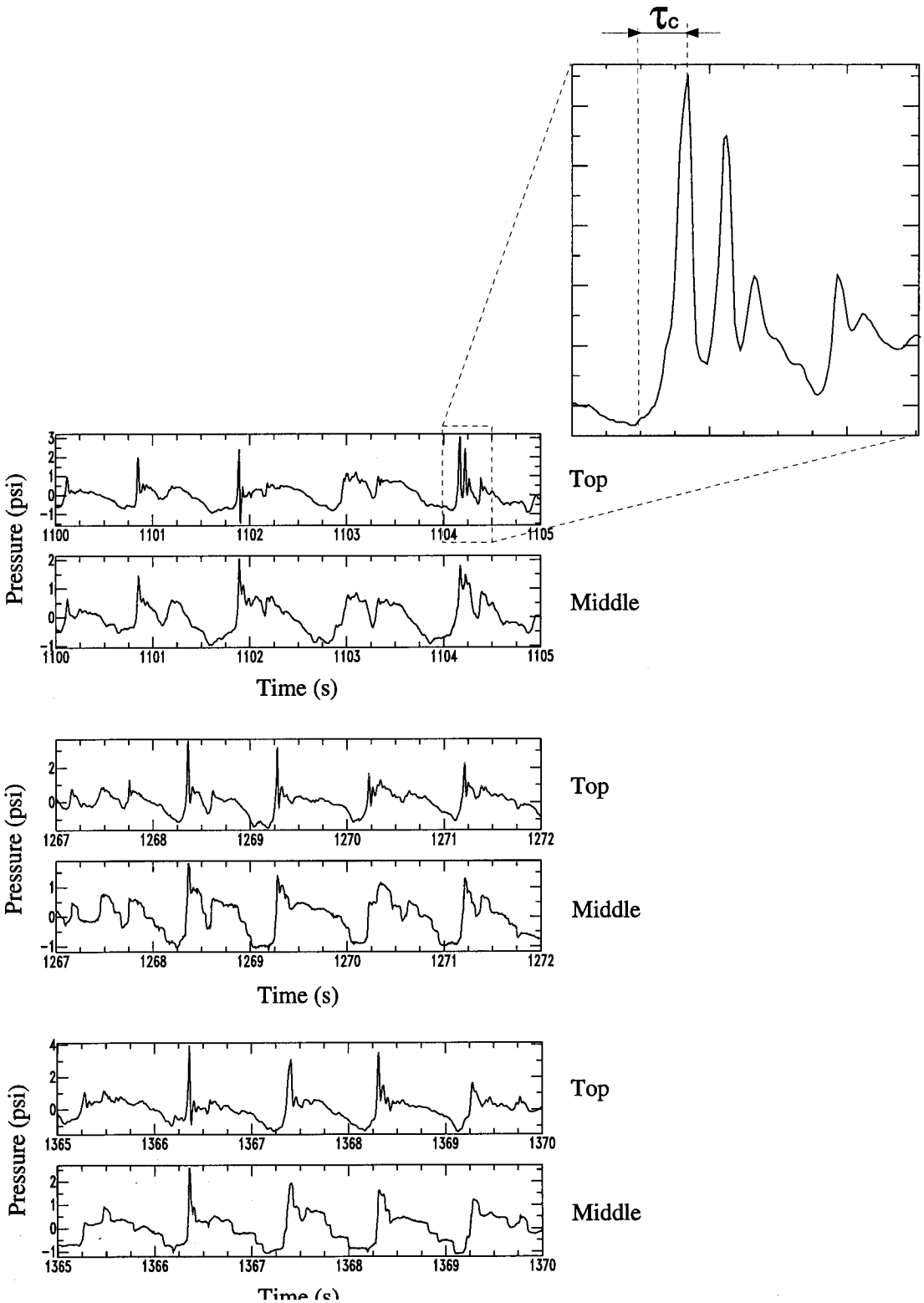

Figure 2.2: Several examples of pressure pulses.

The equation of motion in spherical coordinates is then

$$\ddot{R}R + \frac{3}{2}(\dot{R})^2 = \frac{P(R) - P_\infty}{\rho} = -\frac{\Delta P}{\rho} \tag{2.1}$$

For a spherical void the wall pressure $P(R) = 0$ and the collapse time is

$$\tau_c = 0.915 R_M \sqrt{\rho / P_\infty} \tag{2.2}$$

(For the complete derivation see Appendix B.)

The measured collapse time of individual pulses varies between $0.03 - 0.06s$. Thus, choosing the driving pressure P_∞ to be atmospheric pressure, $10^5 Pa$, and the density of water $\rho = 1000 kg/m^3$, gives for the average observed collapse time $\tau_c = 0.05 \pm 0.02s$ a bubble radius of $R_M \sim 0.5m$. This result is clearly not applicable to Old Faithful since for the most part the geyser conduit is much narrower than $1m$, and at its narrowest point it is only $\sim 0.1m$ wide. The Rayleigh collapse model is an idealized one and does not account for the effect of non-condensible gases cushioning the collapse and so is an upper limit estimation of the collapse radius. Another possible complication is the effect of diffusion of heat generated by steam condensation, through the collapsing bubble wall.

2.1.2 The role of non-condensible gases

Assuming an adiabatic collapse, the pressure-volume relationship is

$$P_g(V) = P_{g0} \left(\frac{V_0}{V} \right)^\gamma \tag{2.3}$$

Where P_g is the gas pressure inside the bubble, P_{g0} is the initial non-condensible gas pressure, V and V_0 are the bubble time-dependent volume and initial volume respectively, and γ is the specific heats ratio. In this case the term ΔP in equation 2.1 becomes

$$\Delta P = P_\infty - P_v - P_g(V) \tag{2.4}$$

where P_v is the vapor pressure of condensible gases inside the bubble, and the equation of motion becomes:

$$\ddot{R}R + \frac{3}{2}(\dot{R})^2 = \frac{1}{\rho} \left[P_v + P_{g0} \left(\frac{R_0}{R} \right)^{3\gamma} - P_\infty \right] \tag{2.5}$$

The solution is obtained by a 4^{th} order Runge-Kutta numerical integration and several calculations are shown in Figure 2.3, which presents the time history of collapse processes for several different values of P_{g0} for a given R_0 and ΔP. The limiting case $P_{g0} = 0$ describes a Rayleigh collapse. As the non-condensible gas pressure increases, the bubble oscillates with increasing period and decreasing amplitude.

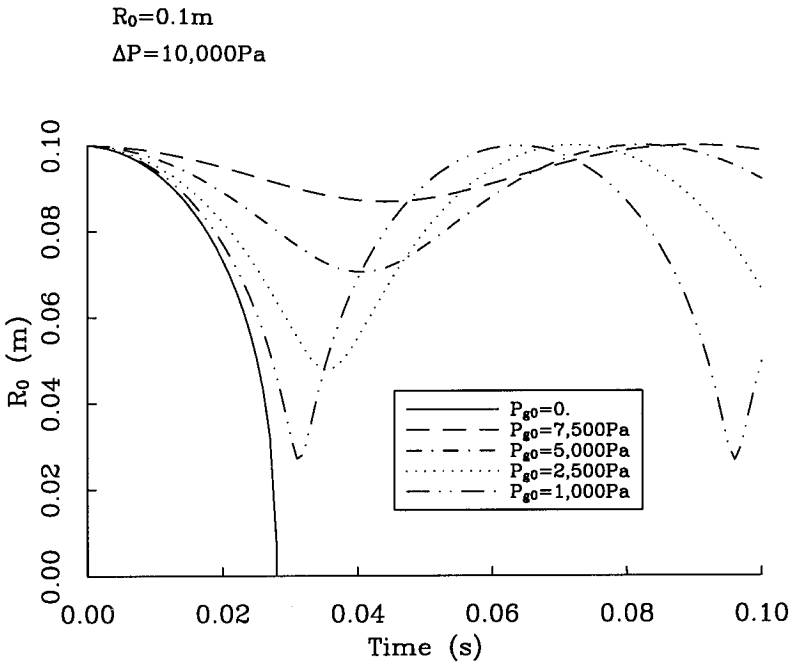

Figure 2.3: Calculation of spherical bubble collapse history with non-condensible gases.

In the small oscillations limit, when $R \to R_0$, the linearized form of equation 2.5 is

$$\ddot{R}R_0 = \frac{1}{\rho}\left[P_v + P_{g0}\left(1 + 3\gamma\frac{R_0 - R}{R_0}\right) - P_\infty\right] \tag{2.6}$$

2.1.3 Damping

Damping plays an important role in the collapse process as can be seen from Figures 2.1 and 2.2. Adding a viscous damping term to equation 2.5 we obtain what is known as the Rayleigh-Plesset equation (*Plesset* [1949]).

$$\ddot{R}R + \frac{3}{2}(\dot{R})^2 = \frac{1}{\rho}\left[P_v + P_{g0}\left(\frac{R_0}{R}\right)^{3\gamma} - P_\infty\right] - \frac{4\nu}{R}\dot{R} \tag{2.7}$$

where ν is the kinematic viscosity of the surrounding fluid. For water at $\sim 100°C$, $\nu = 10^{-6}m^2/s$, resulting in a negligible damping term for the models shown in Figure 2.3, since the minimum radius is never small enough to increase the damping force to the magnitude of the pressure or inertia forces. Nonetheless, damping does occur, and some other mechanism needs to be pursued for the bubble sizes discussed here. The approach taken here is to replace ν in equation 2.7 by an effective viscosity, ν_E, that will generally fit the data, and consequently explain its magnitude.

The effect of damping on the amplitude as well as the frequency of oscillations is illustrated in Figure 2.4. Again, the amplitude and the frequency of oscillations are coupled, so that the effective viscosity causes a longer period of oscillation.

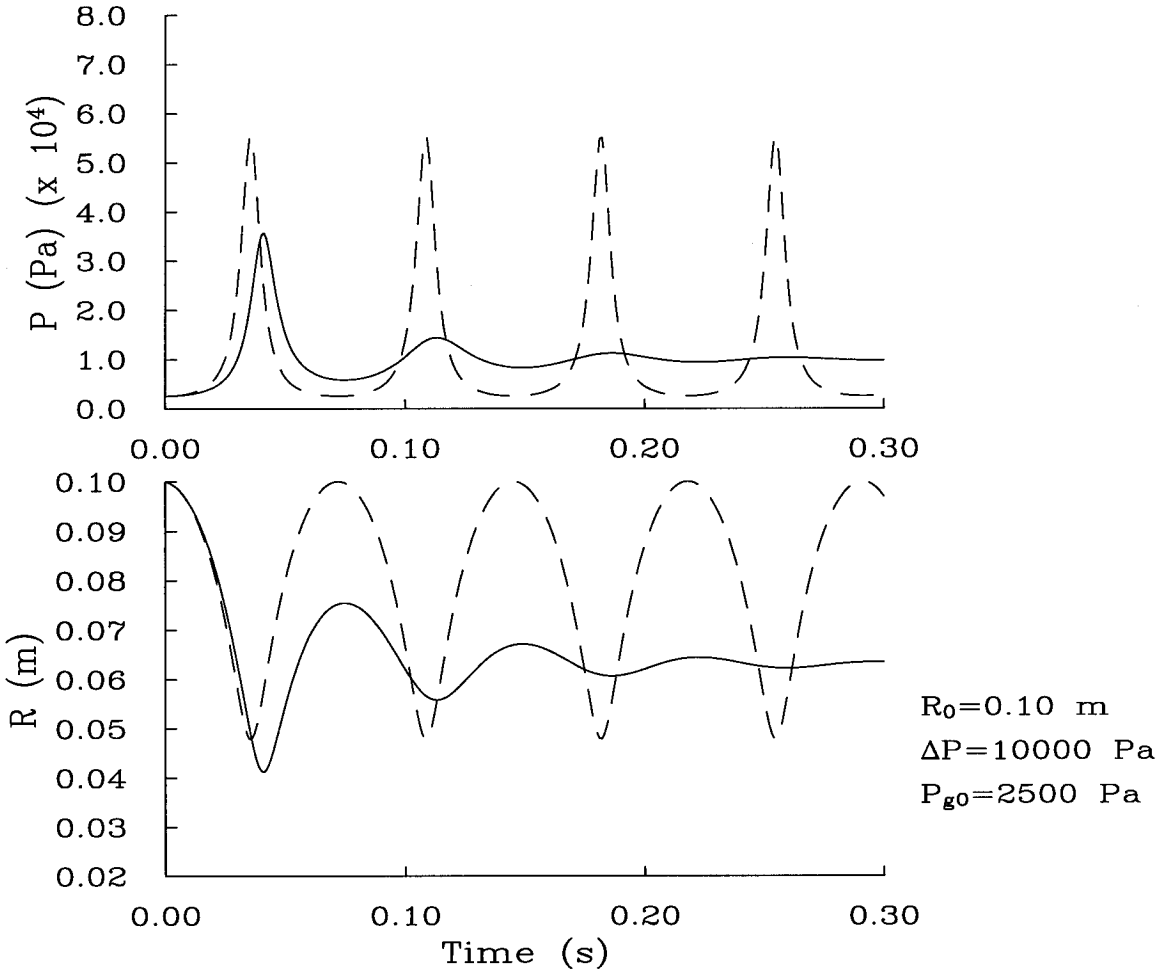

Figure 2.4: Comparison between damped bubble oscillations (solid line) and undamped oscillations (broken line). Note the change of period as well as amplitude. An effective viscosity of $0.03m^2/s$ was used.

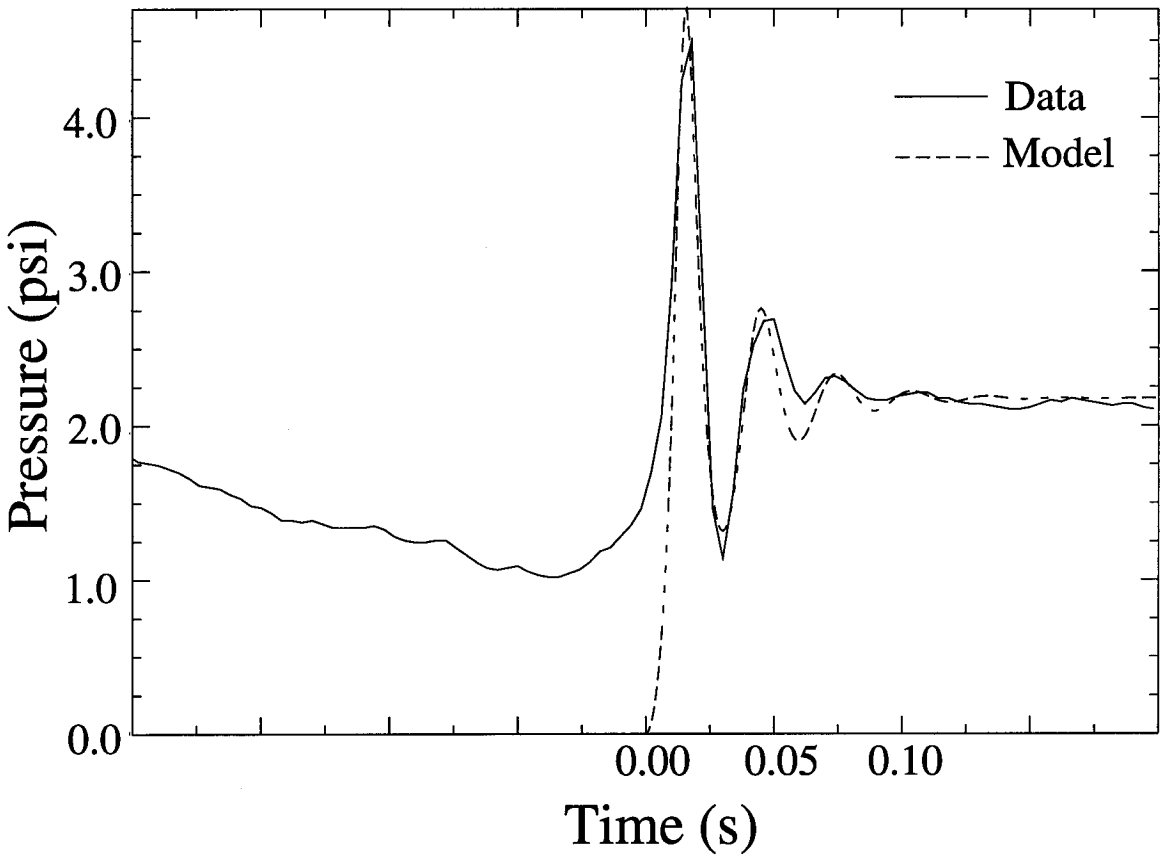

Figure 2.5: A bubble of initial radius $R_0 = 5.5cm$, internal pressure $P_{g0} = 0.2Bar$, feeling a driving pressure $\Delta P = 0.3Bar$ and $\nu_E = 0.04m^2/s$. The driving pressure is equivalent to the weight of $3m$ of water. Note that the zero level was chosen arbitrarily, since only the collapse process (not the inflation) is illustrated here.

In Figure 2.5 an effective viscosity $\nu_E = 0.04m^2/s$ and an isothermal process ($\gamma = 1$) were assumed in order to obtain a good fit to the data. The model successfully describes the general characteristics of the process, namely the period of oscillation, the overall damping, and a net pressure buildup through the process.

As was shown by *Chapman and Plesset* [1971] at large bubble radii, the effective viscosity is significantly larger than the liquid viscosity due to energy lost by radiation and thermal diffusion (in which case the collapse process is no longer adiabatic $\gamma \neq 1.4$). Therefore:

$$\mu_E = \mu_l + \mu_A + \mu_T \tag{2.8}$$

where μ_E is the effective viscosity, and μ_l, μ_A, and μ_T are the liquid, acoustic and thermal viscosities, respectively. It follows that at radii of a few centimeters for water-air mixture, the acoustic viscosity dominates (*Chapman and Plesset* [1971]), and for small oscillations it is:

$$\mu_A = \frac{\rho\omega^2 {R_0}^3}{4c_l} \tag{2.9}$$

where ω is the bubble oscillation frequency, and c_l is the speed of sound in the liquid. For the observed frequency of $\omega \sim 30Hz$ with $c_l = 1500m/s$, and a collapse radius of $0.05m$, $\mu_A \sim 0.1kg/(ms)$ which results in an effective dynamic viscosity $\nu_E \sim 10^{-5}m^2/s$, three orders of magnitude smaller than the viscosity used in Figure 2.5. If the region of collapse contains 10^{-3} mass fraction of steam c_l can be as low as $20m/s$ (*Kieffer* [1977]), and then $\nu_E \sim 10^{-3}m^2/s$, still an order of magnitude too small. Therefore, we must conclude that other effects may account for the strong damping observed.

A hint for the possible dissipation mechanism may be found in the lack of resonance in the water column. Analysis of arrival times of the pressure pulses at the three sensors indicates that most of the pressure pulses arrive at the top sensor first, implying that they originate near the top of the water column. The average arrival time difference between the top two transducers is $\sim 0.002 \pm 0.002$ (i.e., one sample period) which may constrain the speed of sound in the two-phase water-steam fluid in the geyser to a lower bound of about $1500m/s$, the speed of sound in water, in which case the main source of dissipation would be a scatter of irregularities in the conduit walls rather than the fluid compressibility.

Figure 2.6 presents the time record as well as the corresponding Fourier spectra for five seconds of pressure data recorded at the top and middle pressure transducers. From the time record it is clear that very little dispersion, if any, is observed. However, the dissipation is frequency dependent, where frequencies higher than $\sim 20Hz$ have lower amplitude at the middle transducer compared to the top, while the lower frequencies are hardly dissipated at all. A mechanism that might have the above characteristics is the viscous forces felt by a cloud of bubbles under compression. In this

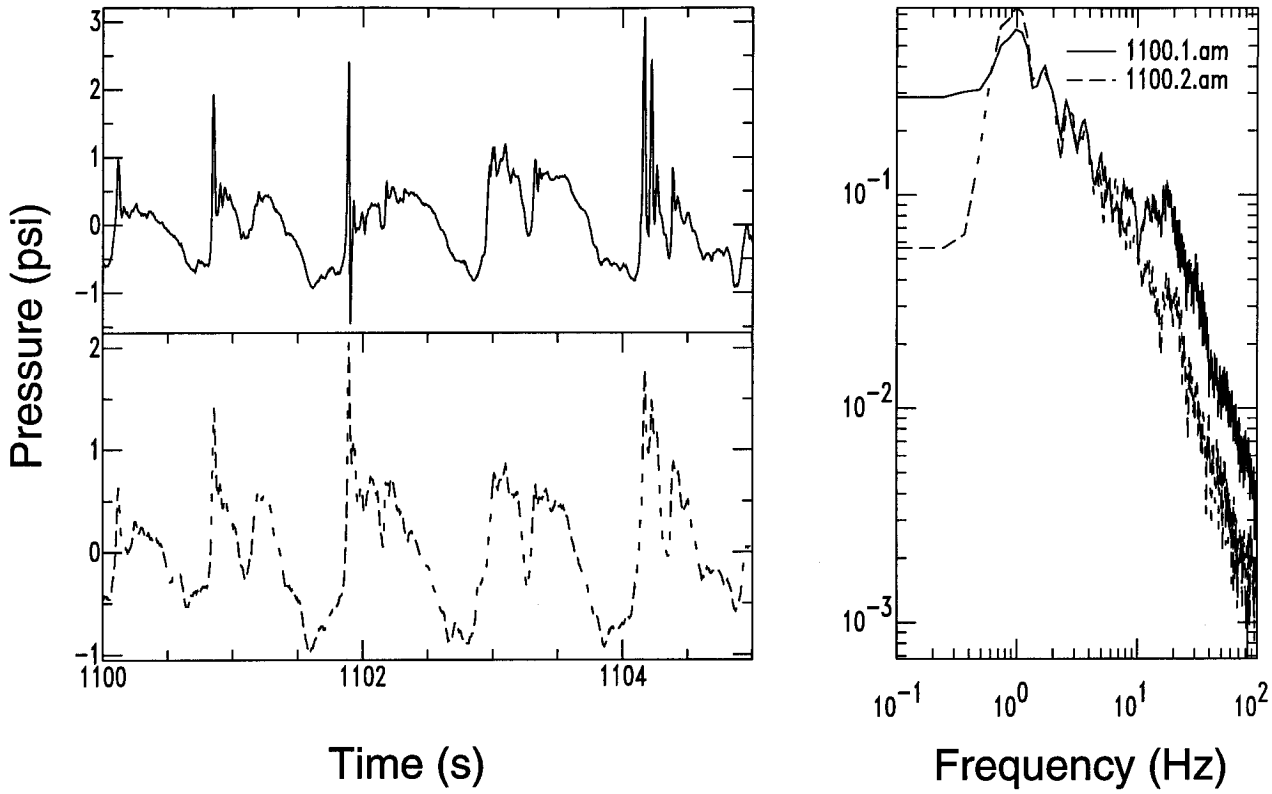

Figure 2.6: A $5s$ long time window of the top (solid line) and middle (broken line) pressure sensors and their corresponding Fourier amplitude spectra. Dissipation is significant only above $10Hz$.

case the fluid viscosity will play an important role as liquid is squeezed between the bubbles during expansion and compression of the cloud. For a speed of sound of $\sim 20m/s$, the wavelength at $20Hz$ is $\sim 1m$. At the same time for pure water at $1Hz$, the wavelength is $1500m$. If the bubble cloud is near the top of the water column, as is suggested by the video shots of Westphal, Kieffer and Hutchison [Personal communication], then wavelengths of the order of the cloud dimension will be strongly dissipated within that region, whereas wavelengths several times longer the bubbly zone will be dominated by the larger portion of fluid in the column where the volume fraction of steam is significantly lower.

2.2 Event rate

Several dynamic processes can cause regular pulsation in a super-heated pipe full of coolant, as was discussed in numerous nuclear engineering studies (*Boure et al.* [1973]). Such regular instabilities are generated when the fluid in the system fluctuates between two thermodynamic states, i.e., when a small thermodynamic perturbation can result in an instantaneous phase change. The excitation of this type of two-phase instabilities is strongly dependent on the heat and mass flux in and out of the system, and the geometry of the system.

In this section the interaction between these parameters, and their influence on the event rate in the water column, will be discussed. Rather than provide a detailed description of the dynamics of the instabilities, the problem is going to be treated as quasi-static, making the following assumptions:

- The fluid is well mixed, i.e., isothermal.
- Each pulse releases a quantum of heat.
- The rate of occurrence of pulses is solely dependent on the heating rate of the fluid in the conduit, i.e., a pressure pulse corresponding to a cooling event occurs when the temperature in the fluid reaches a certain threshold of super-saturation.

The advantage of these assumptions is that the fluid in the conduit is a well defined control volume whose temperature history is completely determined by the amount of heat per unit mass in it, while no consideration of processes within the control volume such as heat or mass transport is necessary. These assumptions are simplistic, as temperature gradients are known to exist in the column; the pulse amplitude fluctuates, and as was mentioned before, dynamic constraints on the pulse rate are likely to exist. However, as will be demonstrated, significant insight into the heating process of the water column can be gained, with the above assumptions, as simple as they might be. This calculation should be treated as a thought experiment rather than an attempt to exactly model the dynamic behavior of the geyser.

2.2.1 Event rate - data

Since only a 30-minute-long pressure record inside the water column was obtained, the rate of seismic events (of which we have a day-long record) is used to characterize the long-term behavior of the source. Figure 2.7 displays a count of the events recorded at station WY000, during a 12-hour period on October 21, 1992. The events were counted by a computerized counter that was designed to detect the events energetic enough to appear distinctly above noise level. As was presented in Figure 1.18, there is in general good correspondence between the seismic events and the pressure pulses during the period in which both are recorded. An inaccurate count may arise in the last few minutes before eruption, due to the general increased noise level causing individual events to become less distinct.

It is apparent that the number of events per minute increases over a time scale of about 20-minutes when it decreases suddenly, then increases to plateau for another 30-40 minutes. This general behavior fluctuates between different eruption cycles, and fluctuations further increase as the eruption nears. However, an attempt will be made to describe a model which accounts for the general behavior observed, namely, the 20 minute rise, the sudden decrease and the final plateau as depicted by a broken line in Figure 2.7.

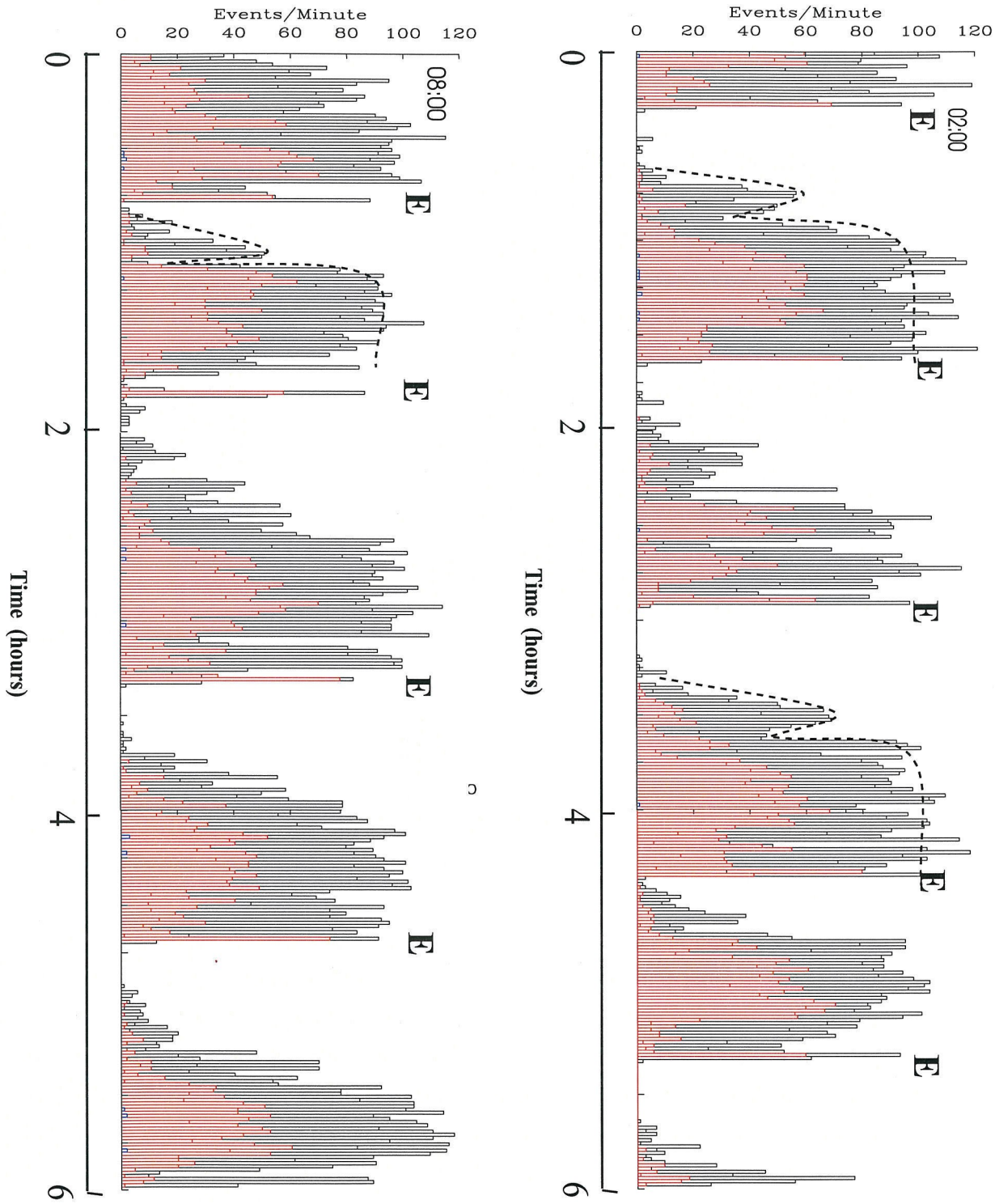

Figure 2.7: Event rate at WY000 inferred from a 12-hour long record. The red histograms represent event counts of energy ten times higher than the black histograms. The general trend to be modeled is outlined by a dotted line. Eruptions are marked by "E."

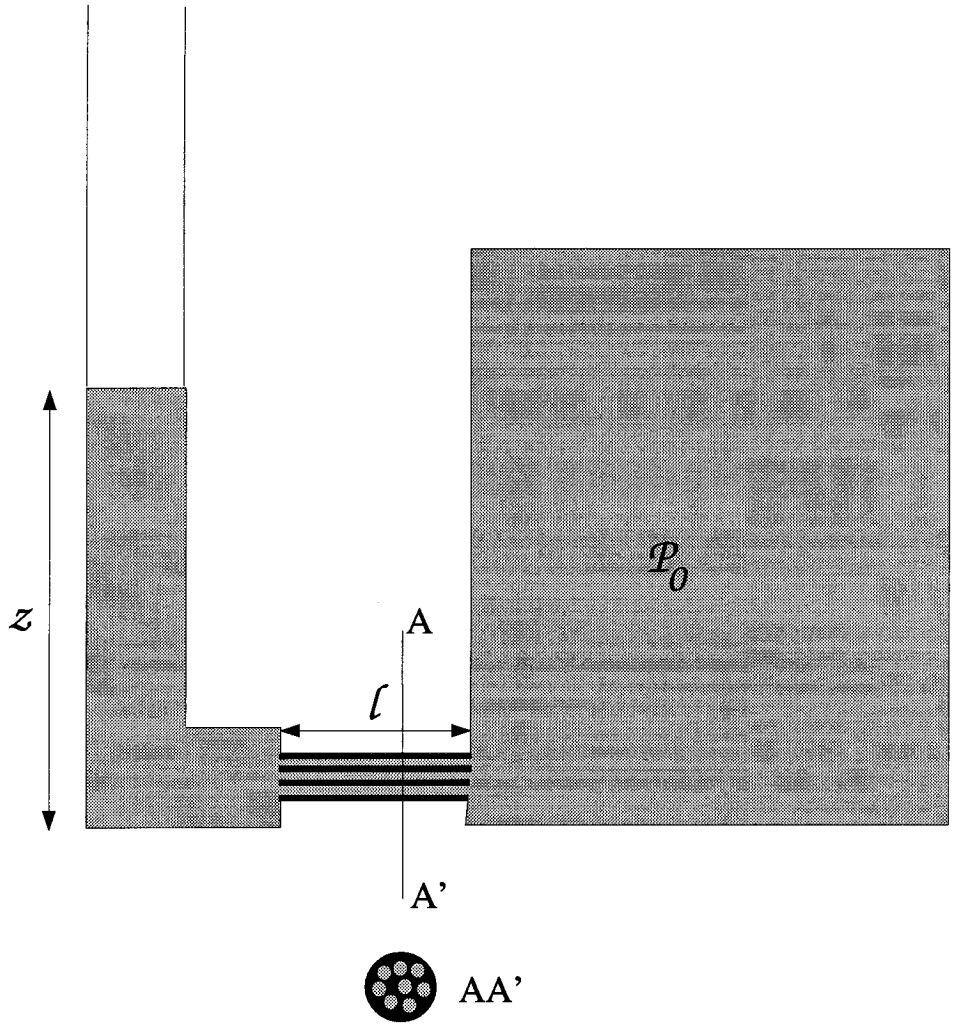

Figure 2.8: Filling model.

2.2.2 Filling rate

Consider the system displayed in Figure 2.8. A tank with liquid of density ρ at pressure p_0 is connected to a pipe of cross section area A, through a network of n pipes of radius a and length l. At time t_0 a valve is released and the fluid flows through the thin pipes and fills the larger pipe. We assume that the tank volume is sufficiently large compared to the volume of the pipe, so that the forcing pressure stays p_0 for the duration of the filling process. First we treat the time history of the water level rise in the pipe. The average velocity u_{av} in one of the thin pipes, assuming that inertial forces are negligible (i.e., that the flow through the pipe is Poissueille flow) is

$$u_{av} = \frac{p_0 - \rho g z}{l} \frac{a^2}{8} \frac{1}{\mu} \tag{2.10}$$

where μ is the viscosity of the fluid. From conservation of mass we get

$$u_{av} = \dot{z}\frac{A}{n\pi a^2} \tag{2.11}$$

where $\dot{z}$ is the time derivative of the water level in the big pipe.

Therefore, the equation of motion for z is

$$p_0 - \rho g z - \alpha \dot{z} = 0 \tag{2.12}$$

where

$$\alpha = \frac{8A\mu l}{n\pi a^4} \tag{2.13}$$

The above discussion can be similarly formulated in terms of the medium's permeability, κ. Using Darcy's law for fluid flow in porous media

$$u = -\frac{\kappa}{\mu}\frac{dp}{dx} \tag{2.14}$$

then

$$\alpha = \frac{\mu l}{\kappa} \tag{2.15}$$

So for the pipe model

$$\kappa = \frac{\pi}{8}\frac{na^4}{A} \tag{2.16}$$

Integrating Equation 2.12 we get

$$z(t) = \frac{p_0}{\rho g}\left[1 + Ce^{-\left(\frac{\rho g}{\alpha}\right)t}\right] \tag{2.17}$$

where C is a constant of integration determined from the initial conditions. For the initial condition $z(t=0) = 0$, $C = -1$.

Figure 2.9 illustrates the filling rate history for different values of α, the constant determining the duration of the filling process. p_0 scales the height of the equilibrium point and is $1MPa$ in Figure 2.9. Comparing the time scales of Figure 2.9 to the pressure history measurement obtained by Westphal and Kieffer [personal communication] (Figure 2.10), it seems that $\alpha = 2 \times 10^7 kg/m^2 s$ is right to an order-of-magnitude.

With $\mu = 8.6 \times 10^{-4} Pas$ for water and $A \sim 1m^2$ for Old Faithful, α determines the group

$$\frac{l}{na^4} = 5 \times 10^{10} m^{-3} \tag{2.18}$$

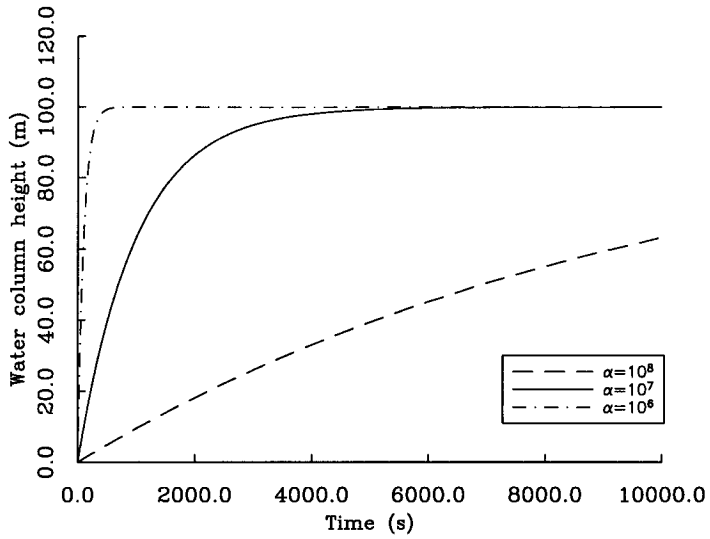

Figure 2.9: Filling rate based on the model of Figure 2.8.

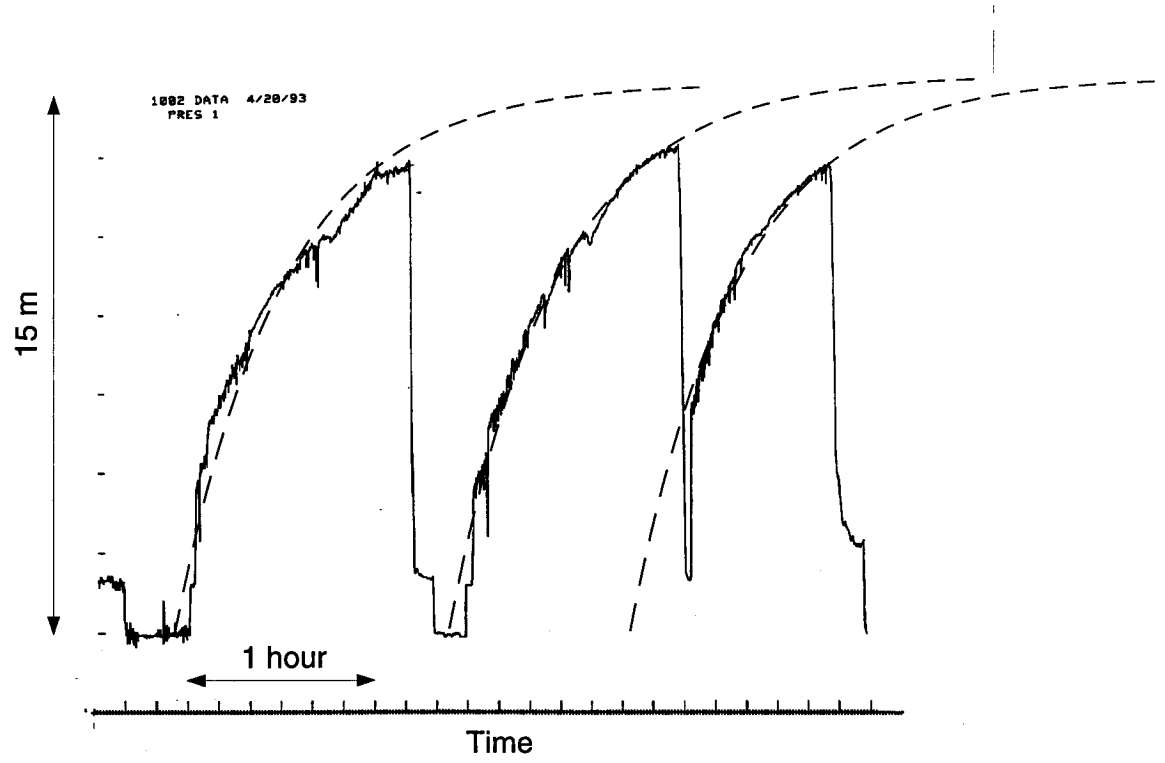

Figure 2.10: Pressure data (1 sps) obtained by Westphal, Kieffer and Hutchinson in 1993, and a filling curve (broken line) corresponding to $\alpha = 2 \times 10^{-7} kg/m^2$. The model described by Equation 2.17 obtains a good fit to the data.

or

$$\frac{l}{\kappa} \sim 10^{11} m^{-1} \tag{2.19}$$

The average velocity u_{av} is dependent on the water level change rate, $\dot{z}$, which can be estimated from the measurements. The water column rises about 20m in one hour; therefore, $\dot{z}$ is $\sim 5 \times 10^{-3}$m/s.

The Reynolds number for pipe flow is defined as

$$R_e = \frac{\rho u_{av} 2a}{\mu} \tag{2.20}$$

Therefore,

$$R_e = \alpha \frac{\rho \dot{z} a^3}{4\mu^2 l} \tag{2.21}$$

and in terms of the permeability

$$R_e = \frac{\rho \dot{z} a^3}{4\mu\kappa} \tag{2.22}$$

Using $\alpha = 2 \times 10^7 kg/m^2 s$, $\dot{z} = 5 \times 10^{-3} m/s$, the viscosity and density of water, $\kappa \sim 10^{-7} m^2$ for pervious gravel (*Turcotte and Schubert* [1982]), and pipe radius $a = 10^{-3} m$ gives $R_e \sim 10$. Similarly, from Equation 2.15 $l \sim 100m$.

Therefore, for Reynolds number as low as 10, $l >> a$, as expected.

2.2.3 Heating models

Heating from below

The temperature of the water as a function of time can be calculated by assuming a constant heat source. Thus the total of heat Q pumped into the water column at time t is:

$$Q = \int_{t_0}^{t} qA(\tau) d\tau \tag{2.23}$$

where q is the heat flux, and $A(t)$ is the surface area through which heat flows into the water column. The temperature is then calculated using the specific heat at constant pressure C_p.

$$\Delta h(t) = C_p \Delta T(t) = \frac{Q(t)}{M(t)} \tag{2.24}$$

where h is the enthalpy of the water, and $M(t)$ is the total mass in the column as a function of time, and for water $C_p = 4187 J/kg°K$.

Using a heat flux $q = 5 \times 10^6 J/m^2 s$ we get the heating history displayed in Figure 2.11. In this process the heat flows in through the bottom of the cylinder only. From equations 2.23 and 2.24 and from Figure 2.9, the temperature rise in the column will asymptotically become linear, as the

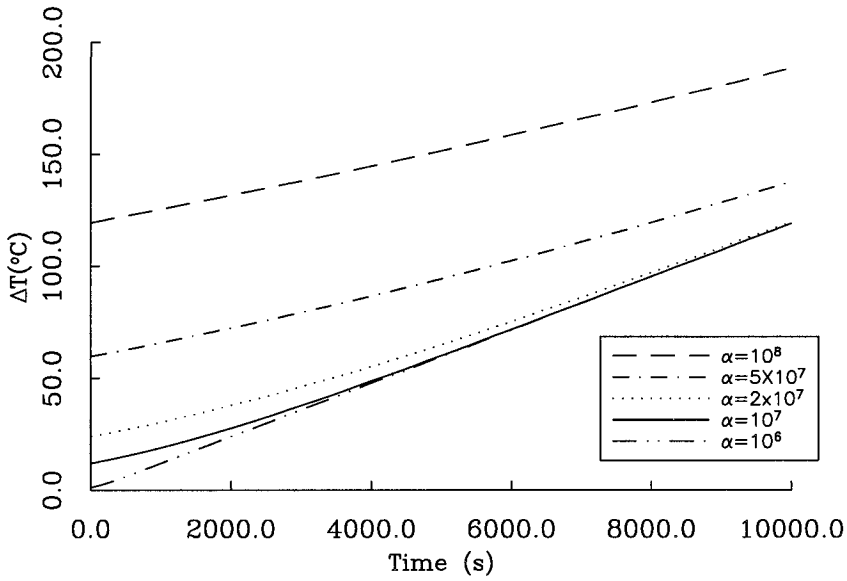

Figure 2.11: Heating from below.

water level approaches its hydrostatic equilibrium level

$$\Delta T = \frac{qt}{C_p \rho z(t)} \tag{2.25}$$

The slower the filling rate (higher α's), the larger the temperature rise per unit time. However, since for small α it reaches that level more rapidly, the curves for smaller α's become linear earlier. The initial conditions in all the calculations assume that there is no mass in the pipe at $t = 0$, and that the water flowing in is at $0°C$. The assumptions made initially infer that the heating of every unit mass is instantaneous, causing a temperature jump at time $t = t_0 + dt$. Therefore, the fluid temperature at infinitesimally short time after $t_0 = 0$ will differ significantly between processes of different heat and mass fluxes.

The value of the heat flux q is not well constrained. *Rinehart* [1980] calculated an order-of-magnitude heat flux for Old Faithful as follows: The temperature of the super-heated water at the beginning of an Old Faithful eruption is $112°C$ (the boiling point at Yellowstone is $93°C$). Since the origin of the water coming out of Old Faithful is meteoric, it enters the system at $\sim 5°C$. Therefore, the water needs to be heated from $5°C$ to $112°C$ between eruptions. The total amount of water ejected during one eruption is $50m^3$, which gives a total of $(112°C - 5°C) \times C_p \times 50,000kg \sim 2 \times 10^{10} J$ per eruption cycle. Since one cycle lasts approximately one hour, and the geyser's cross sectional area is $\sim 1m$, the heat flux is roughly $5 \times 10^6 J/m^2 s$. The assumption that the water heats from $5°C$ to $112°C$ during one cycle may be wrong since the water might very well be in the system already, and preheated to some temperature between the above limits. On the other hand, the system is losing heat by means other than an eruption via the numerous cooling-events.

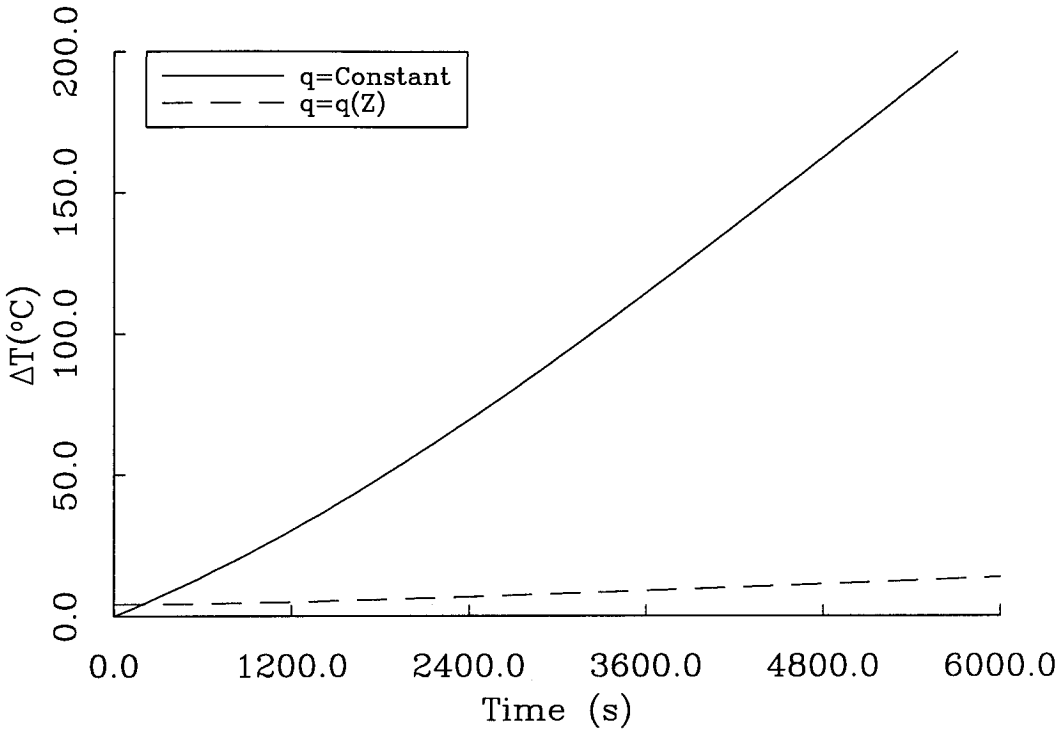

Figure 2.12: Heating from the walls. The solid line represents constant heating ($q = 5 \times 10^4 J/(m^2 s)$) while the broken line shows the heating history of a wall whose temperature increases linearly with depth ($q = 5 \times 10^5 J/(m^2 s); z_f = \frac{P_0}{\rho g}$).

Heating from the walls

Suppose that the heating is coming through the walls rather than from below. Consider two cases: One in which the heat flux is $q_0 = Constant$ and one in which it increases linearly with depth. In the first case the heating history is (equation 2.23):

$$Q(t) = \int_0^t q_0 c_w z(\tau) d\tau = \left(\frac{p_0}{\rho g}\right) t - \left(\frac{\alpha}{\rho g}\right) z(t) \tag{2.26}$$

where c_w is the circumference of the conduit, and $z(t)$ is given by Equation 2.17.

If we characterize the heat flux as linearly decreasing upwards:

$$q(z) = q_b \left(\frac{z_f - z(t)}{z_f}\right) \times Const. \tag{2.27}$$

where q_b is the heat flux at the bottom of the water column, then the heating history derived from equation 2.23 is

$$Q(t) = \left(\frac{q_b c_w}{2 z_f}\right) \left[z(t)t - \frac{z_f}{2}\left(\frac{\alpha}{\rho g}\right)\left(e^{-\frac{2\rho g}{\alpha}t} - 1\right)\right] \times Const. \tag{2.28}$$

where z_f is a reference depth.

Figure 2.12 compares the two cases described by equations 2.26 and 2.28. Again, as $z(t)$ asymptotically approaches z_f, in both cases the heating approaches linearity, as heat continues to flow into the system while the mass flow rate decreases.

2.2.4 Conduit geometry

The "heating from below" model results in a heating curve that is approximately linear in the time scale of $\sim 1hour$ in which we are interested. This implies that the rate of occurrence of heat-loss events which we assume to be proportional to the heating rate is also going to be linear. Since our observation is that there are at least two regimes of event rate (and probably more) the constant cross section pipe cannot explain the change in event rate. A possible model that can account for the observed rate change is that of a pipe with a (sudden) change of diameter. It has been observed that such a change does occur. According to *Birch and Kennedy* [1972] and Westphal et al. [personal communication], there is an area of widening at about the $10m$ depth from the top of the hole. The extent of that widening is not known. Let's assume that a pipe has a cross-section area A_0 that opens at some depth z_1 to a cross-section area $A_1 > A_0$. Since the water level rise $\dot{z}$ is slow, we can regard that time as a starting point for a new filling process of a pipe of cross section A_1, but now with a new initial condition $z(t=0) = z_1$ which results in a constant $C = z_1 \frac{\varrho g}{p_0} - 1$ in Equation 2.17. Therefore, the temperature is given by

$$\Delta T = \frac{1}{C_p} \frac{Q_0 + q_0 A_0 t}{m_0 + \rho A_1 (z - z_1)} \tag{2.29}$$

where Q_0 and m_0 are the heat and mass accumulated so far in the narrow (cross section A_0) pipe, respectively.

The result is shown in Figure 2.13 ($q_0 = 5 \times 10^5 J/(m^2 s)$) and the corresponding water level rise and cumulative mass are shown in Figure 2.14. As soon as the water level reaches the z_1 level, the total mass increases following the curves shown in Figure 2.14. As a result the rate of temperature rise or, equivalently, the cooling-event rate will go down. This effect can be understood if we consider the limiting case when at z_1 the pipe opens indefinitely, causing a constant mass flux. Since we assume constant heat flux, the mass of water will asymptotically approach constant temperature. This in turn will cause the cooling events to cease altogether.

Similarly, if the pipe narrows at the z_1 level, then the mass flux goes down and the heating rate increases (Figure 2.15).

Figure 2.16 illustrates the behavior of a pipe with a wide section in the middle. The actual temperature-time curve should appear as a 'saw-tooth' shaped curve where every time the temperature reaches the critical super-heat, it drops by an amount corresponding to one heat quantum released by one event, and heats again to the threshold level following the slope of the heating curve

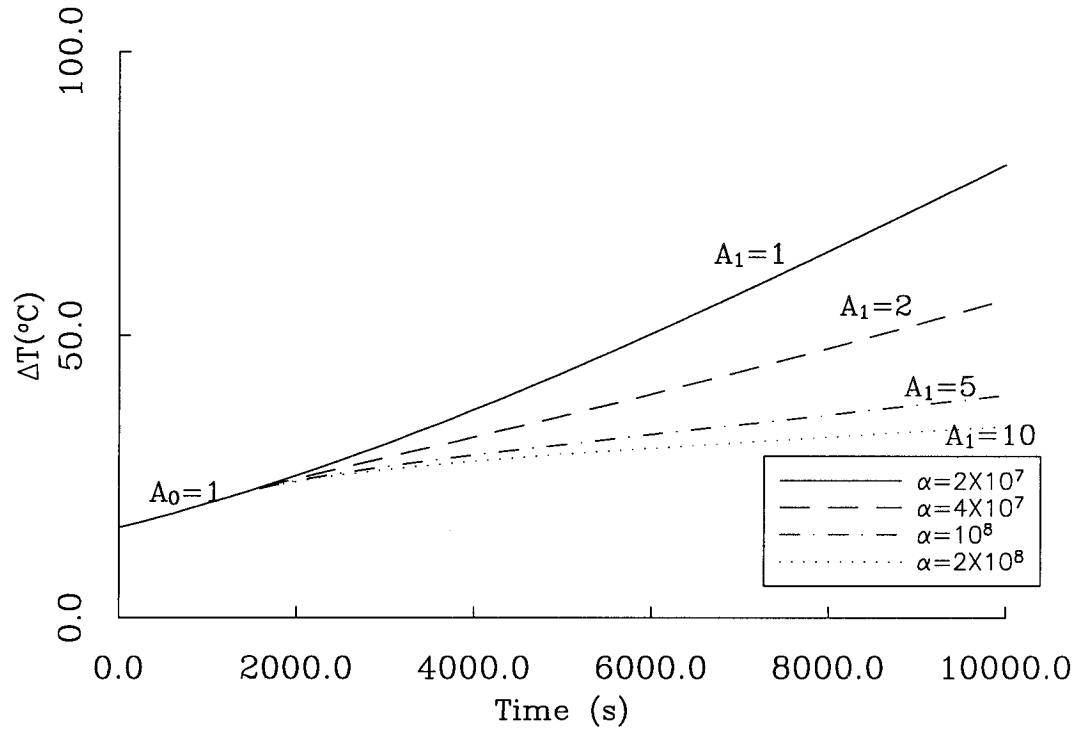

Figure 2.13: Heating from below with a widening pipe, $z_1 = 7m$.

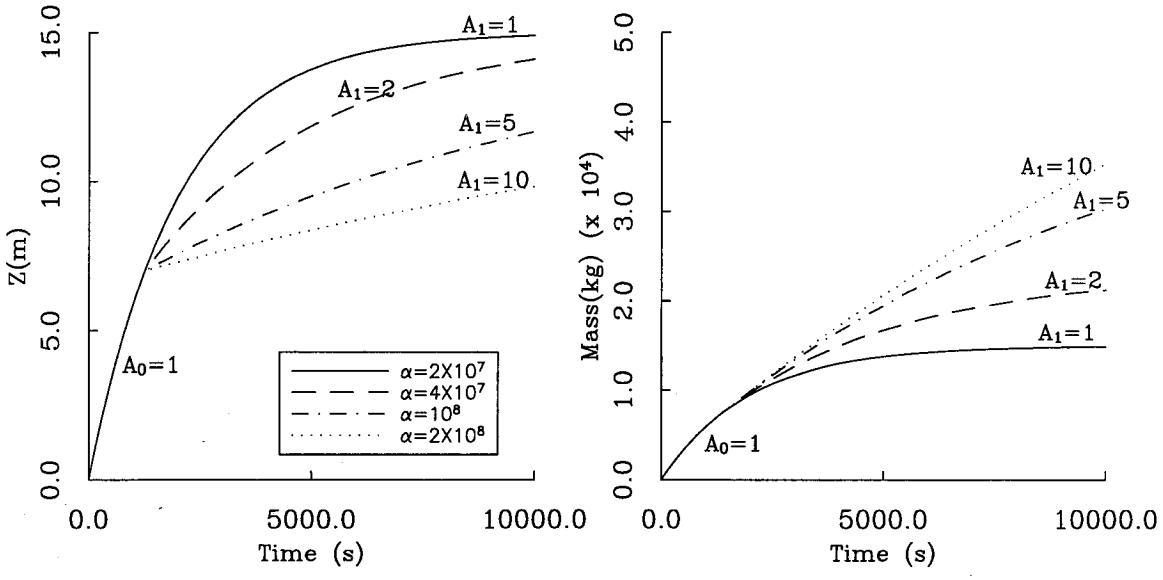

Figure 2.14: Filling rate of a widening pipe, $z_1 = 7m$.

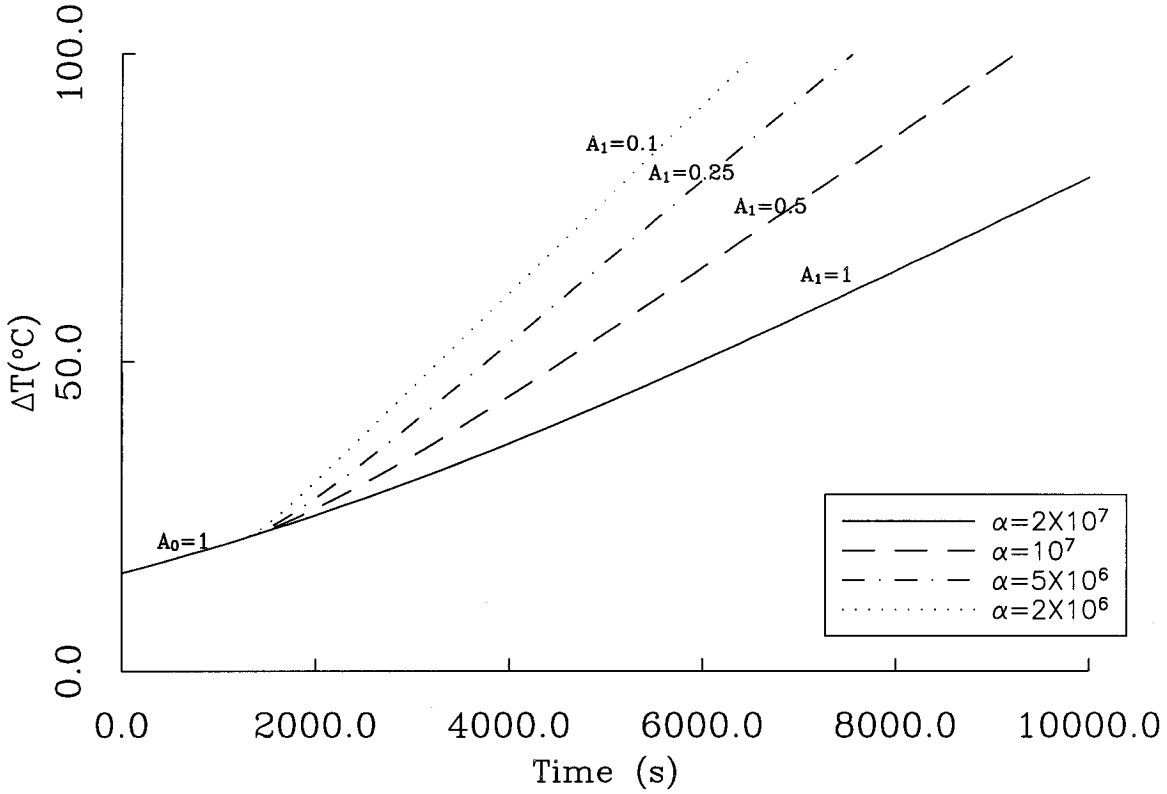

Figure 2.15: Heating from below with a narrowing pipe, $z_1 = 7m$.

at that instant. For convenience, Figure 2.16 displays the unperturbed temperature history rather than the actual 'saw-tooth' curve. It is interesting that the event rate drops dramatically for what seems like a mild change in the heating rate. This calculation illustrates the importance of the role played by the geometry of the pipe on the geysering behavior. Such changes as a decrease and a sharp increase of event-rate are observed at Old Faithful (Figure 2.7).

2.3 Summary

The source of continuous harmonic tremor at Old Faithful Geyser is most likely caused by individual bubble collapses, occurring at the top of the super-heated water column. The intensity of the tremor is determined by the rate at which bubbles collapse, which depends on the heat and mass flux, and is strongly controlled by the geometry of the conduit.

A collapse model with pressure difference $\Delta P = 0.3Bar$, residual internal gas pressure $P_{g_0} = 0.2Bar$, and an effective viscosity $\mu_E = 0.04m^2/s$ which implies a bubble radius, $R_0 \sim 5cm$, is in agreement with the pressure measurements and is consistent with the conduit diameter. Although at this point there is no damping mechanism which can fully account for the large effective viscosity needed to match the observation, the strong frequency dependent dissipation suggests a zone of

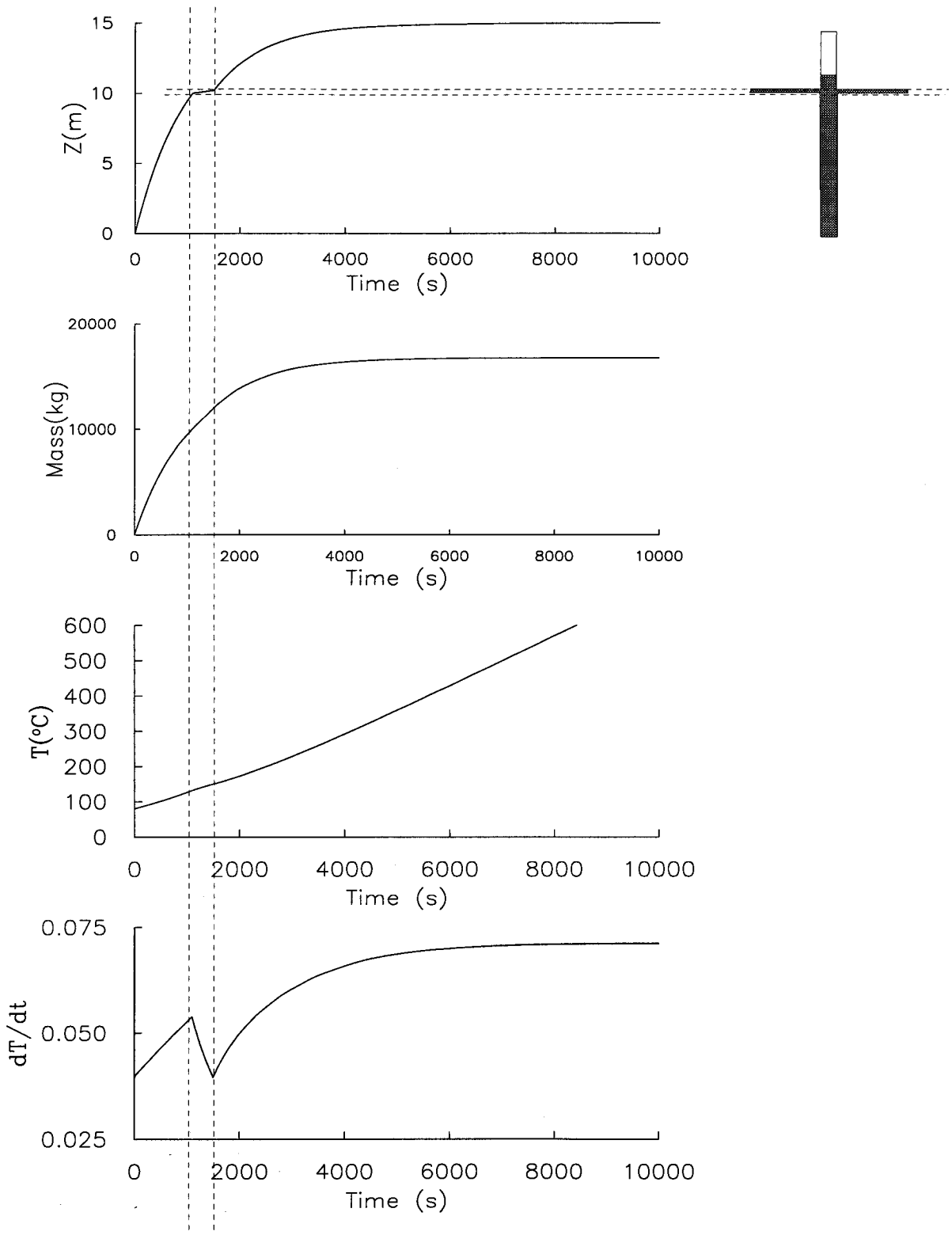

Figure 2.16: A pipe of cross sectional area $A_1 = 1m^2$ opening at $z_1 = 10m$ to $A_2 = 10^2$, and narrowing back to A_1 at $z_2 = 10.2m$. Shown in the figure are the water-column height, the cumulative mass, the heating history, and the derivative of the heating history which determines the rate of events.

bubbly liquid at the top of the water column, in which high frequencies are attenuated, and which does not affect longer periods.

!x A constant heat flux and a filling process driven by pressure equalization between the aquifer and the conduit through the porous medium gives rise to a heating rate which asymptotically approaches linear temperature increase as the water column exponentially nears its equilibrium level.

Neglecting dynamic effects, when the event rate is solely dependent on the heating rate, the time dependent event intensity can be modeled by widening and narrowing of the conduit, thus controlling the mass flux, and consequently the heat flux and the event rate.

Chapter 3 The Medium

Since it is well established now that the harmonic tremor observed at Old Faithful is not a result of a source process, we direct our attention at the elastic medium between the source and the receiver and ask the following question: How does the elastic medium respond to an impulse with a harmonic wave-train with the characteristics described previously, namely:

- The frequency of the harmonic signals varies as a function of location on a scale of $\sim 10m$.
- The harmonic signal is more pronounced in the horizontal components than the vertical component.
- The sledge hammer source produces spectral behavior similar to the natural source.
- The resonance frequency does not change with time.

3.1 Model: Shallow soft layer

The simplest possible model that can account for the above characteristics is that of a soft layer overlying a half space. By 'soft layer' we mean a layer whose shear (S) velocity is particularly low, as is normally observed in loose material and water-saturated soils (*Puzyrev and Kulikov* [1980], *Clark* [1966]), and as is common in the upper geyser basin of Yellowstone, (A more complete discussion of the local geology will follow later in this chapter.) When an elastic wave enters the layer at an angle from below the strong shear velocity impedance mismatch between the layer and its surroundings causes shear energy to be trapped in the layer, while compressional (P) energy propagating into it leaks out due to the milder P impedance mismatch between it and the half-space. This behavior is schematically illustrated in Figure 3.1.

Another consequence of the sharp velocity contrast is a strong P to SV conversion at the layer - half-space interface, and a near-vertical SV wave. Therefore, the SV motion will be observed mainly on the radial component of a seismic station on the surface, and its frequency is determined by the layer thickness.

Two main physical parameters may affect the above mechanism:

- The velocity and density structure
- The source frequency content

The role of these parameters will be discussed next.

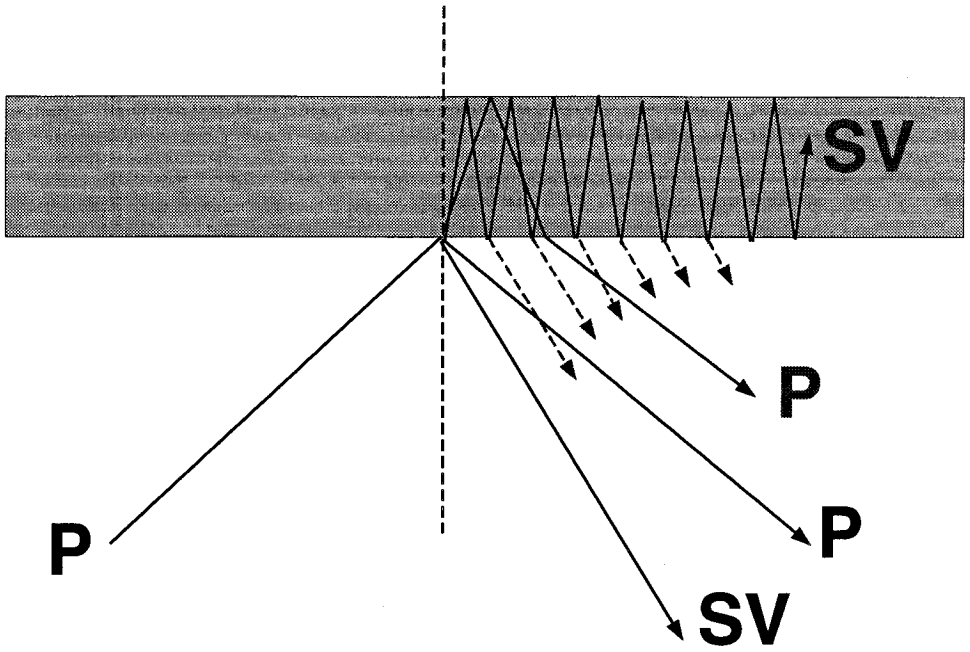

Figure 3.1: Plane P wave fed into a soft layer overlying a half-space.

3.1.1 Layer thickness and elastic velocity

In the following calculations synthetic seismograms are generated by feeding a plane wave at an angle from below into a structure consisting of a soft layer over half-space using Haskell's propagator matrix method (*Haskell* [1953]). The plane wave calculation does not include attenuation, and by definition is not geometrically spreading while propagating. This method is used for its simple elegance and for convenience. However, as will be demonstrated, since the reverberation occurs in a zone whose scale is $\sim 1-2$ wavelengths, the plane wave assumption is satisfactory.

Figure 3.2 illustrates the mechanism described above. As was mentioned previously, since the reverberating SV wave is nearly vertical and the layer has one free surface, its wavelength is approximately

$$\lambda = 4 \times h \tag{3.1}$$

where h is the layer thickness. Thus the resonance frequency is

$$f = \frac{\beta}{\lambda} = \frac{\beta}{4h} \tag{3.2}$$

where $\beta = V_s$ is the shear velocity. And for the structure of Figure 3.2, $\lambda = 2m$ and $f = 25Hz$. The next frequency multiple that satisfies the free surface condition will be the third multiple, $f = 75Hz$. Note that since the SV reverberation is not perfectly vertical, some of it is observed on the vertical component.

Figure 3.3 demonstrates the direct dependence of the reverberation frequency on the layer thick-

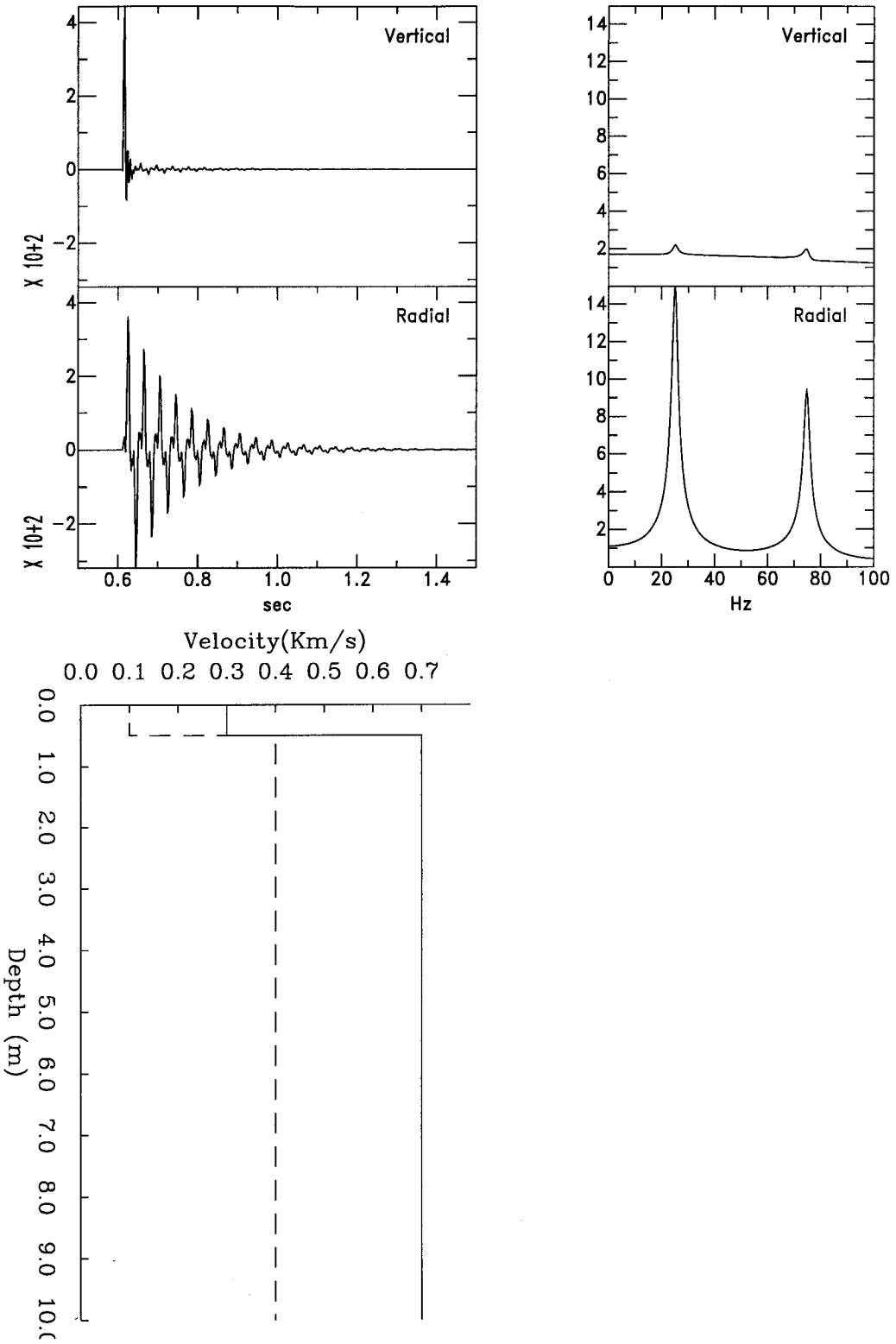

Figure 3.2: A synthetic seismogram and its Fourier spectrum generated using Haskell's propagator matrix method illustrate the response of a soft layer over a half-space to a P plane wave from below at an angle of 30 degrees. V_p and V_s variation in the structure are outlined by a solid and a broken line, respectively. The source time function is a 0.01s wide triangle.

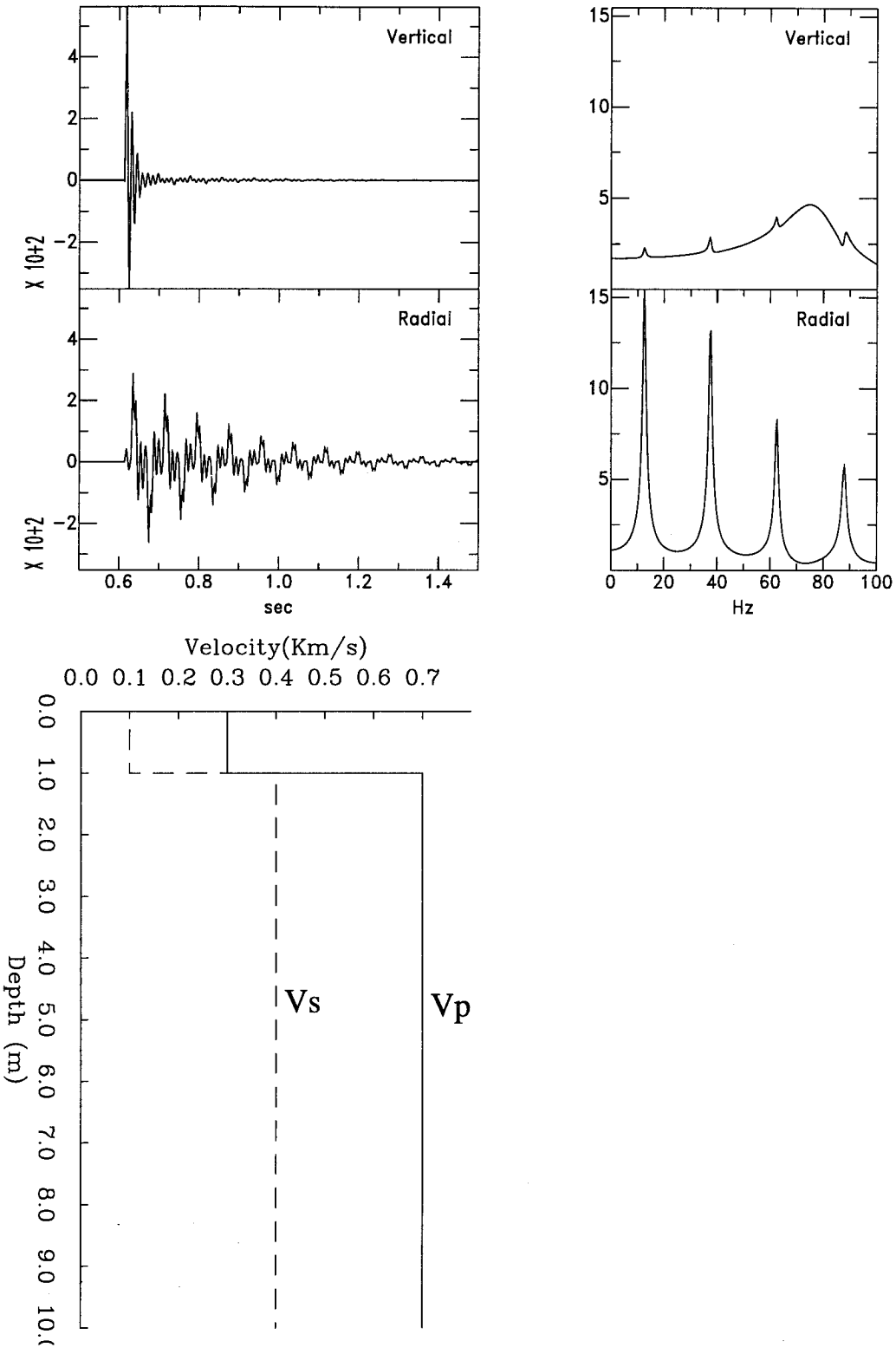

Figure 3.3: Same as Figure 3.2 with a soft layer twice as thick.

ness h. A factor of two increase in h causes the frequency to drop by half. Again, since there is only one free surface, only odd frequency multiples are observed. Some higher-frequency P reverberation is observed, but is attenuated quickly as P energy leaks out of the layer. In some cases this P reverberation may be well developed but outside the frequency response of the sensor.

When several layers are added between the soft top layer and the half-space (Figure 3.4), P waves leak out of the layer and reflect back, whereas the S energy is predominantly trapped in the soft layer. The P-wave reverberations off several layer interfaces result in a non-harmonic vertical motion at the surface.

The effect of a hard crust over a soft layer

In many locations around Old Faithful geyser as well as other geysers, the ground is covered by a thin crust of fine-grain geyser deposits. This material known as 'Geyserite' is composed of opaline silica and forms a hard surface overlying the softer material below. This formation is more abundant in proximity to the geyser's orifice.

The effect of this geological configuration on the resonance frequencies of reverberation can be understood by considering the simple model described in Figure 3.5. At the extreme case when $h_1 \sim \infty$, the frequency of the fundamental mode of oscillations in the layer would be double that of a single layer at the surface to accommodate non-slip conditions at the layer boundaries. However, when the crust is infinitesimally thin, there would still be a strong interaction between the soft-layer and the free surface.

Figure 3.6 illustrates the effect of the crust on the spectral behavior of the medium. The fundamental mode at $h_1 = 0$ is shifted to lower frequency with increasing crustal thickness, and would altogether disappear at the limit when $h_1 \sim \infty$. The second overtone makes the transition to a frequency twice as high as the original fundamental mode. The reason for this gradual behavior is that when the crust is thin, it moves as a rigid body on top of the soft layer. Thus, gradually increasing the thickness of the crust is equivalent to the gradual increase of a mass in a spring-mass system, which in turn reduces its natural frequency.

The significance of this effect is illustrated in Figure 3.7 where the reverberation frequency in a multi-layer structure is still dominated by the top $30cm$, and the presence of crust greatly affects the spectrum by reducing the fundamental mode frequency as described above. This process provides an additional mechanism to drastically change the reverberation frequency over a relatively short spatial scale, by variation of the crust thickness.

3.1.2 Source frequency content

The successful excitation of reverberations strongly depends on the frequency content of the source.

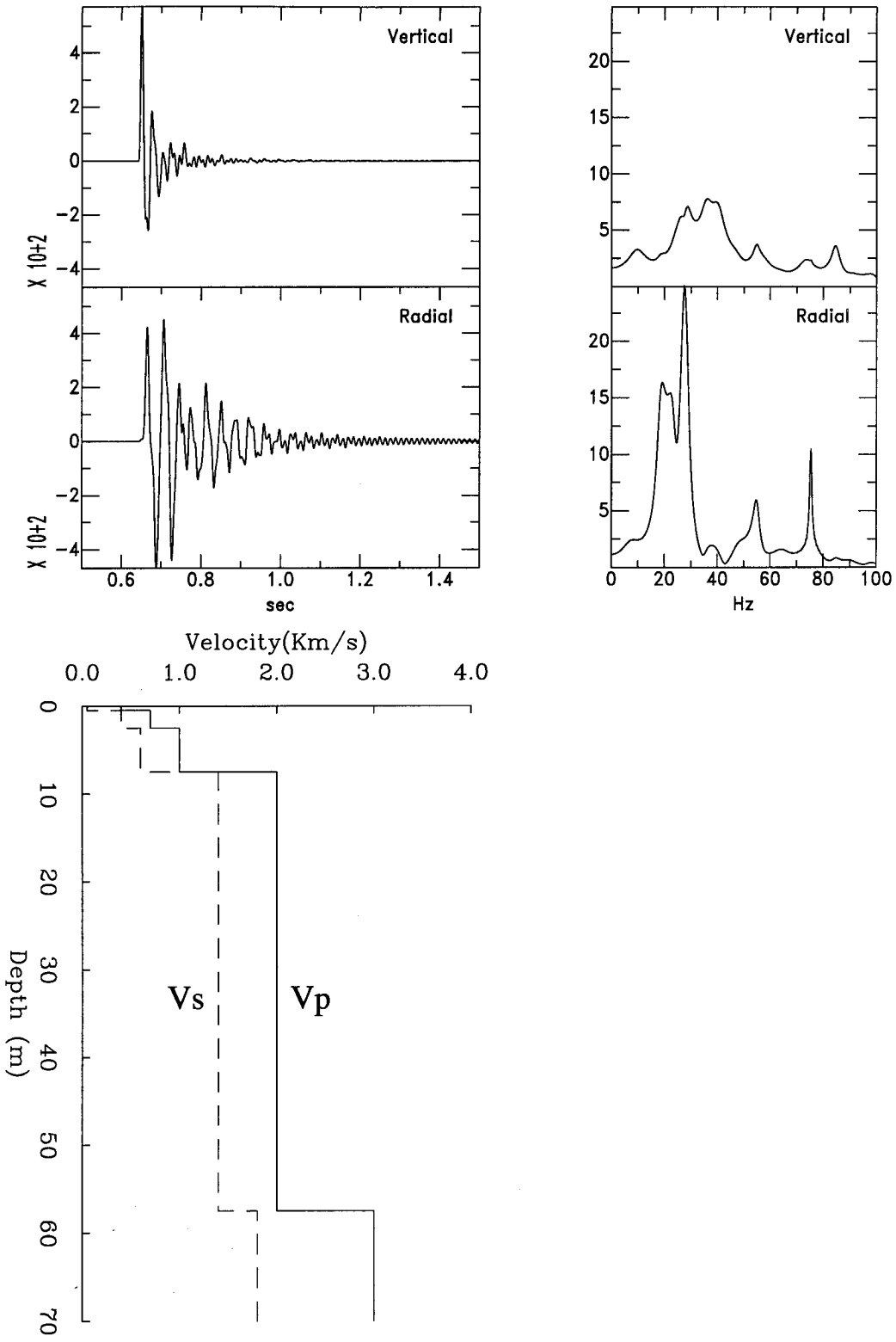

Figure 3.4: A stratified structure causes P-waves to bounce off the different interfaces. The soft layer on the top of the structure still results in near-harmonic reverberations.

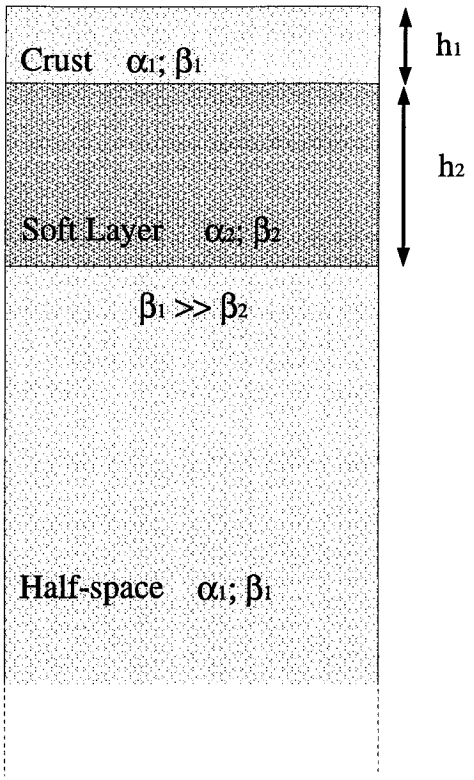

Figure 3.5: A crust of h_1 overlying a soft layer of thickness $h_2 \sim h_1$.

This dependence is illustrated in Figure 3.8. When the source time constant is much longer than the period of natural oscillation (case **a**), the excitation of the natural frequencies is poor, and improves as the source duration is getting shorter and closer to the fundamental mode frequency. The same effect may be important when considering the differences between earthquake signals and long period ('LP'-type) events on volcanos.

3.1.3 The geological structure

Geophone lines

In order to constrain the models described in the previous sections, five geophone lines were laid out at the locations shown in Figure 1.1. We attempted to locate individual reflectors in the medium if they existed, and for that purpose $100Hz$ vertical geophones were chosen. Each line consisted of 24 geophones placed at $1ft$ spacing for high resolution. The data logger was a 24-channel, 12-bit McSEIS-170f supplied by OYO Geospace, and was set up to record at 1000sps.

A sledge hammer source was used at five locations relative to each line as illustrated in Figure 3.9. Shots number 1 and 5 are one line length away (one 'walk-away'). As it turned out, no distinct reflections were observed. However, in some cases a surface wave ('Ground Roll') appeared, and was subsequently used to constrain the seismic velocity models described above.

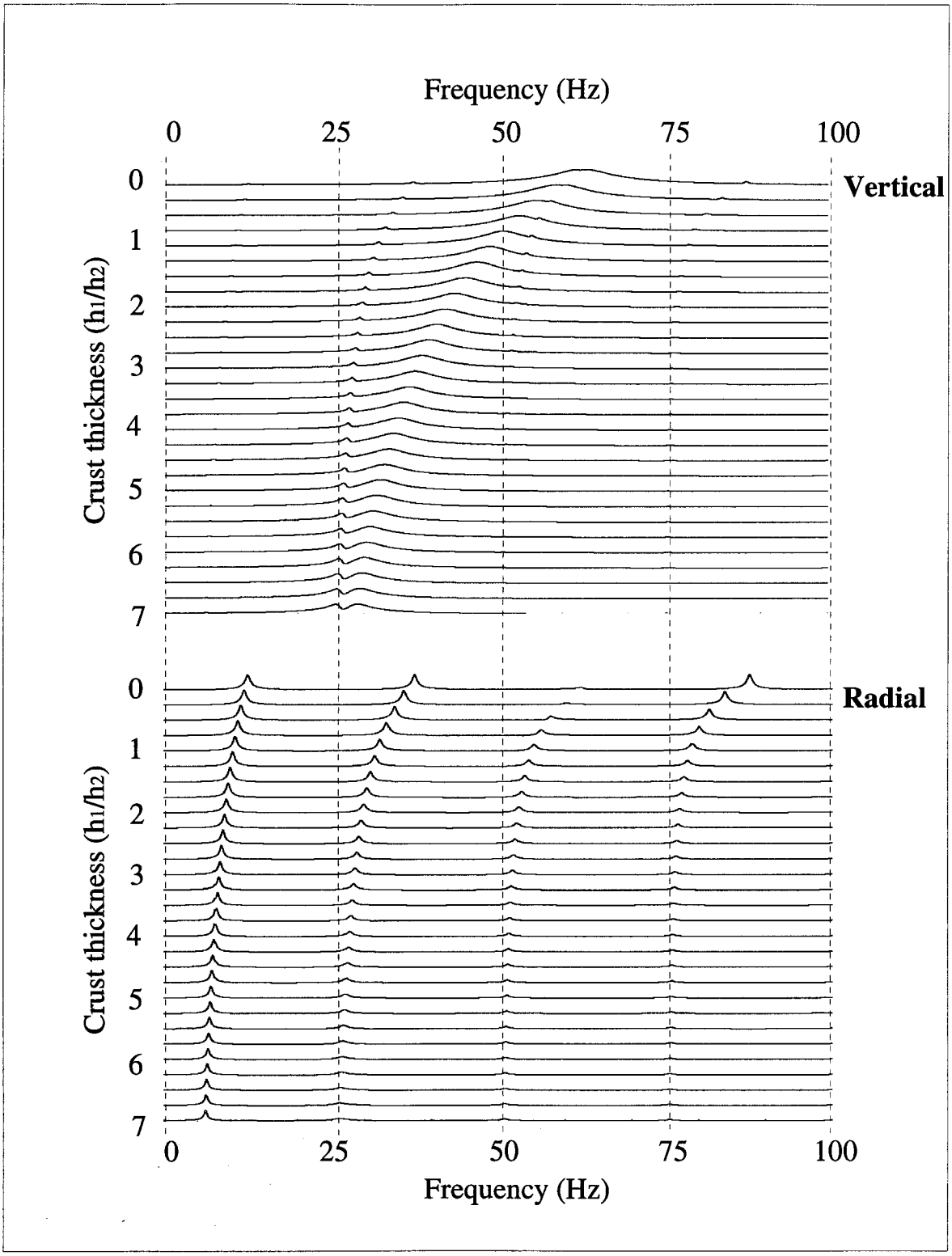

Figure 3.6: The spectrum of the radial and vertical components observed on the surface as a function of crust thickness. The starting velocity model is the same as in Figure 3.2 where the seismic velocity in the crust is the same as in the half-space.

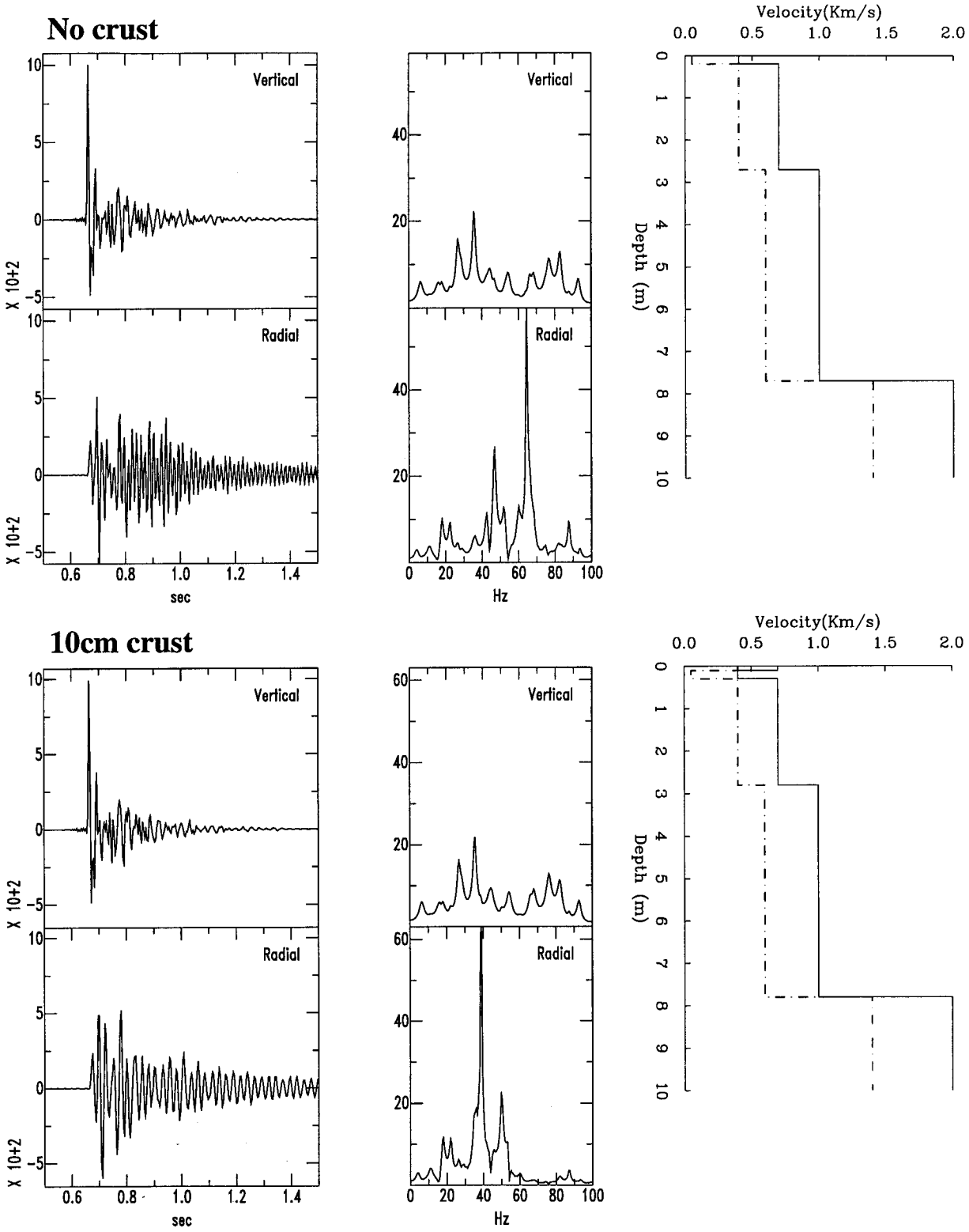

Figure 3.7: A comparison of the effect of a 10*cm* crust over a 20*cm* thick soft layer, overlying a multi-layered structure. The general behavior is as described above, and the presence of the crust causes the fundamental mode spectral peak to shift to lower frequency.

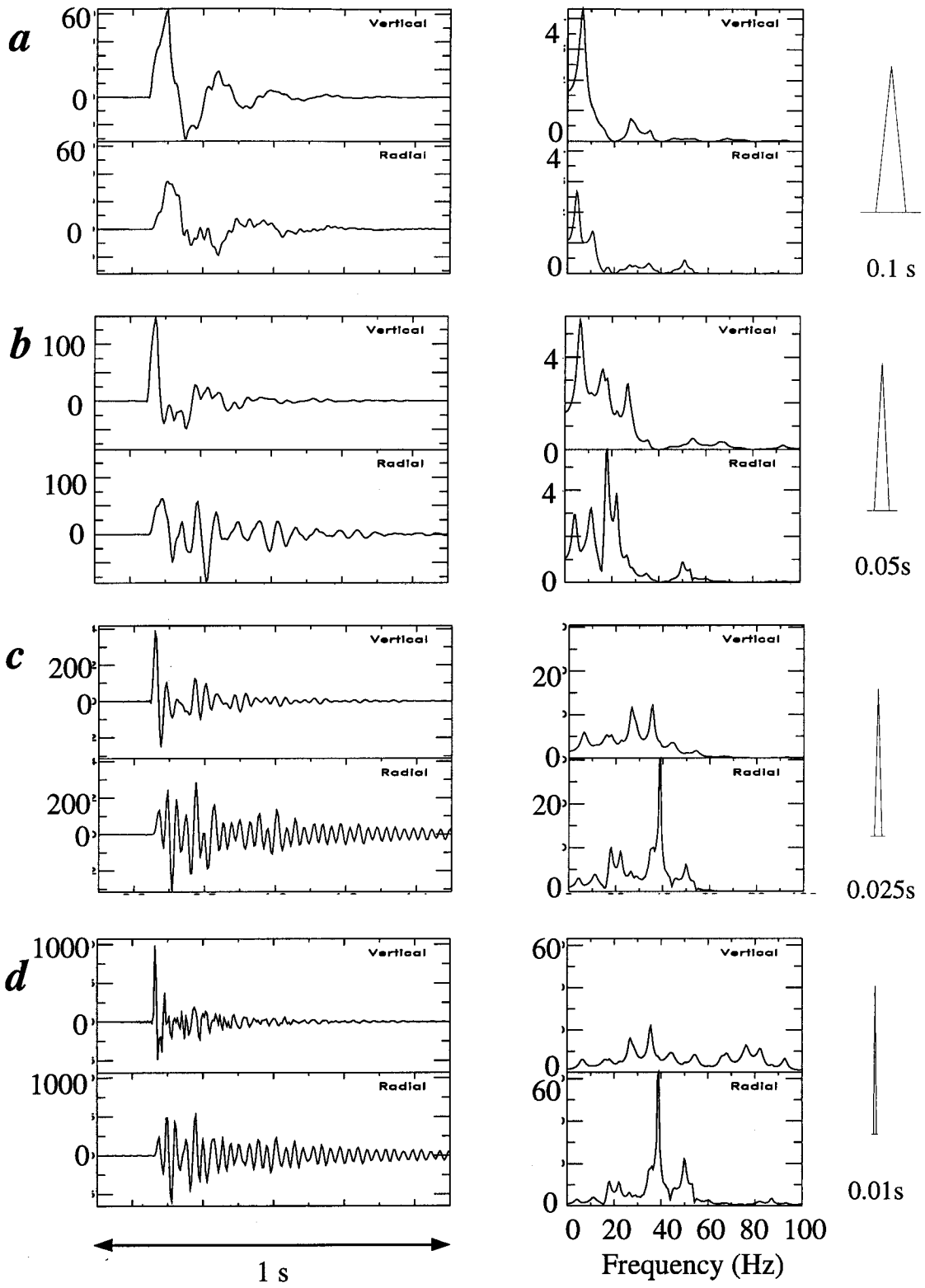

Figure 3.8: The dependence of excitation of the natural frequencies on the source duration (Frequency content). The elastic model used here is the same as at the bottom of Figure 3.7 and the source time history is presented to the right of each case studied. The amplitude is on a relative scale.

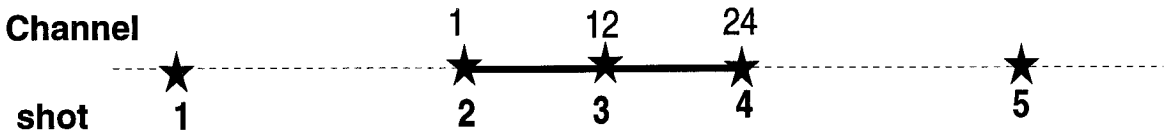

Figure 3.9: The general setup of a geophone line. Each line recorded five shots: two at one line-length away; two at the line ends and one at the center.

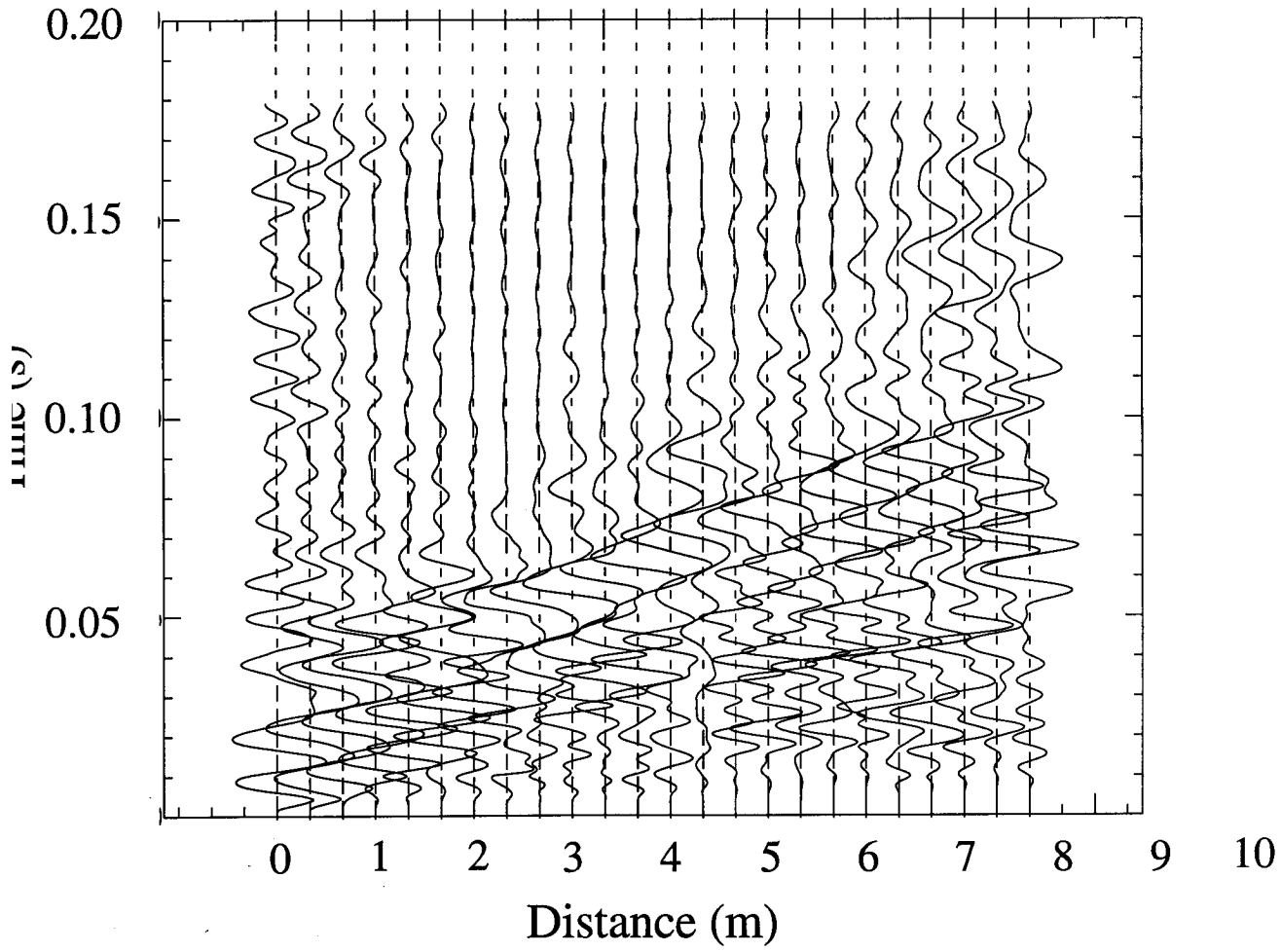

Figure 3.10: Seismic section at Line 1, shot number 2.

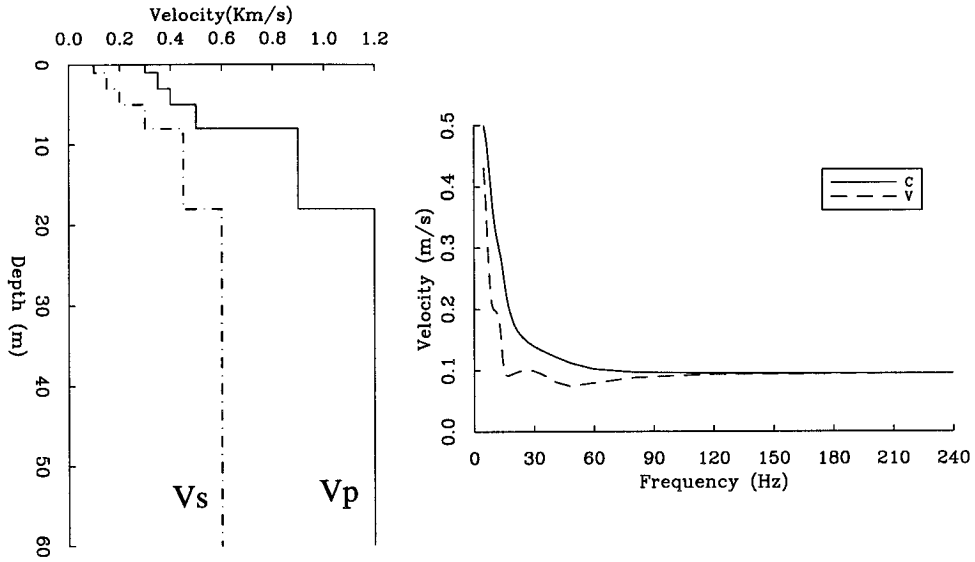

Figure 3.11: Velocity model and the corresponding Rayleigh group and phase velocity dispersion curves. At high frequencies the Rayleigh wave velocity is that of the slow layer on the top of the structure.

Figure 3.10 displays seismic section observed at line 1 (Figure 1.1). As is mentioned above, dominant feature on the section is the surface wave moving across the array at $\sim 200m/s$.

Similar behavior is observed at line 2 (Figure 3.12), where a distinct surface wave is propagating across the array at a slightly lower velocity. This behavior is consistent with the type of model suggested above for the local excitation of reverberations, as can be explained by the numerical simulation of a Rayleigh wave generated by a vertical force on the top of the structure displayed in Figure 3.11. The group and phase velocities at high frequencies are determined solely by the velocity of the shallow, soft layer. The velocity of propagation changes on a scale of a few meters between Line 1 and Line 2, which is also consistent with the suggested model.

Another model explains the observation at Line 4 (Figure 3.13). As for Line 2, the surface-wave velocity is determined by the soft layer on top. At line 4, high-frequency body waves are more prominent than in Line 2 or 1, yet a surface wave is still observed (Figure 3.14). Little dispersion is observed.

Line 4 was situated with the intention of comparing it to the observations at the nearby stations BD00A and BD00B (Figure 1.1). The structure suggested for line 4 and its corresponding calculated impulse response are consistent with the observations at these stations as illustrated in Figure 3.15.

Geology

A disadvantage of Old-Faithful was the fact that we were not allowed to trench the shallow structure once we had the notion that it is responsible for the seismic behavior as described above. The geology, therefore, had to be inferred from nearby structures, past excavations and drill-holes in the area,

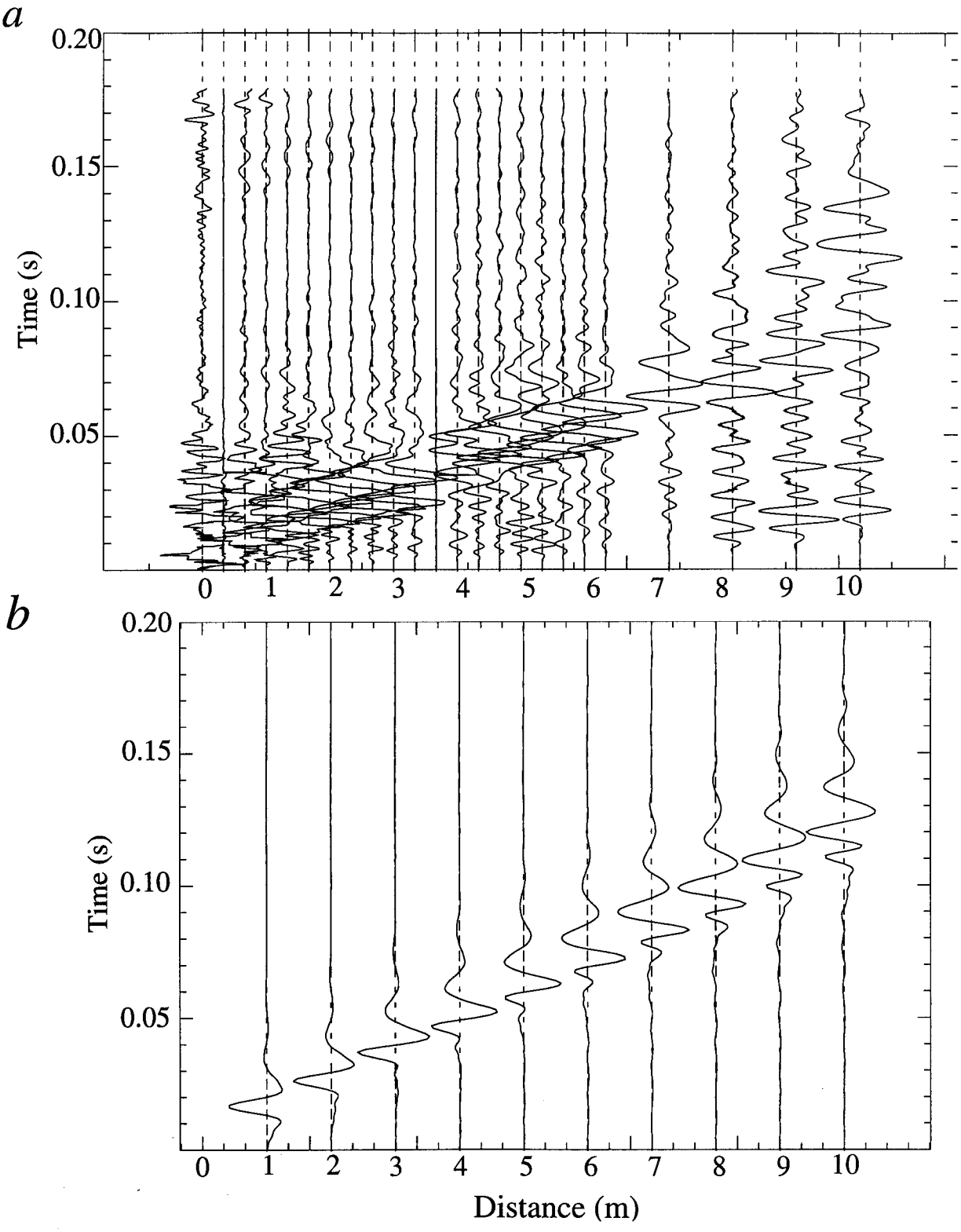

Figure 3.12: A combination of shots 2 and 5 at Line 2, and a calculation of the fundamental mode Rayleigh wave generated from a vertical single force using the model of Figure 3.11. The source is a $0.01s$ long triangle, which simulates the sledge-hammer.

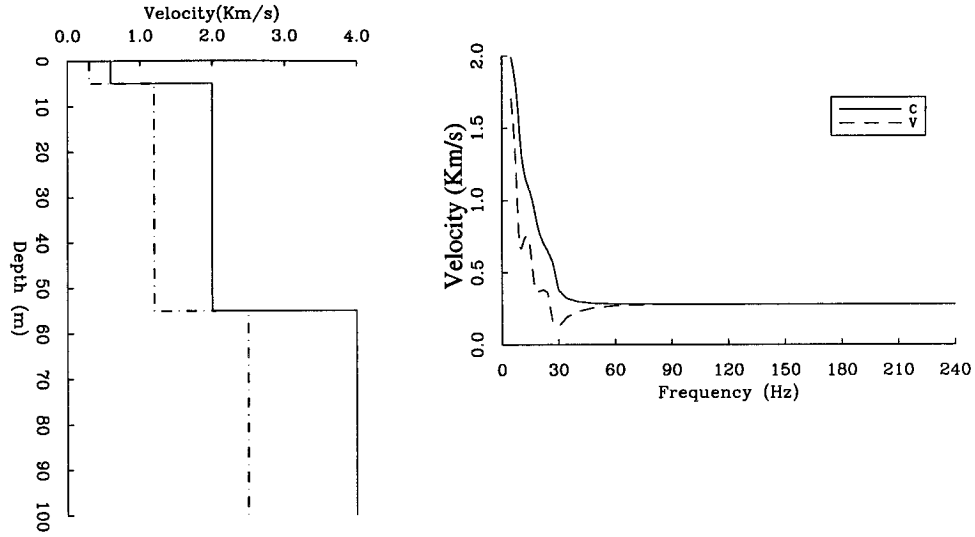

Figure 3.13: Suggested velocity structure for Line 4.

with the understanding that even though these data do not give an exact description of the in situ geology, they most likely display the general characteristics of the shallow subsurface at the Upper Geyser Basin in Yellowstone. The closest geologic structures resembling Old Faithful are the neighboring dormant geyser domes displayed in Figure 1.1. The dome southeast of Old Faithful is composed of layers upon layers of soft-material, made of small-grain, unconsolidated, porous and water-saturated material which can be bored by hand. The surface around Old Faithful itself is covered interchangeably by loose material and hard surface 'geyserite', an opaline slica geyser deposit, which covers most of Old Faithful's dome as well as patches of several meters in diameter around it. We did not perform a detailed geologic study of the neighboring domes.

Several geologic studies were carried out at the Upper Geyser Basin through the years. The first study was done by *Fenner* [1936] and consisted of a bore-hole several hundred meters from Old Faithful, in the vicinity of numerous hot pools. According to *Fenner* [1936]: "Study of exposures in the neighborhood indicated that all the surrounding area is under-lain by a series of roughly stratified gravels and sands." In a description of an excavation at a gravel pit north of the drill site Fenner states: "The material was an unconsolidated medium gravel with some larger pebbles and a few cobbles. It consisted almost entirely of obsidian and rhyolite, well stratified, but the strata were of wavy form and in places showed distinct cross-bedding." Fenner's descriptions are in full agreement with the type of structure derived from the seismic data. The 'wavy form strata' may be responsible for the spatial frequency fluctuations. Following Fenner, a group from the U.S. Geological Survey conducted a series of research drill holes in Yellowstone National Park (*White et al.* [1975]). The group headed by D. White and R. Fournier drilled four holes in the Upper Geyser Basin as well as several other basins in Yellowstone. I have gained access to their very detailed bore-hole data, and

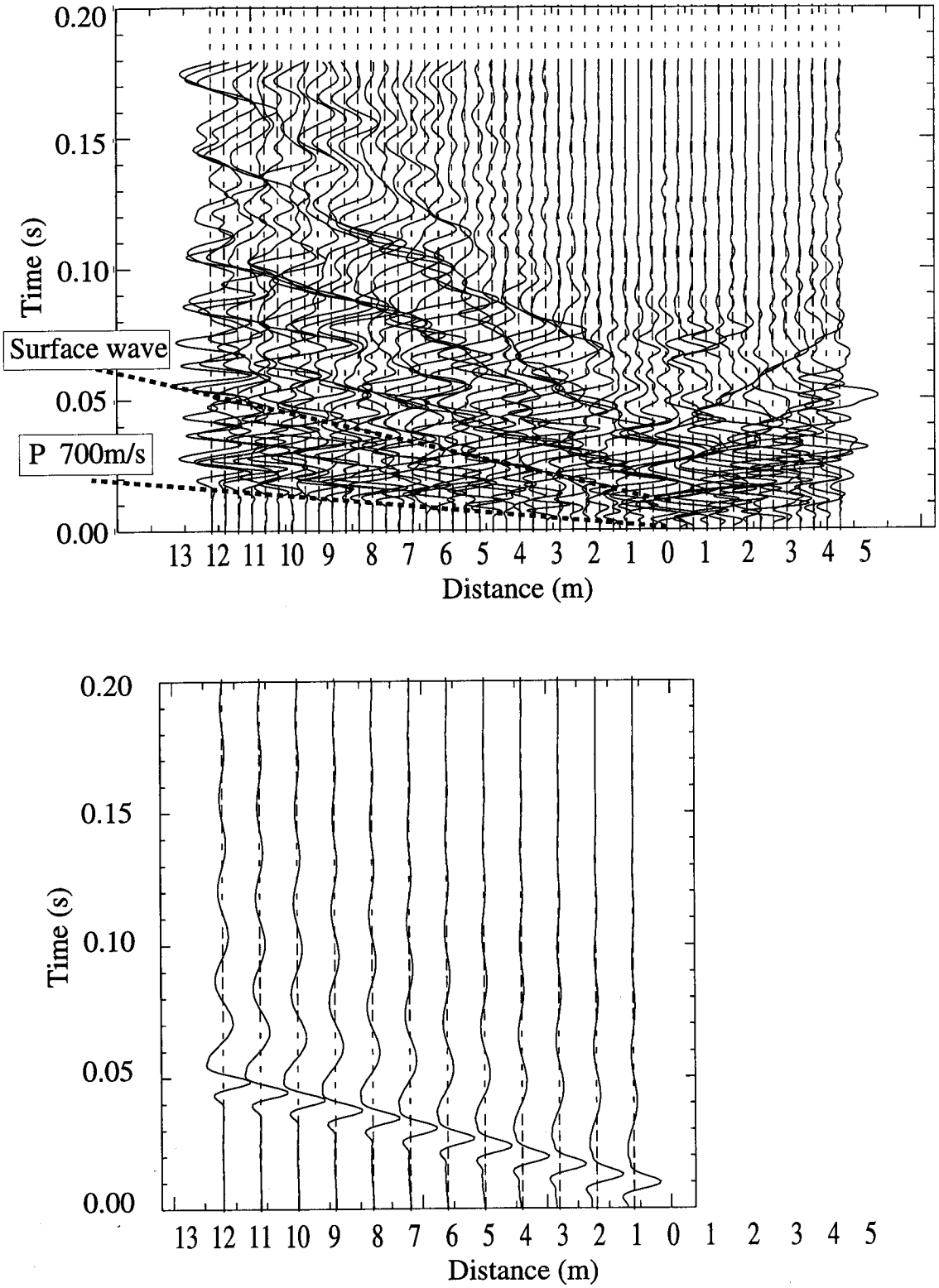

Figure 3.14: Line 4, shots 1 and 3.

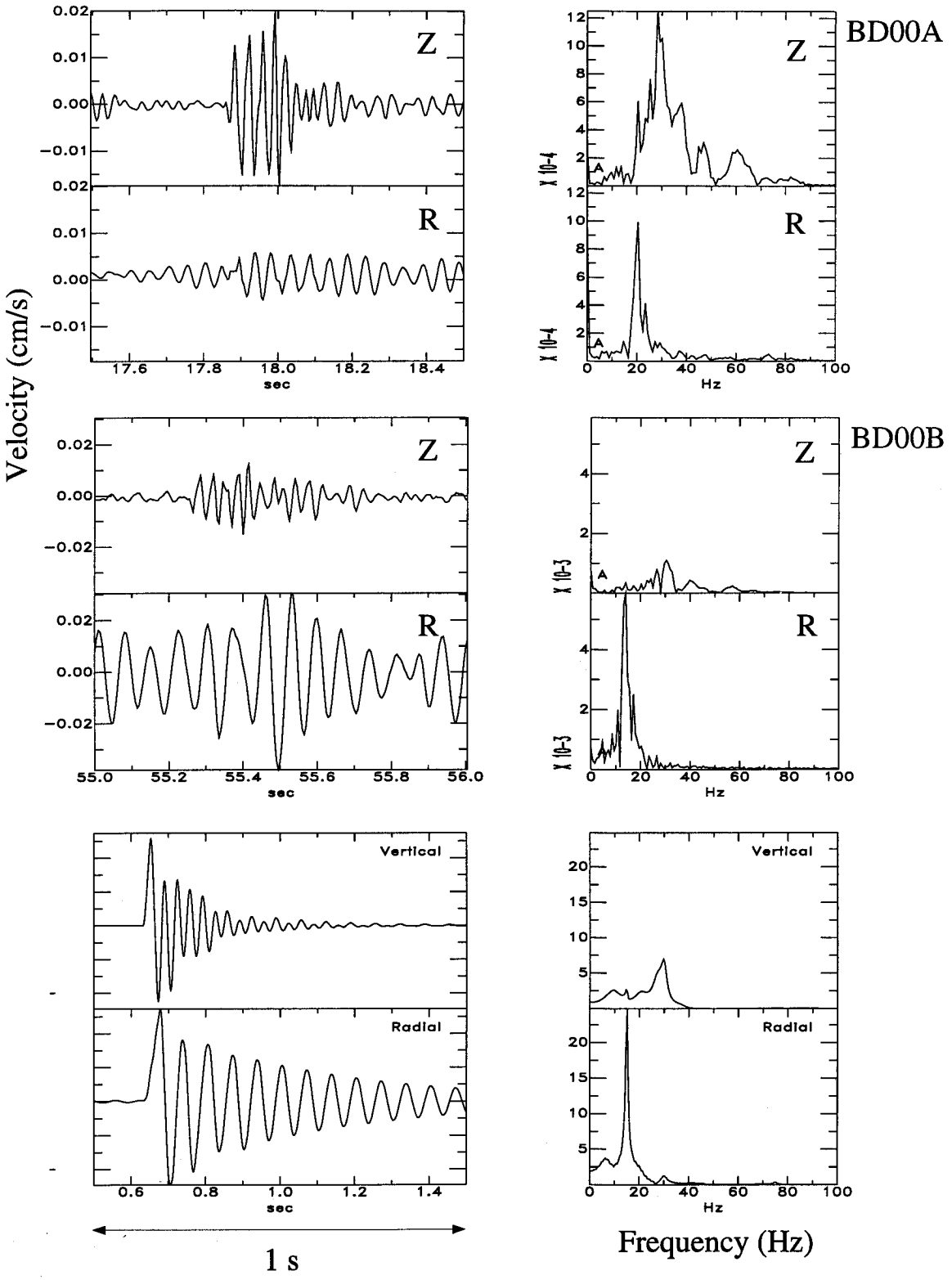

Figure 3.15: Using the data of Figure 3.14, a layer thickness is determined (Figure 3.13) to match the frequencies observed at nearby stations BD00A and BD00B. Source duration of 0.05s is used to simulate a bubble pulse.

with the authors' permission I report here some of the shallow drilling data unpublished previously.

Y1 - 1.2 Miles West of Old Faithful Geyser

Depth (ft)	Material
0 - 5.5	Fragmental sinter; Crumbly and poorly lithified. Opal; Black-brown coated partings. Conspicuous layering.
5.5 - (?)12	Indurated fragmental and primary Sinter. << 5% sporadic admixed volcanic gravels. Primary sinter has plant casts.
12(?) - 16	Obsidian-clast gravels to pebble gravel and indurated coarse grain sand. Poorly and sporadically lithified.
16 - 25.5	Granule gravel, locally pebbly. Obsidian and rhyolite detritus. Conspicuous cross-bedded to 30°.
25.5 - 30	Gravel; granule to pebble. Rude horizontal bedding (much missing core 27'-30'). Rare clast to 1'.
30 - 35.9	Silt and very fine sand; beds $1mm - 1cm$ (laminated). $\sim$ 25% interbedded gravel. Much broken core 34-35'. Bedding horizontal. Sand dikes in silt at 31'.
36- 40	Silt and very fine to medium sand with 20% inrerbedded granule gravel. Conspicuous cross-bedded in sand. Horizontal.
40 - 45	Gravel; granule to pebble-size; Interbedded coarse sand and trace fine sand. Cross bedded to 30°. Dip horizontal to 10°. Max clast $\sim 1cm$.

Y7 - Biscuit Basin

Depth (ft)	Material
0 - 1	Artificial fill.
1 - 3.5	Sinter (1-2' solid, 2-3.5' fragmental
3.5 - 5.5	Buff silica mudd, some sinter fragments. Grades downward into sandstone.
6 - 21	Cemented medium sandstone grading downwards into cemented granule obsidian sand + gravel. Some rhyolite cobbles up to 0.5' diameter. Sandstone shows crude bedding. Some graded cross-bedded cemented, clear amorphous silica? No alteration evident.
21 - 102	No core.

Both drill holes support the 'layer-over-half-space' model to some extent. In drill hole $Y1$, particularly the top 5.5 feet are 'poorly lithified', namely unconsolidated, while the material below is 'Indurated fragmental primary sinter', *i.e.*, consolidated.

3.2 Summary

The different seismic data sets, the broadband and short-period passive recordings and the active geophone line data together with our knowledge of the geology, point to reverberations of trapped SV (and in some cases P) energy in a shallow soft layer as the source of the harmonic impulse response of the medium. The sharp velocity contrast results in a near-vertical SV wave, which is observed on the station's radial component. The excitation is more efficient when the source duration is of the order of the medium's fundamental mode period.

The numerical simulations of the geophone line data suggest that at high frequencies ($\sim 100Hz$) the surface-wave velocity is approximately the shear velocity at the top layer. With this knowledge at hand and with the observation of the reverberation frequency at a specific site, a local layer thickness can be inferred. The variation in the reverberation frequency is dominated by the layer thickness, and possibly by the presence of a thin hard crust which reduces the fundamental mode frequency as it thickens.

Since the wavelength of the S waves ($\lambda = 4 \times h$) is small compared to the spacing between stations, only the local structure near the site of the observations controls the frequency. The 96-geophone array data also supports the hypothesis of local excitation, as specific sites are consistently excited regardless of the source location (Chapter 1).

The fact that the excitation is confined to specific locations around the geysers suggests that the excited sites have a 3-D configuration which is not accounted for in the calculations performed here. Contributing to this notion is the fact that strong tangential harmonic motion is observed. Since

the source is known to be volumetric, for tangential SH motion to take place, coupling between the SV and SH motions must occur, and for that to happen a deviation from the 2-D models described here has to be considered. Such coupling can take place when the P wave propagates through an interface whose intersection with the wave-plane is not horizontal. The geological description of 'wavy form strata' and 'cross-bedding at 30°' may be describing this effect.

The harmonic tremor excitation mechanism described in this chapter may have strong implications to excitation of harmonic tremor in volcanos, where inter-bedding of hard lava flows and soft ash flows is common. This possibility will be discussed in the following chapter.

Chapter 4 Implications to Volcanoes

4.1 General

As will be demonstrated in this chapter, the seismic phenomena observed at Old Faithful described so far strongly resemble the activity observed prior and during some volcanic eruptions. In the light of the observations at Old Faithful depicted in Chapters 1-3, and the phenomenological resemblance between the geyser and volcano seismicity, this chapter will address the possible implications the Old Faithful experiment might have for the understanding of sources of volcanic seismic signals, as well as the important question of their power as a predictive tool. Since the term 'volcanic tremor' has been generally used to describe any non-earthquake volcanic seismic activity, it would be useful to take a closer look at some specific examples of volcano-seismic activity. A brief review of several representative observations will follow. Special attention will be paid to similarities and differences on an eruption cycle time-scale as well as individual events scale.

4.2 Volcanic tremor examples

The question of the source physics has been addressed by numerous studies. Although some studies point to a strong path effect dominating the frequency content of the signal (*Goldstein and Chouet* [1994], *Gordeev* [1992], *McNutt* [1986], *Weaver and Malone* [1976]), it is generally agreed that the harmonic nature of tremor originates in source resonance. Most proposed models for harmonic volcanic tremor concentrate on the signal's spectral characteristics and successfully match the observed spectral peaks. These models span a large range of physical processes, such as resonating 'organ pipe'-type oscillations (*Chouet* [1985]), oscillating crack (*Aki et al.* [1977]), non-linear excitation by fluid flow (musical wind instruments, *Julian* [1994]) and more. However, all these plausible models stem from the notion that it is indeed the source which oscillates harmonically. This assumption is based on the general following observations:

- Different stations observe common spectral peaks.
- Simultaneous spectral changes at different sites.
- Spectral correlation with other observations (mainly audio-visual).

4.2.1 Langila, Papua New Guinea and Sakurajima, Japan

The eruptions of Langila and Sakurajima provide two of the most obvious examples of harmonic tremor generated by source, to which Old Faithful is a poor analogy. At Langila *Mori et al.* [1989] describe two main types of tremor: harmonic, and non-harmonic as shown in Figure 4.1*a* (*Mori et al.* [1989]).

The continuous non-harmonic tremor seems to be composed of a string of low-frequency (LP) events, as is observed at Old Faithful. The harmonic tremor, however, displays two distinct frequencies (a fundamental mode and its multiple) appearing identically at three different stations. There are no phase shifts in the harmonic signal as would be the case if it were generated by a random excitations of 'LP' events, and as is the case for the 'non-harmonic' tremor. It was also reported (*Mori et al.* [1989]) that on occasion the volcano produces puffing sounds at a frequency matching the recorded harmonic oscillations.

Similar seismic observations were recorded at Sakurajima (Figure 4.1*b*, (*Julian* [1994], after *Kamo et al.* [1977]). Distinct spectral peaks and their multiples are observed on all three components, and at different sites (not in the figure). Again, the signal displays no phase shifts after the oscillations become steady.

The examples of Langila and Sakurajima are the end member of volcanic tremor generated by a pure source effect, and present the necessary observations required for a source related interpretation. Particularly, the Langila case illustrates the difference between a source effect and a path effect. The low-frequency ('LP') events described in Figure 4.1*a* are generated by an explosion process (*Mori et al.* [1989]) and are frequently accompanied by an air-wave. Their 'non-harmonic' characteristic is clear when compared to the harmonic signal generated by the source, and they probably represent the medium's impulse response just as in the case of Old Faithful. As will be described in some of the following examples, the characterization of tremor as 'harmonic' is highly subjective, to the extent that the Langila 'non-harmonic' tremor may be categorized as 'harmonic tremor' under different circumstances.

4.2.2 Kilauea, Hawaii

Types of tremor observed in Hawaii

Hawaiian volcanism presents one of the most diverse set of observation of fluid flow related seismicity. As was described by *Koyanagi et al.* [1987] in addition to brittle failure events (earthquakes), tremor and 'LP' events originate in three depths: Shallow ($>$ 5km), intermediate (5 – 15km) and deep (30 – 60km). While shallow tremor is directly related to observed eruptive activity, inflation and deflation, deep tremor acts steadily without direct relation to surface eruptions (*Aki and Koyanagi*

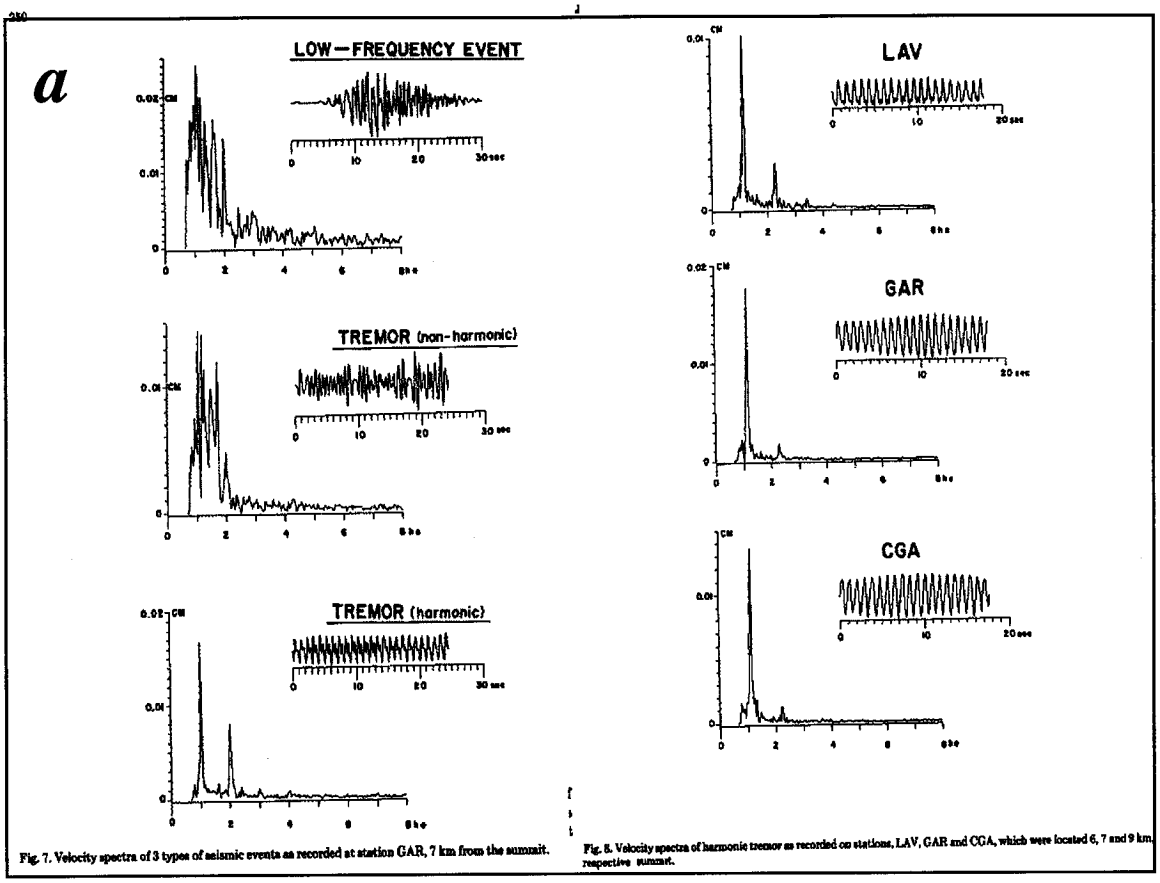

Fig. 7. Velocity spectra of 3 types of seismic events as recorded at station GAR, 7 km from the summit.

Fig. 8. Velocity spectra of harmonic tremor as recorded on stations, LAV, GAR and CGA, which were located 6, 7 and 9 km, respective summit.

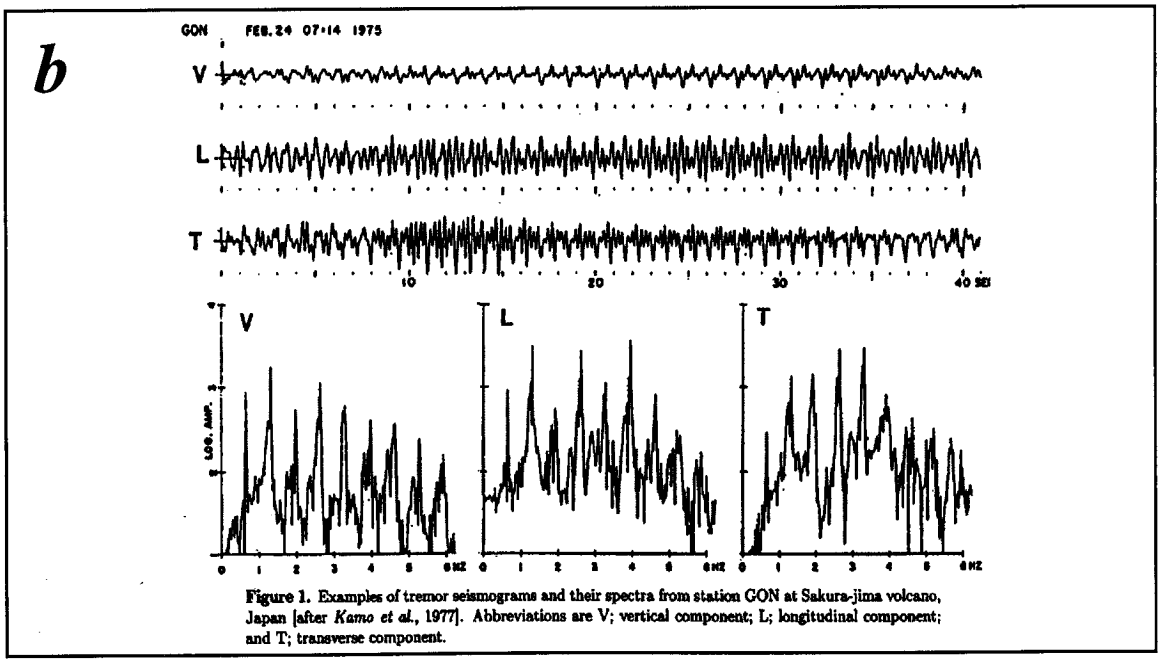

Figure 1. Examples of tremor seismograms and their spectra from station GON at Sakura-jima volcano, Japan [after *Kamo et al.*, 1977]. Abbreviations are V; vertical component; L; longitudinal component; and T; transverse component.

Figure 4.1: a. Non-harmonic, and harmonic tremor at Langila.; b. Harmonic tremor at Sakurajima.

[1981]). *Aki and Koyanagi* [1981] have observed that seismic stations at different locations observe a consistent change of frequency throughout episodes of deep tremor, which points to a source effect.

Intermediate tremor is generally associated with inflation of the volcano's summit, and is usually not directly related to observed surface activity. An a-seismic region is believed to exist between the deep and intermediate regions. Some of the typical Hawaiian activity is described in Figure 4.2 (*Koyanagi et al.* [1987]).

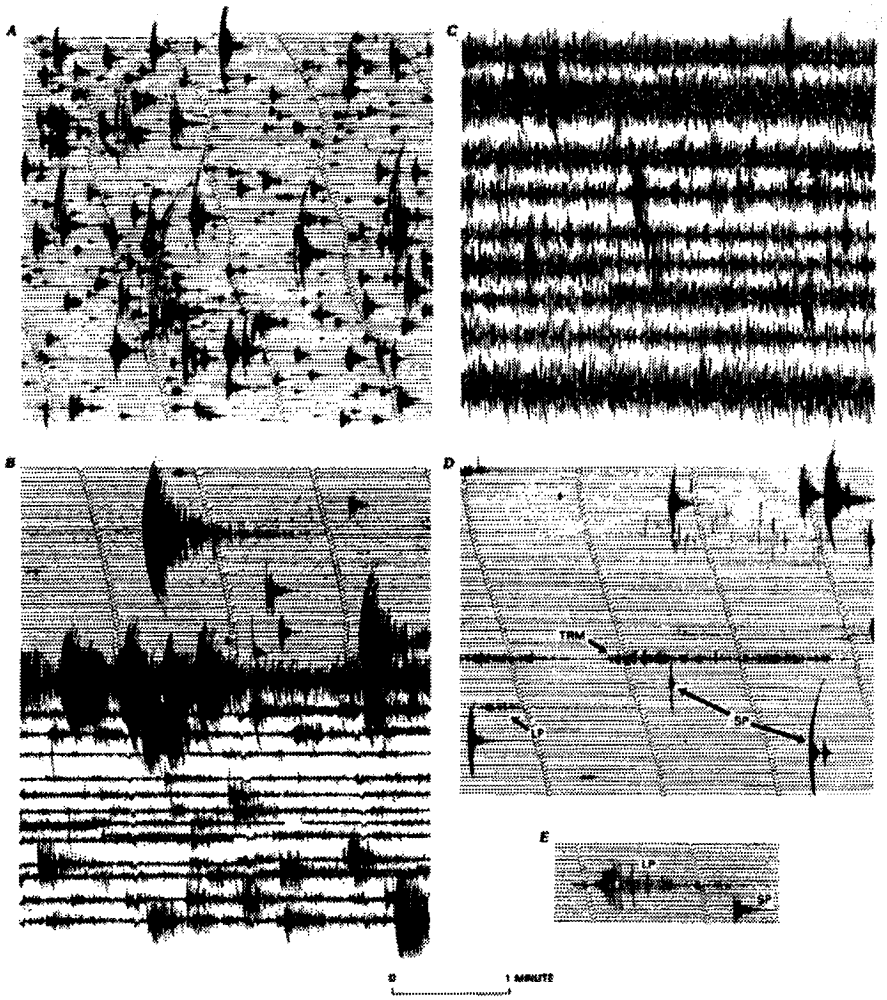

FIGURE 45.3.—Smoked-drum seismograms showing records of earthquakes and volcanic tremor in south Hawaii. *A*, Swarms of short-period earthquakes. *B*, Intrusion-related swarms of short-period earthquakes followed by eruption tremor (lower part). *C*, Continuous harmonic tremor during sustained eruption. *D*, Short-period earthquakes (SP), long-period event (LP), and intermediate-depth tremor burst (TRM). *E*, Signatures of a long-period event (LP) and a smaller short-period earthquake (SP).

Figure 4.2: Examples of Hawaiian tremor.

Shallow tremor

Shallow tremor, on the other hand, goes hand in hand with eruptive activity, as is demonstrated in Figure 4.3.

Hawaiian eruptions are composed of episodes of inflation, lava fountaining, and deflation, all associated in one way or another with shallow tremor and 'LP' events. The connection between shallow activity and eruptions may suggest that it might be analogous in some way to Old Faithful's activity in its intensity pattern as well as in individual events. An example of a tremor sequence that bears a resemblance to an eruption cycle at Old Faithful is presented in Figure 4.4, where amplitude as well as event rates combine to form a pattern similar to that observed at Old Faithful.

As is shown in Figure 4.4, the tremor and 'LP' activity is associated with inflation of the Southwest Rift of Kilauea, although no eruption is observed on the surface.

As far as the spectral characteristics of the tremor and the 'LP' events which compose it, shallow tremor displays distinct spectral peaks as was observed near Mauna Ulu (*Koyanagi et al.* [1987]) and Puu Oo (*Goldstein and Chouet* [1994]). It has been demonstrated (*Ferrazzini et al.* [1991], *Goldstein and Chouet* [1994]) that the shallow tremor near Puu Oo is strongly affected by the shallow structure. *Goldstein and Chouet* [1994] have suggested a model similar to that described in Chapter 3 for Old Faithful, of a near-surface soft layer that may be responsible for obscuring source from path effects.

4.2.3 Mountt Saint Helens

The eruption of Mt. Saint Helens, Washington, on May 18, 1980, and the following sequences of eruptions where preceded and accompanied by several types of seismic events (*Malone et al.* [1981], *Malone et al.* [1983], Figure 4.5*a*). Although the main eruption started with little immediate warning as far as tremor is concerned, as it was triggered by a massive landslide which gave rise to a lateral blast releasing the pressurized gases within the volcano, several of the sizeable eruptions in the following year displayed significant correlation between the activity on the surface and tremor (Figure 4.5*b*, *Malone et al.* [1983]).

The activity in the last hour/days preceding the eruptions illustrated in Figure 4.5*b*, are composed mainly of type-m transitioning to type-l earthquakes (Figure 4.5*a*). Harmonic tremor prior to the June 12, 1980, eruption is reported to have picked up in intensity and amplitude for a period of about 40min, but has died down $\sim$ 2 hours before the eruption, similar to Old Faithful's activity pattern.

As far as individual events are concerned, it is established yet again that the spectral characteris-

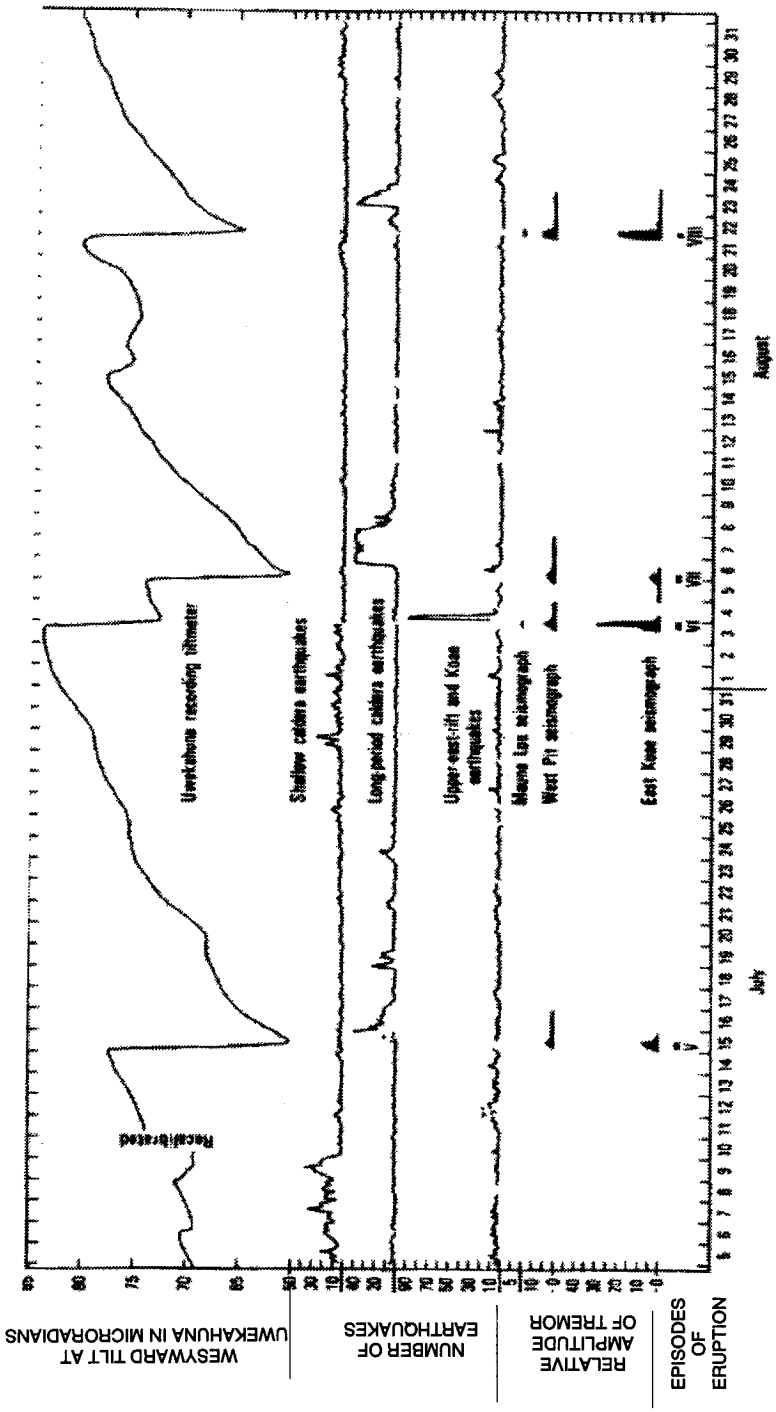

Figure 4.3: Plot of summit tilt, numbers of shallow earthquakes, relative amplitude of tremor, and episodes of eruption for the Mauna Ulu eruption of Kilauea Volcano, May-October 1969. Tilt measurements at 2-hour intervals from the Uwekahuna east-west component tiltmeter near the northwest rim of Kilauea caldera. Earthquake counts at 2-hour intervals from selected local stations, detection threshold estimated at about magnitude 0.1 Amplitude of tremor taken from adjusted hourly readings of smoked-paper records and plotted in relative units above background noise at three stations: Mauna Loa (MLO), 25 km from the eruption site; West Pit (WPT) 11 km from the eruption site; and East Koae (EKO), 5 km from the eruption site. Times of major eruptive episodes indicated by horizontal bars and labeled with their sequence numbers. Data beyond October incomplete and therefore omitted.

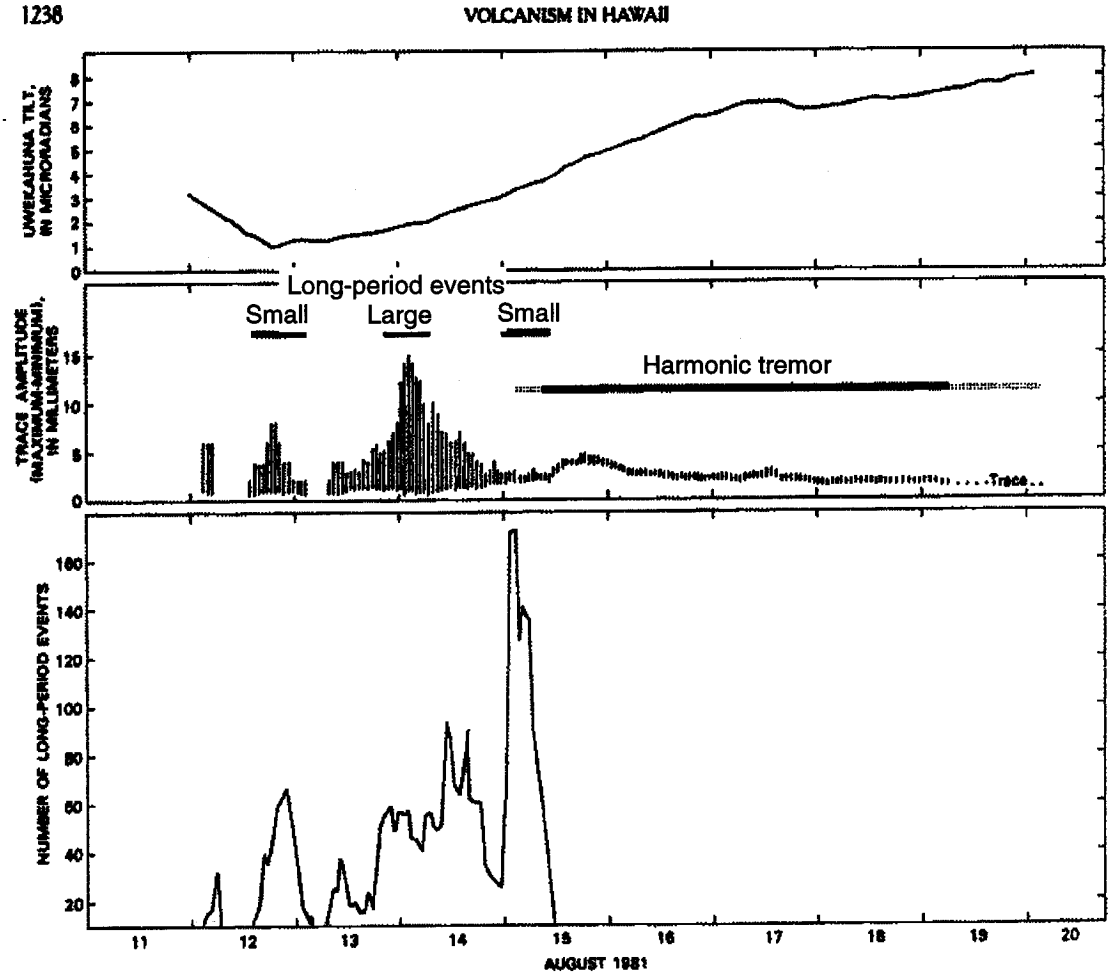

Figure 4.4: Ground tilt, long-period earthquakes and tremor plotted hourly following the later part of the August 1981 intrusion in the east rift zone of Kilauea. In the upper plot, the east-west component of tilt at Uwekahuna indicates reversal and reinflation of the summit following a major collapse. In the middle plot, vertical lines represent the hourly maximum-to-minimum amplitude range from tremor and long-period events read on station NPT at standard gain using Develocorder seismograms magnified 20 times. A wide maximum-minimum range implies large long-period events in a low background of tremor, whereas a narrow range and high minimum amplitude indicate high harmonic tremor with no discernible long-period events. The lower plot shows the hourly number of long-period events (> 10 events per hour) recorded at station NPT.

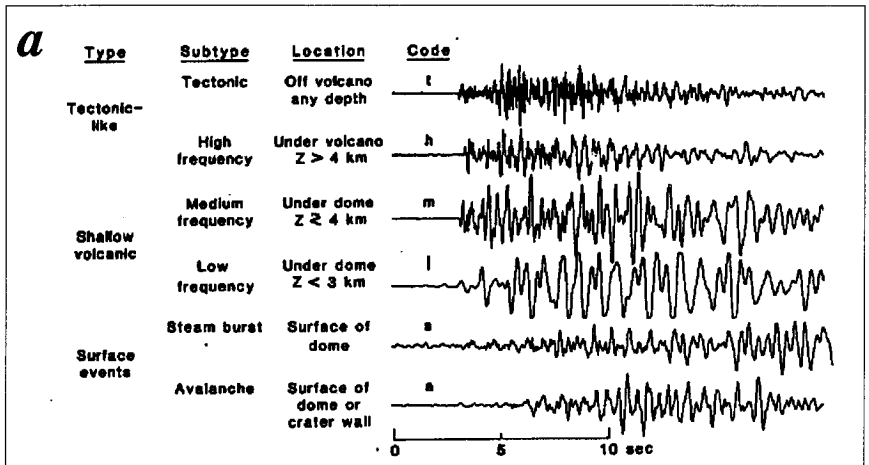

Fig. 1. Characteristic seismograms for the six categories of events observed at Mount St. Helens. Seismograms are from station SHW, located 3.6 km west of the active dome. The example of type t is from a tectonic earthquake located 8.2 km south of the dome at a depth of 5.6 km; type h, a high-frequency volcanic earthquake located under the dome at a depth of 6.2 km. The remaining four events occurred at shallow depth or at the surface near the dome: the example of type m is from a medium-frequency volcanic earthquake; type l, a low-frequency volcanic earthquake; type s, an observed gas burst from the top of the dome; type a, a rock avalanche from the south crater wall.

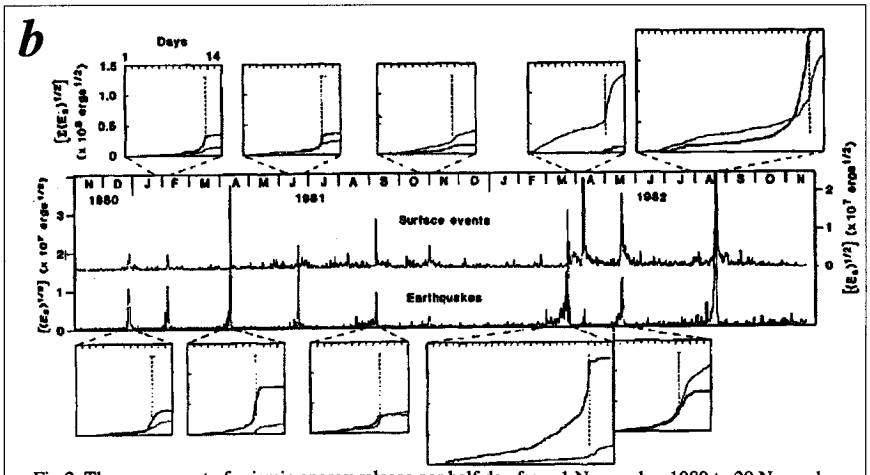

Fig 2. The square root of seismic energy release per half day from 1 Novermber 1980 to 20 November 1982. Surface events (types s and a) are plotted seprately from earthquakes (types m and l). The cumulative energy released during a 2-week period (a 4-week period in the case of the March 1982 and August 1982 eruptions) around each of the eruptions is shown near the time of each eruption. [377] Light lines represent surface events, and heavy lines represent shallow earthquakes. Each vertical dashed line indicates the most likely time of the beginning of the eruption.

Figure 4.5: Seismic activity at Mount St. Helens.

tics of continuous tremor resemble those of single 'LP' events (*Fehler* [1983], *Hofstetter and Malone* [1986]), implying that they share a common origin. *Fehler* [1983] demonstrates that the spectral peaks are stationary, varying slightly between the vertical and the horizontal components, and that their relative amplitude changes within the tremor sequence. He also shows that earthquakes do not excite the spectral behavior displayed by tremor, and that there is no correlation between tremor amplitude and frequency content. *Fehler* [1983] thus attributes the tremor waveform to the source. However, as was established at Old Faithful, tremor amplitude can change significantly without changing its spectral characteristics, and yet it is a pure site effect.

4.2.4 1989-1990 Redoubt Volcano eruption

During the 1989-1990 eruption of Redoubt volcano, Alaska, several types of ground motion were observed (*Power et al.* [1994]). These include Volcano tectonic events, shallow 'hybrid' events, shallow long-period events, tremor, and eruption (Figure 4.6). The December 14, 1989, activity precursory to the eruption (*Power et al.* [1994]) strongly resembles a typical eruption cycle at Old Faithful (Figure 4.6), as a swarm of long-period events which turns into continuous tremor culminates in an emergent eruption.

The RSAM records which average the amplitude over a 10-minute-long sliding window, also show great similarity to the event count histograms at Old Faithful (Figure 2.7). There is a general agreement that the harmonic frequency is a result of normal mode excitation of a vertical crack (*Chouet et al.* [1994], *Mori* [1995]), based on the observations that an explosion source did not excite the spectral peaks of the 'LP' event, and the fact that it can be argued that several spectral peaks are common to more than one station (Figure 4.7).

However, as was described in Chapter 4, the excitation of reverberation in the structure is strongly dependent on the frequency content of the source (Figure 3.8). The explosion source frequency content may be too high to efficiently excite the structure. Also, as demonstrated by Figure 4.7, most common spectral peaks are close to noise level, while some of the dominant peaks are not well correlated throughout the array.

Although this phenomenon may be explained by a radiation pattern of a vertical crack (*Chouet et al.* [1994]), based on the strong similarity in seismic behavior of Redoubt to Old Faithful, and on the uncertainties in the Redoubt data, it is just as plausible that the 'LP' events observed at Redoubt are the volcano's impulse response in the same way that the harmonic tremor at Old Faithful is the system's response to a single pulse.

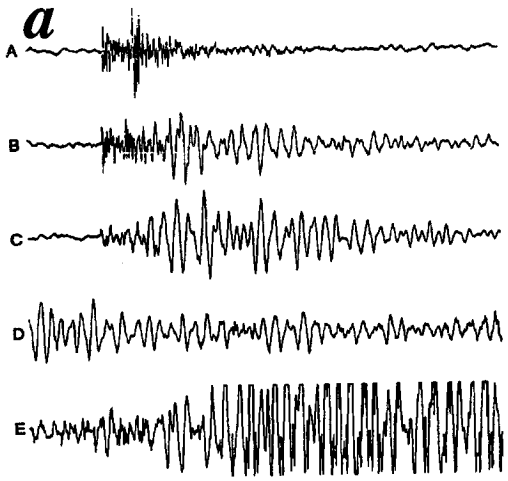

Fig 5. Typical waveforms of the various types of seismic signals originating from Redoubt Volcano. The waveforms are: (A) volcano-tectonic earthquake on December 20 at 6.75 km depth; (B) shallow hybrid event on December 16; (C) shallow long-period event on December 13; (D) tremor on December 14; and (E) Tephra eruption at 03:38 on December 15. All signals are from station RED.

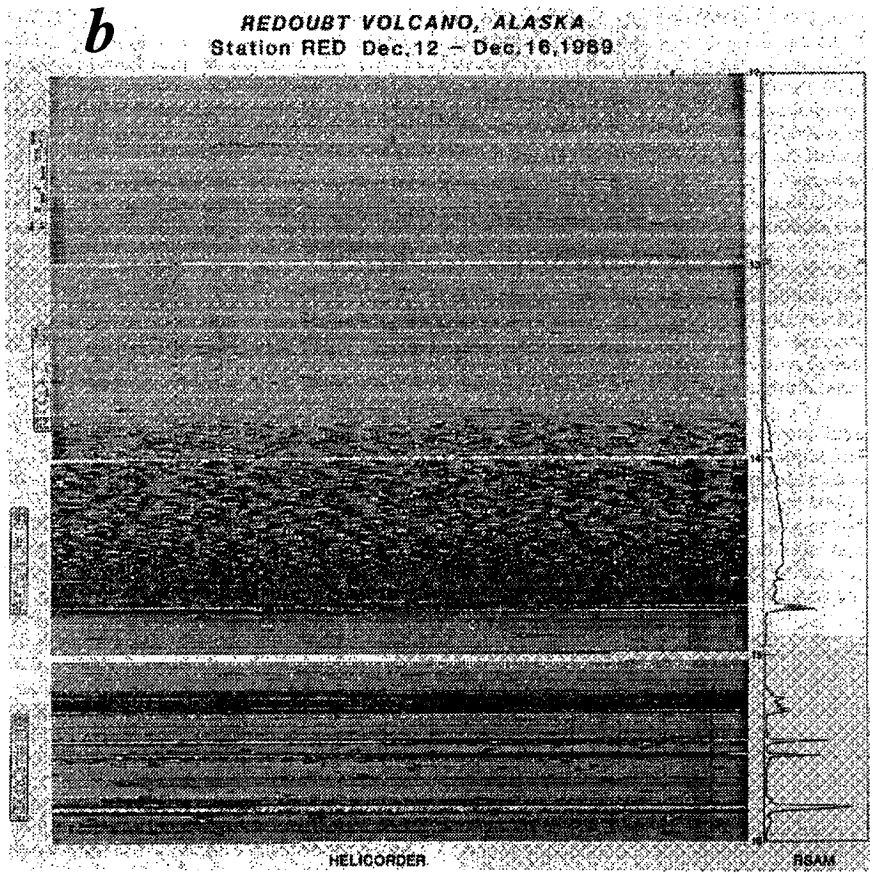

Fig. 11. Helicorder records (left) and RSAM average amplitude (right) from station RED for December 12 to 16. Note the swarm of long-period events and volcanic tremor which precedes the explosions at 09:47 and 10:09 on December 14. The initial explosions are followed by seismic quiescence, volcanic tremor (19:00 to 23:30), and tephra eruptions at 01:52, 03:38, and 10:13. The time scale of the Helicorders is UT (subtract 9 hours to convert to AST); each panel represents a 24-hour period.

Figure 4.6: Seismic activity at Redoubt Volcano.

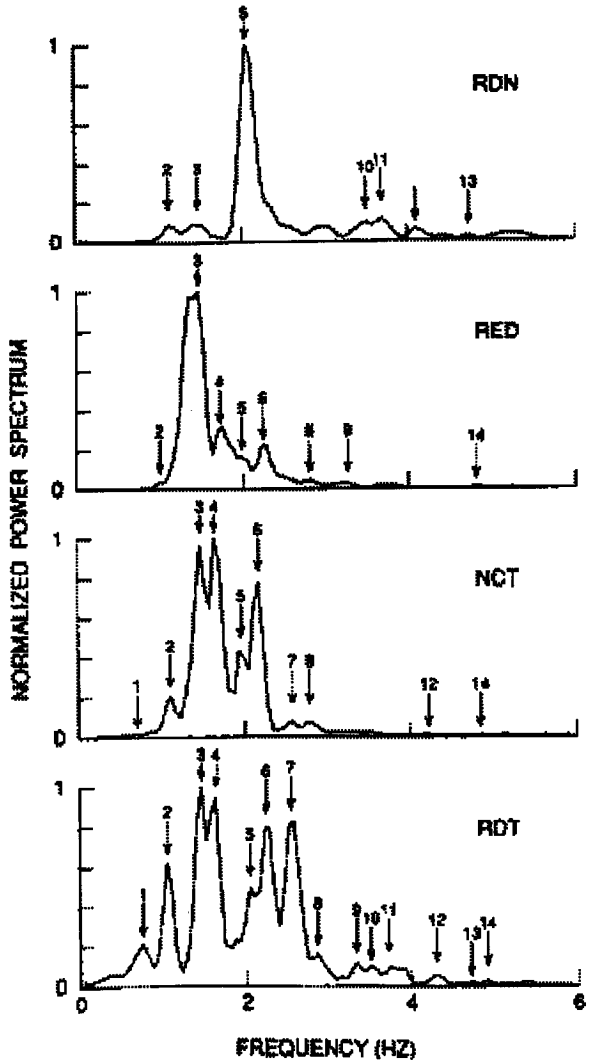

Figure 4.7: Power spectra of the vertical component of ground velocity obtained at stations RDN, RED, NCT and RDT for long-period events in the swarm of December 13-14. These spectra were obtained by stacking the spectra of 16 events, and then averaging and smoothing the result with a Hanning window. Each event was sampled with a 17-s window that spanned the entire record of motion for that event. frequencies are from 0 to 6 Hz with a resolution of a ± 0.03 Hz. Spectral peaks common to two or more stations are indicated by numbers. Note that the seismic energy is consentrated below 5 Hz and notice also the marked differences in the excitation of common spectral peaks at the four stations.

4.2.5 Stromboli, Italy

Strombolian activity is characterized by small repetitive explosions ($sim6 - 7$ explosions per hour), with volcanic tremor as stationary phenomenon (*Ripepe et al.* [1996]). *Ripepe et al.* [1996] have recorded simultaneous infrasonic pressure waves and seismic waves and observe a phenomenon similar to Old Faithful Geyser (Figure 4.8).

According to *Ripepe et al.* [1996] the pressure impulses are attributed to degassing events which superimpose to form continuous tremor. A correlation between the frequency content of the air-waves and the seismic waves is observed, and *Ripepe et al.* [1996] assigns it to source behavior. As can be observed in Figure 4.8, the amplitude of the air-waves and the seismic waves correlates as well. The background activity at Stromboli bears a strong resemblance to Old Faithful's activity, though the activity pattern preceding an eruption (explosion) differs. Stromboli's data suggest that an explosion is initiated through a process that differs from a full eruption at Old Faithful, and is probably more analogous to 'pre-play'-type explosion of a single large bubble. Stromboli like Old Faithful show no clear precursory signals to this type of event.

4.3 Summary

It is difficult to make a general statement about the applicability of Old Faithful activity to volcanic tremor analysis. As was illustrated in the above examples, volcano seismicity poses a wide range of phenomena varying significantly between volcanoes as well as at a given volcano. Therefore, the parallels should be drawn carefully and specifically. The examples shown so far suggest that seismic activity may show some similarities to Old Faithful's activity particularly when shallow tremor is concerned (Hawaii), and when the hydrothermal system is involved (*Leet* [1988], *Chouet* [1996]). In these cases continuous tremor is composed of individual 'LP' events which intensify, and culminate in an emergent eruption, without a particular precursor. As far as individual 'LP' events are concerned, although it has been generally assumed that the spectral characteristics of these events are a result of source resonance, it is evident that the loose identification of tremor as 'harmonic' may be in some cases misleading, as one volcano's 'non-harmonic' tremor is another's 'harmonic' tremor.

It seems that Old Faithful geyser outlines an end member of fluid flow induced seismicity in which structural reverberations are the sole mechanism for generating continuous harmonic tremor. The 'pure source' end members are cases such as Langila and Sakurajima, where very specific observations (stationary oscillation with no phase shifts, identical spectral characteristics at different sites, and independent non-seismic observations) lead to identification of source resonance. In between these two end-members lies a wide spectrum of phenomena, where source and path effects combine to form a complicated wavefield, characterized by a lack of coherent arrivals, and by intensity that

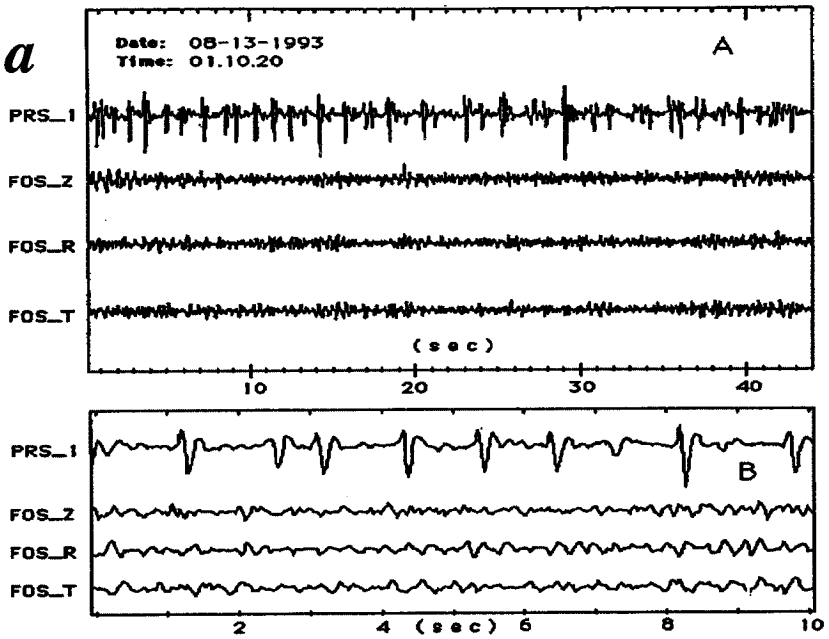

Infrasonic impulses and seismic signals recorded by pressure sensor and three component station located in the Fossa at only 150m from the vent. a) There is no evidence of transient signals in any of the three seismic stations. b) Close up of 10s long interval.

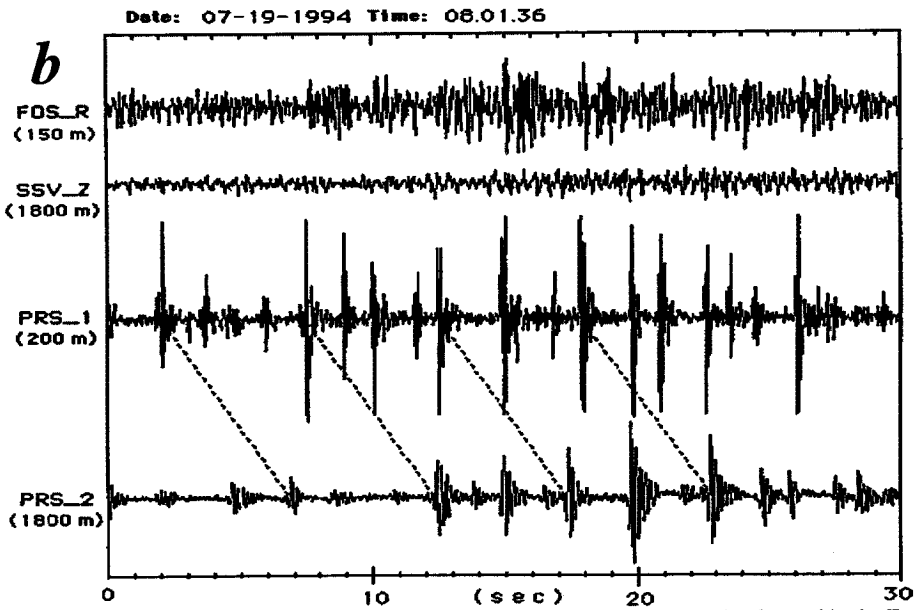

Infrasonic impulses and seismic signals recorded by the three component station located in the Fossa (150 M from the vent) and by the pressure sensor at 1800 m from the vents. Delay times of 4.7 s between PRS-1 and PRS-2 infrasonic impulses are in agreement with a 340 m/s sound velocity in atmosphere. The increased pressure values (6-7 Pa) recorded by the pressure sensor in the Fossa agrees with the visible increment of the degassing activity and with the records of the same impulses at 1800 m from the vent.

Figure 4.8: Seismic and inra-sonic recordings at Stromboli.

generally correlates with surface activity such as inflation, deflation and eruption.

The main pitfall in volcanic tremor analysis is its general simple harmonic appearance. Owing to the simple harmonic behavior of the ground motion, source-resonator models are necessarily inconclusive about the exciting mechanism. Any resonator (be it an organ pipe, oscillating crack or a waveguide) may be excited by one of a number of different mechanisms, provided it has the right frequency content. In volcanoes particularly, the physical properties needed for determining the source dimensions and source properties are poorly constrained. For example, the sound velocity in a two-phase water-steam fluid mixture can vary by two orders of magnitude from a few tens of meters per second, to a few thousands of meters per second *Kieffer* [1977], and the elastic wave velocity in rock from ~200 m/s (unconsolidated ash) to ~2000 m/s (lava flows), both of which are abundant on volcanoes. Further, most volcanic edifices have extremely complicated stratigraphies and topography, which complicate path effects. It was suggested (*Chouet* [1996]) that spectral stacking may help identify non-path-effect spectral peaks. While stacking the spectra of numerous 'LP' events might help clean the record, and may indeed bring source effects to the foreground, it does not guarantee elimination of path effects. If we were to stack Old Faithful's 'LP' events, we would certainly not outline any source related activity.

One way to avoid propagation complexities is to analyze the broadband seismicity. Preliminary attempts to use broadband data on volcanoes have begun to unravel the processes that were formerly obscured by the band-limited instruments (*Neuberg et al.* [1994], *Kawakatsu et al.* [1992]). Including 3D propagation effects and topography (*Ohminato and Chouet* [1996]) will be needed to reduce the uncertainties outlined so far.

Chapter 5 Conclusions

This work resolved some of the issues we set out to explore, in particular the origin of its harmonic tremor. It was demonstrated that the source of harmonic tremor at Old Faithful Geyser is impulsive and that the geological structure plays a crucial role in filtering the source and responding harmonically to it. It was also established that continuous harmonic tremor at Old Faithful results from a superposition of impulses in analogy to 'LP' events on volcanoes, and is not due to source resonance. In that, Old Faithful represents an end member of fluid flow seismicity, which partly applies to some volcanic tremor examples, mainly eruption related shallow tremor.

A source model which fits the observed data in the form of a few centimeter size bubbles collapsing near the top of the water column was suggested. Subsequently it was shown that a simple geologic model of a shallow soft layer can react as a wave guide for shear energy resulting in near monochromatic reverberations. Support for this model was found in shallow seismic profiles and in documentation of stratigraphy in the Upper Geyser Basin. Similar geologic structure are common on volcanoes, where soft ash and hard lava flows, or ashes of different deoposition histories and different densities are laid interchangeably with sharp contacts between them. It is therefore plausible that some of the volcanic tremor models may not be a reliable description of the source. Propagation effects need to be incorporated into the analysis, and constraints from non-seismic observations are necessary. Also, as the spectrum of flow phenomena observed in and around volcano is vast and due to the complexities described above, correlations between different volcanic systems should be made carefully.

Volcanic tremor has been extensively used as a tool for predicting eruptions. Currently, the predictive power of volcanic tremor stems from its existence, rather than from a full understanding of the physical mechanisms which generate it, as has been the case in Pinatubo, Redoubt and Spurr volcanoes (*Mori* [1995]). As was pointed out by *Chouet* [1996], the challenge is understanding the activity which is less clearly correlated with eruptions, in particular the deep tremor, believed to be related to magma transport at depth. The Old Faithful analog for shallow tremor suggests that shallow tremor, while being a good last minute precursor, is probably not useful for long-term prediction.

Chapter 6 Appendix

6.1 Appendix A: The relationship between eruption duration and the interval between eruptions

After a long eruption the interval *Azzalini and Bowman* [1990] have modeled this relationship using a second order Markov chain, which is summarized in the following table:

	s,l	*l,s*	*l,l*
s,l	0	0.689	0.311
l,s	1	0	0
l,l	0	0.388	0.612

Table 1 lists the probabilities that an eruption will be short (s) or long (l) given that it was preceded by a sequence of two eruptions of short or long duration. For example, the probability for having a short eruption following a sequence of short and then long eruptions will be described by the line *s,l* and column *l,s*. A close look at the table shows that the uncertainty is always related to the eruption following a long eruption. (A short eruption is always followed by a long one.)

6.2 Appendix B: Rayleigh collapse

Rayleigh [1917] calculated the collapse time of a spherical cavity in a body of incompressible fluid with constant pressure P_∞ at infinity. In spherical-polar coordinates the incompressibility condition and the spherical symmetry require that the fluid velocity field would have the characteristic:

$$\frac{\dot{r}}{\dot{R}} = \frac{R^2}{r^2} \tag{6.1}$$

where R is the instantaneous cavity wall, and $r > R$ is a location outside the bubble. For a fluid of density ρ, the kinetic energy of motion is:

$$\frac{1}{2}\rho \int_R^\infty \dot{r}^2 4\pi r^2 dr = 2\pi\rho\dot{R}^2 R^2 \tag{6.2}$$

The work done by the pressure in closing the cavity from a maximum radius R_M to R is:

$$\frac{4}{3}\pi P_\infty \left({R_M}^3 - R^3\right) \tag{6.3}$$

and equating equations A2 and A3 we get:

$$\dot{R}^2 = \frac{2P_\infty}{3\rho}\left(\frac{{R_M}^3}{R^3} - 1\right) \tag{6.4}$$

Since $\dot{R} = dR/dt$ we can seperate variables and get:

$$t = \sqrt{\left(\frac{3\rho}{2P_\infty}\right)} \int_R^{R_M} \frac{R^{3/2}}{\left({R_M}^3 - R^3\right)^{1/2}} dR \tag{6.5}$$

for which the solution is:

$$\tau_c = 0.915 R_M \sqrt{\rho/P_\infty} \tag{6.6}$$

Bibliography

Aki, K., and R. Koyanagi, Deep volcanic tremor and magma ascent mechanism under Kilauea, Hawaii, *Journal of Geophysical Research, 86*(B8), 7095–7109, 1981.

Aki, K., M. Fehler, and S. Das, Source mechanism of volcanic tremor: Fluid driven crack models and their application to the 1963 Kilauea eruption, *Journal of Volcanology and Geothermal Research, 2*, 259–287, 1977.

Azzalini, A., and A. W. Bowman, A look at some data on the Old Faithful Geyser, *Applied Statistics, 39*(3), 357–365, 1990.

Birch, F., and G. C. Kennedy, Notes on geyser temperatures in Iceland and Yellowstone National Park, *Geophy. Monog. Am. Geophys. Union, 16*, 329–336, 1972.

Blake, W. K., *Mechanics of flow induced sound and vibration*, vol. 1, chap. 6, p. 404. Academic Press, 1986.

Boure, J. A., A. E. Bergles, and L. S. Tong, Review of two-phase flow instability, *Nuc. Eng. and Design, 25*, 165–192, 1973.

Chapman, R. B., and M. S. Plesset, Thermal effects in the free oscillation of gas bubbles, *J. of Basic Eng.*, pp. 373–376, 1971.

Chouet, B., Long-period volcano seismicity: Its source and use in eruption forecasting, *Nature, 380*(6572), 309–316, 1996.

Chouet, B. A., Excitation of buried magmatic pipe: A seismic source model for volcanic tremor, *Journal of Geophysical Research, 90*, 1881–1893, 1985.

Chouet, B. A., R. A. Page, C. D. Stephens, J. C. Lahr, and J. A. Power, Precursory swarms of long-period events at Redoubt Volcano (1989-1990), Alaska: Their origin and use as a forecasting tool, *Journal of Volcanology and Geothermal Research, 62*, 95–136, 1994.

Clark, *Handbook of Physical constants.* Table 9-4, 1966.

Fehler, M., Observations of volcanic tremor at Mount St. Helens volcano, *Journal of Geophysical Research, 88*(B4), 3476–3484, 1983.

Fenner, C. N., Bore-hole investigations in the Yellowstone Park, *Jour. Geology, 44*, 225–315, 1936.

Ferrazzini, V., K. Aki, and B. Chouet, Characteristics of seismic waves composing Hawaiian volcanic tremor and gas-piston events observed by a near-source array, *Journal of Geophysical Research, 96*(B4), 6199–6209, 1991.

Goldstein, P., and B. Chouet, Array measurements and modeling of sources of shallow volcanic tremor at kilauea Volcano, Hawaii, *Journal of Geophysical Research, 99*(B2), 2637–2652, 1994.

Gordeev, E., Modeling of volcanic tremor wave fields, *Journal of Volcanology and Geothermal Research, 51*, 145–160, 1992.

Griffith, P., Geysering in fluid filled lines, An ASME publication 62-HT-39, American Society of Mechanical Engineering, ASME-AIChE Heat Transfer Conference and Exhibit, Huston, Texas, 1962.

Haskell, N. A., The dispersion of surface waves on multilayered media, *Bull. Seis. Soc. Am., 43*, 17–34, 1953.

Hofstetter, A., and S. D. Malone, Observations of volcanic tremor at Mount St. Helens in April and May 1980, *Bulletin of the Seismological Society of America, 76*(4), 923–938, 1986.

Julian, B. R., Volcanic tremor: nonlinear excitation by fluid flow, *Journal of Geophysical Research, 99*(B6), 11,859–11,877, 1994.

Kamo, K., T. Furuzawa, and J. Akamatsu, Some natures of volcanic micro-tremors at Sakurajima Volcano, *Bulletin of the Volcanological Society of Japan, 22*, 41–58, 1977.

Kawakatsu, H., T. Ohminato, and Y. Kuwahara, Broadband seismic observation at the Sakurajima Volcano, Japan, *Geophysical Research Letters, 19*, 1959–1962, 1992.

Kedar, S., B. Sturtevant, and H. Kanamori, The origin of harmonic tremor at Old Faithful Geyser, *Nature, 379*, 708–711, 1996.

Kieffer, S. W., Sound speed in liquid-gas mixtures: water-air and water-steam, *Journal of Geophysical Research, 82*(20), 2895–2904, 1977.

Kieffer, S. W., Seismicity of Old Faithful Geyser: An isolated source of geothermal noise and possible analogue of volcanic tremor, *J. Volcanology and Geotherm. Res., 22*, 59–95, 1984.

Koyanagi, R. Y., B. Chouet, and K. Aki, Origin of volcanic tremor in Hawaii, part 1. Data from the Hawaiian Volcano Observatory 1969-1985, in *Volcanism in Hawaii*, edited by R. W. Decker, T. W. Wright, and P. H. Stauffer, no. 1350, pp. 1221–1259. 1987.

Leet, R. C., Saturated and subcooled hydrothemal boiling in groundwater flow channels as a source of harmonic tremor, *Journal of Geophysical Research, 93*(B5), 4835–4849, 1988.

Malone, S. D., E. T. Endo, C. S. Weaver, and J. W. Ramey, Seismic monitoring for eruption prediction, in *The 1980 eruptions of Mount Saint Helens, Washington*, edited by P. W. Lipman, and D. R. Mullineaux, no. 1250, pp. 803–813. U. S. Geological Survey, 1981.

Malone, S. D., C. Boyko, and C. S. Weaver, Seismic precursors to the Mount St. Helens eruptions in 1981 and 1982, *Science*, *221*, 1376–1378, 1983.

McNutt, S. R., observations and analysis of b-type earthquakes, explosions and volcanic tremor at Pavlov Volcano, Alaska, *Bulletin of the Seismological Society of America*, *76*, 153–175, 1986.

Mori, J., Volcano seismology hazard assessment, *Reviews of Geophysics, Supplement*, 263–267, 1995.

Mori, J., H. Patia, C. McKee, I. Itikari, P. Lowenstein, P. De-Saint-Ours, and B. Talai, Seismicity associated with eruptive activity at langila volcano, papua new guinea, *Journal of Volcanology and Geothermal Research*, *38*, 243–255, 1989.

Neuberg, J., R. Luckett, and M. Ripepe, Highlights from a seismic broadband array on Stromboli Volcano, *Geophysical Research Letters*, *21*, 759–752, 1994.

Ohminato, T., and B. A. Chouet, A free-surface boundary condition for including 3d topography in the finite difference method, *Submitted to Bulletin of the Seismological Society of America*, 1996.

Plesset, M. S., The dynamics of cavitation bubbles, *ASME j. Appl. Mech.*, *16*, 228–231, 1949.

Power, J. C., R. A. Lahr, B. A. Page, B. A. Chouet, C. D. Stephens, D. H. Harlow, T. L. Murray, and J. N. Davies, Seismic evolution of the 1989-1990 eruption sequence of Redoubt Volcano, Alaska, *Journal of Volcanology and Geothermal Research*, *62*, 69–94, 1994.

Puzyrev, N. N., and V. A. Kulikov, Experimental data on the propagation and excitation of transverse waves in water-saturated deposits, *Geologiya i Geofizika*, *21*(12), 86–94, 1980.

Rayleigh, On the pressure developed in a liquid during the collapse of a spherical bubble, *Philos. Mag.*, *34*, 94–98, 1917.

Rinehart, J. S., Earth tremors generated by Old Faithful Geyser, *Science*, *150*, 494–496, 1965.

Rinehart, J. S., Geophysical study of geyser action in Yellowstone National Park, *Journal of Geophysical Research*, *72*(18), 4651–4663, 1967.

Rinehart, J. S., *Geysers and Geothermal Energy*. Springer-Verlag, 1980.

Ripepe, M., P. Poggi, T. Braun, and E. Gordeev, Infrasonic waves and volcanic tremor at Stromboli, *Geophysical Research Letters*, *23*(2), 181–184, 1996.

Turcotte, D. L., and G. Schubert, *Geodynamics*. John Wiley and Sons, Table 9-1, 1982.

Weaver, C. S., and S. D. Malone, Mount. St. Helens seismic events: Volcanic earthquakes or glacial noise?, *Geophysical Research Letter*, *3*, 197–200, 1976.

White, D. E., R. O. Fournier, L. J. P. Muffler, and A. H. Truesdell, Physical results of research drilling in thermal areas of Yellowstone National Park, Wyoming, Professional paper 892, U. S. Geological Survey, 1975.